ALMA MATER STUDIORUM
UNIVERSITÀ DI BOLOGNA

DEPARTMENT OF PHYSICS AND ASTRONOMY "A. RIGHI"

SECOND CYCLE DEGREE

PHYSICS

Neutrino-Hydrogen interactions in the SAND detector of the DUNE experiment

Supervisor
Dr. Gabriele Sirri

Co-supervisors
Dr. Alberto Mengarelli
Dr. Federico Battisti

Defended by
Camilla Roselli

Graduation Session December 2025

Academic Year 2024/2025

Come quando la nebbia si dissipa,
lo sguardo a poco a poco raffigura
ciò che cela 'l vapor che l'aere stipa

Dante Alighieri, Inf. XXXI, 34–36

Abstract

The Deep Underground Neutrino Experiment (DUNE) is a next-generation long baseline neutrino program, exposed to the world's most intense neutrino beam. DUNE is designed to measure the CP violation phase, to determine the neutrino mass ordering, and to improve the precision of oscillation parameters.

Its near detector complex plays a central role in constraining the neutrino flux and interaction models that dominate the systematic uncertainties of the oscillation analysis. A major limitation arises from large uncertainties in the neutrino-nucleus cross section, driven by nuclear modeling and final-state interactions. A promising strategy to overcome this challenge is to measure neutrino interactions on hydrogen, where the cross sections are known with much smaller uncertainties.

This work focuses on the SAND detector (System for on-Axis Neutrino Detection) located at the DUNE near site and details a methodology for achieving precise measurements of (anti)neutrino interactions on hydrogen in its low-density tracker. The approach relies on the statistical subtraction of interactions observed on thin graphite targets from those on polypropylene ("solid hydrogen" technique). This capability is investigated through a full detector simulation. An estimate of the systematic uncertainties on the energy distribution of (anti)neutrino on hydrogen is provided.

Contents

List of Figures

List of Tables

Introduction

Neutrinos are the most abundant known particle in the universe, as well as some of the most mysterious and not yet fully understood ones. Neutrinos are clear evidence of physics beyond the Standard Model, since in the Standard Model they are described as massless, whereas experimental evidence of neutrino oscillations implies that they do have mass. In the last decades, many advances have been made in neutrino physics, but many questions still remain to be investigated. For this purpose, new neutrino experiments are required.

The Deep Underground Neutrino Experiment (DUNE) is a next-generation long-baseline neutrino oscillation experiment. Its primary objectives are to measure the CP violation phase δ_{CP}, to determine the neutrino mass ordering, and to measure the neutrino mixing parameters with unprecedented precision. DUNE will consist of two neutrino complex detectors, a Far Detector and a Near Detector, exposed to the world's most intense neutrino beam.

Among the ND components, the SAND detector (System for on-Axis Neutrino Detection) will play a central role. It will be composed of an electromagnetic calorimeter, a low-density tracker and a small active liquid argon target. All these components are embedded in a magnetic field (0.6 T) generated by a superconducting solenoid. SAND will continuously monitor the beam on-axis and constrain flux and cross-section systematics, improving the precision of the oscillation analyses. One of the dominant limitations on the achievable precision on the flux measure arises from large uncertainties in the neutrino-nucleus cross section. These are affected by the choice of nuclear models and final-state interactions, which cannot be entirely described using perturbative QCD. SAND will overcome this challenge by measuring neutrino interactions on free nucleons, where the cross sections are known with much smaller uncertainties. SAND will obtain neutrino interactions on hydrogen, exploiting the structure of its tracker that will be equipped with thin layers of graphite (pure C) targets and polypropylene targets (C_3H_6). In detail, $\nu - H$ interaction will be obtained via a statistical subtraction technique (referred to as "solid hydrogen"), which consists of a statistical subtraction of interactions on C from those on C_3H_6.

The goal of this work is to estimate the energy distribution of neutrinos interacting on hydrogen and evaluate the relative systematic uncertainties, exploiting the "solid hydrogen" technique. In chapter 1, an overview of neutrino physics is presented with a particular focus on neutrino interaction theory and phenomenology. In chapter 2 and in

chapter 3, the DUNE experiment and the SAND detector are illustrated, respectively, including their design and physics goals. In chapter 4, the description of the simulation framework used for this analysis is provided. In chapter 5, the analysis steps are detailed, including the signal selection, the performance of statistical subtraction and the evaluation of the systematic uncertainties.

Chapter 1

Neutrino Physics

1.1 Neutrino Hypothesis and Discovery

The neutrino was first proposed by Pauli in 1930 [1] as a third particle involved in the β decay, to justify the continuous value of the observed electron energy. Initially called *neutron* by Pauli, and then renamend *neutrino* by Fermi [2], since around the same time Chadwick had discovered the particle we now know as the neutron [3], this particle has some unique characteristics. It was postulated to be a fermion smaller than the electron, massless[1], with no electric charge, and not subject to strong interaction. For these reasons, it was considered an elusive particle, seemingly undetectable, and impossible to confirm experimentally.

The neutrino was directly observed in 1956 by Reines and Cowan (Nobel in 1995) at the Savannah River Plant of the U. S. Atomic Energy Commission [4]. The experimental method consisted in detecting the particle through the inverse β decay process on proton: $\bar{\nu} \;\; p \rightarrow n \;\; e^+$, taking advantage of the antineutrino flux produced by the Savannah River nuclear reactor. The experiment also measured the cross-section for the reaction obtaining the value $1.2^{+0.7}_{-0.4} \times 10^{-43}$ cm^2, which was in agreement with the theoretical expected value $(1.0 \pm 0.17) \times 10^{-43}$ cm^2 [5].

In 1962 Schwartz, Lederman and Steinberger (1988 Nobel Prize) [6] observed a second type of neutrino at the Brookhaven Laboratory. They showed that neutrinos produced in pion decay $\pi^- \rightarrow \mu^- \, \bar{\nu}_\mu$ generated only muons, not electrons. This provided strong evidence for a second neutrino type i.e. the muon neutrino, different from the electron neutrino observed by Reines and Cowan. This experiment marked the first time a neutrino beam produced by an accelerator was used. Today, neutrino beams are still generated in much the same way, a method that will be described in Chap. 2.

In 2001, a third type i.e. the tau neutrino was directly observed at the DONUT (Direct Observation of the NU Tau) experiment at Fermilab [7]. The ν_τ was revealed by the tau leptons produced in charged current interactions in iron. In this case also, a neutrino beam was used.

[1] Pauli hypothesized a neutrino mass of the same order of magnitude as the electron mass, then Fermi and Perrin suggested that neutrinos could be massless.

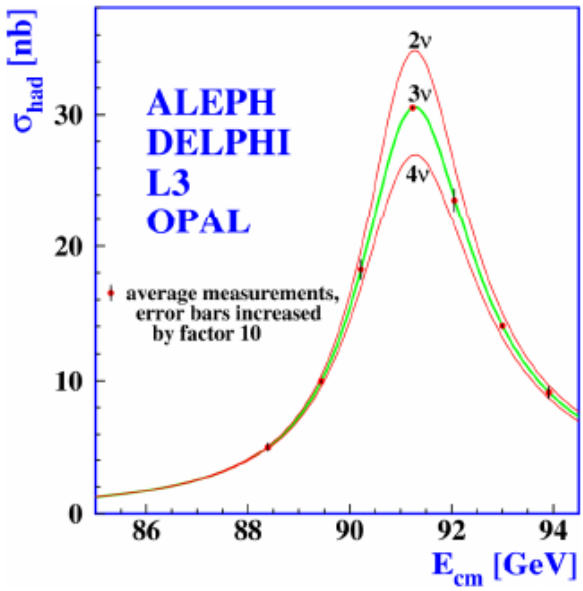

Fig. 1.1: *Curves represent the predicted total cross-section for hadron production as a function of the center-of-mass energy, considering 2, 3, and 4 neutrino families. Dots are data from LEP* [8].

The existence of exactly three neutrino flavors was confirmed by indirect measurements performed at LEP (Large Electron Positron collider) in 1989 [8]. The analysis of the Z boson decay width confirmed the existence of only three families of interacting neutrinos with mass $M_\nu < M_Z/2$: an additional neutrino family would lead to a wider Z resonance and a diminished peak height, while one family less would produce the opposite effect, as shown in Fig. 1.1. LEP measured $N_\nu = 3.27 \pm 0.30$, current measurements agree with the LEP results, setting the number of neutrino families at: $N_\nu = 2.996 \pm 0.007$ [9].

1.2 Neutrinos in the Standard Model

In the Standard model of particle physics neutrinos are well described as massless particles. The Standard Model (SM) is a gauge theory based on the local symmetry group $\mathrm{SU(3)_C} \times \mathrm{SU(2)_L} \times \mathrm{U(1)_Y}$, where C, L and Y stand for color charge, left-handed chirality and weak hypercharge, respectively. $\mathrm{SU(3)_C}$ describes the strong interaction, while $\mathrm{SU(2)_L} \times \mathrm{U(1)_Y}$ describes the electroweak one [10]. This theory provides a unified picture in which the strong, electromagnetic, and weak interactions between particles are themselves described by the exchange of particles. In SM particles are organized into two main groups: bosons and fermions.

Bosons can be divided into two groups according to their spin. There are the gauge bosons with spin 1, and one scalar boson with spin 0. The firsts mediate the fundamental interactions (i.e. photons mediate electromagnetic interaction, $W^\pm$ and Z

mediate weak interaction, and gluons mediate the strong one), whereas the scalar boson, the Higgs boson, gives masses to the other particles via the Spontaneous Symmetry Breaking mechanism.

Fermions are matter particles, they have spin $\frac{1}{2}$ and they are divided into quarks and leptons, both arranged into three generations. In addition, each fermion has an associated antiparticle. Quarks are fundamental constituents of hadrons and, unlike leptons, do not exist as free particles. Fermions can also be classified according to whether they participate in weak interactions or not. Those that weakly interact are arranged into $\mathrm{SU(2)_L}$ left-handed doublets, while those that do not interact are $\mathrm{U(1)_Y}$ right-handed singlets [11]. This distinction arises from a characteristic feature of the weak interaction, which, as demonstrated by the *Wu et al.* experiment [12] violates parity. This means that only left-handed particles or right-handed antiparticles participate in the interaction. Moreover, it was proven, by the *Goldhaber et al.* experiment [13], that neutrinos maximally violate parity, which implies that only left-handed neutrinos and right-handed antineutrinos exist. So far, no evidence of right-handed neutrinos of any flavor has been observed. All the particles of the SM are summarized in Tab. 1.1 and Tab. 1.2

	Symmetry Group	**Bosons**
Electroweak bosons	$\mathrm{U(1)_Y}$ $\mathrm{SU(2)_L}$	γ $W^{\pm}, Z$
Strong Bosons	$\mathrm{SU(3)_C}$	g

Tab. 1.1: *Bosons of the Standard Model.*

Leptons		**Antileptons**	
$\begin{pmatrix}\nu_e\\ e\end{pmatrix}_L$	e_R	$\begin{pmatrix}\overline{\nu}_e\\ \bar{e}\end{pmatrix}_R$	$\overline{e}_L$
$\begin{pmatrix}\nu_\mu\\ \mu\end{pmatrix}_L$	μ_R	$\begin{pmatrix}\overline{\nu}_\mu\\ \bar{\mu}\end{pmatrix}_R$	$\overline{\mu}_L$
$\begin{pmatrix}\nu_\tau\\ \tau\end{pmatrix}_L$	τ_R	$\begin{pmatrix}\overline{\nu}_\tau\\ \bar{\tau}\end{pmatrix}_R$	$\overline{\tau}_L$

Quarks			**Antiquarks**		
$\begin{pmatrix}u\\ d\end{pmatrix}_L$	u_R	d_R	$\begin{pmatrix}\overline{u}\\ \overline{d}\end{pmatrix}_R$	$\overline{u}_L$	$\overline{d}_L$
$\begin{pmatrix}c\\ s\end{pmatrix}_L$	c_R	s_R	$\begin{pmatrix}\overline{c}\\ \overline{s}\end{pmatrix}_R$	$\overline{c}_L$	$\overline{s}_L$
$\begin{pmatrix}t\\ b\end{pmatrix}_L$	t_R	b_R	$\begin{pmatrix}\overline{t}\\ \overline{b}\end{pmatrix}_R$	$\overline{t}_L$	$\overline{b}_L$

Tab. 1.2: *On the left leptons and antileptons are illustrated, on the right quarks and antiquarks. Left-handed particles are labelled with L, right-handed particles with R.*

1.2.1 Theory of Neutrino interactions

Neutrinos are electrically and color neutral fermions that can only interact weakly or gravitationally[2]. Neutrino interactions are well described by the Standard Model, they

[2]Gravitation is not considered here because it is not described by the Standard Model.

can be explained considering only the electroweak part of the SM Lagrangian, so it is sufficient to consider only the $SU(2)_L \times U(1)_Y$ part of the SM symmetry group unified by the Glashow-Weinberg-Salam (GWS) model [14][15][16].

The $SU(2)_L$ symmetry group is called *weak isospin*. It has three generators I_a, with $a = 1, 2, 3$, which obey the commutation relations:

$$[I_a, I_b] = i\epsilon_{abc} I_c, \tag{1.1}$$

where ϵ_{abc} is the Levi-Civita tensor and $I_a \equiv \tau_a/2$ with τ_a Pauli matrices.

The symmetry group $U(1)_Y$ is called *hypercharge* and it is generated by the hypercharge operator Y, which is connected to I_3 and the electric charge operator Q by the Gell-Mann–Nishijima relation:

$$Q = I_3 + \frac{Y}{2}. \tag{1.2}$$

To the groups $SU(2)_L$ and $U(1)_Y$, two coupling constants are associated, respectively g and g', and four intermediate vector gauge bosons. The bosons W_1^μ, W_2^μ, W_3^μ are associated with $SU(2)_L$, while B^μ is associated with $U(1)_Y$. These four gauge bosons are initially massless and do not correspond to the physical states; instead, the physical states are defined as a combination of them:

$$W_\pm^\mu = \frac{(W_1^\mu \pm i W_2^\mu)}{\sqrt{2}}, \tag{1.3}$$

$$A^\mu = W_3^\mu \sin\theta_W + B^\mu \cos\theta_W, \tag{1.4}$$

$$Z^\mu = W_3^\mu \cos\theta_W - B^\mu \sin\theta_W. \tag{1.5}$$

Physically, A^μ is the electromagnetic field whose quanta are photons, Z^μ is the neutral weak field whose quanta are Z particles of mass $M_z \sim 91$ GeV/c^2, and $W_\pm$ are the charged weak fields whose quanta are the particles of mass $M_W \sim 80$ GeV/c^2. These masses arise from the spontaneous symmetry breaking of the $SU(2)_L \times U(1)_Y$ group through the Higgs mechanism, and they can be written as:

$$M_W = \frac{gv}{2}, \tag{1.6}$$

$$M_Z = \frac{gv}{2\cos\theta_W}, \tag{1.7}$$

where v is the Higgs field vacuum expectation value.
The angle θ_W is called the *weak mixing angle* or *Weinberg angle* and is given by the relation:

$$\sin^2\theta_W = 1 - \left(\frac{M_W}{M_Z}\right)^2, \tag{1.8}$$

which is fixed by the Spontaneous Symmetry Breaking mechanism. Its value was measured to be $\sin^2\theta_W \sim 0.231$ and $\theta_W \sim 28.7°$.

The two coupling constants are determined by the two unification relations that come from the GWS model and can be written as follows, where e is the elementary electric charge:

$$e = g \sin\theta_W, \tag{1.9}$$
$$e = g' \cos\theta_W. \tag{1.10}$$

In this framework, neutrino interactions are divided into two categories: charged-current and neutral-current interactions.
Charged-current interactions (CC) are mediated by charged gauge bosons $W^{\pm}$. They are described by leptonic charged weak current,

$$j^{\rho}_{W,L} = 2 \sum_{\alpha=e,\mu,\tau} \overline{\nu}_{\alpha L} \gamma^{\rho} \ell_{\alpha L}, \tag{1.11}$$

and by the corresponding leptonic charged-current weak interaction Lagrangian,

$$\mathscr{L}^{(\mathrm{CC})}_{I,L} = -\frac{g}{2\sqrt{2}} \left(j^{\rho}_{W,L} W_{\rho} + j^{\rho\dagger}_{W,L} W^{\dagger}_{\rho} \right). \tag{1.12}$$

Moreover, the charged-current vertex allows us to define the neutrino flavor, which is the flavor of the charged lepton connected to the same vertex:

$$\begin{aligned} W^+ &\to e^+ + \nu_e \\ &\to \mu^+ + \nu_\mu \\ &\to \tau^+ + \nu_\tau \end{aligned}$$

Neutral-current interactions (NC) are mediated by the neutral gauge boson Z_0. They are described by the neutrino part of the leptonic neutral current,

$$j^{\rho}_{Z,\nu} = 2 g^{\nu}_{L} \sum_{\alpha=e,\mu,\tau} \overline{\nu}_{\alpha L} \gamma^{\rho} \nu_{\alpha L}, \tag{1.13}$$

and the corresponding neutrino leptonic neutral current weak interaction Lagrangian,

$$\mathscr{L}^{(\mathrm{NC})}_{I,\nu} = -\frac{g}{2\cos\vartheta_W} j^{\rho}_{Z,\nu} Z_{\rho}. \tag{1.14}$$

In Eq. 1.13, the coupling constant g^{ν}_{L} is defined considering the relations of the GWS model for the couplings to left-handed and right-handed fermions:

$$g^{f}_{L} = I^{f}_{3} - q_f \sin^2\theta_W, \tag{1.15}$$
$$g^{f}_{R} = -q_f \sin^2\theta_W, \tag{1.16}$$

where L stands for left, R stands for right, and $f = (\nu, \ell,\ Up-type,\ Down-type)$. I^{ν}_{3} is the value of the third component of the weak isospin and q_f is the electric charge of the considered fermion, in units of the elementary electric charge e. Knowing that for neutrinos $q_\nu = 0$, the coupling constant is $g^{\nu}_{L} = \frac{1}{2}$.

When neutrino interactions occur below the energy scale of the mediator bosons ($\sim$ 100 GeV), the considered Lagrangian can be simplified. In this low-energy region, weak interaction can be approximated to a point-like interaction as suggested by the Fermi Theory. In this case, both CC and NC processes are described by effective Lagrangians:

$$\mathscr{L}_{eff}^{(\mathrm{CC})} = -\frac{G_F}{\sqrt{2}} j_{W\rho}^{\dagger} j_W^{\rho}, \tag{1.17}$$

$$\mathscr{L}_{eff}^{(\mathrm{NC})} = -\frac{G_F}{\sqrt{2}} j_Z^{\rho} j_{Z\rho}, \tag{1.18}$$

where $G_F = \sqrt{2}g^2/8M_W^2 \simeq 1.166 \times 10^{-5}$ GeV^{-2} is the Fermi constant [17].

1.2.2 Phenomenology of neutrino interactions

The phenomenology of neutrino interactions depends both on the energy of the neutrinos and the nature of the target. Because of that, the first distinction that can be made is based on the type of particles involved. According to this, the following interaction can be identified: neutrino-electron, neutrino-nucleon and neutrino-nucleus. The introduction of neutrino masses (see Sec. 1.3), generates small kinematical effects in neutrino interaction processes, which will be neglected here [18–20].

Neutrino electron scattering

Neutrino-electron interactions are the simplest way neutrinos interact with matter. At the lowest order in weak interaction perturbation theory, they involve only free leptons, allowing their amplitude to be calculated exactly using Feynman rules. These interactions can be classified into two groups: elastic or quasi-elastic (QE), based on whether or not the final-state particles remain identical to those in the initial state.

Elastic scattering

In elastic scattering, low energy neutrinos and anti-neutrinos with flavor $\alpha = e, \mu, \tau$, interact with electrons through:

$$\nu_\alpha + e^- \to \nu_\alpha + e^- \tag{1.19}$$

$$\overline{\nu}_\alpha + e^- \to \overline{\nu}_\alpha + e^- \tag{1.20}$$

This process does not have a threshold energy, because the final-state particles are the same of those in the initial state. The only effect is a redistribution of the total energy and momentum between the particles involved.

For ν_e and $\overline{\nu}_e$, electron elastic scattering has both a CC and a NC components. Because the low energy limit is considered, the effective Lagrangian can be derived from Eq. 1.17 and Eq. 1.18, and it takes the form:

$$\begin{aligned}\mathscr{L}_{eff}(\nu_e e^- \to \nu_e e^-) = -\frac{G_F}{\sqrt{2}}\Big\{&[\overline{\nu}_e\gamma^\rho(1-\gamma^5)e][\overline{e}\gamma_\rho(1-\gamma^5)\nu_e] \\ &+ [\overline{\nu}_e\gamma^\rho(1-\gamma^5)\nu_e][\overline{e}\gamma_\rho(g_V^\ell - g_A^\ell\gamma^5)e]\Big\},\end{aligned} \tag{1.21}$$

where the first term is the CC contribution and the second one is the NC contribution. Additionally, $\gamma^5 = i\gamma^0\gamma^1\gamma^2\gamma^3$ is the chirality matrix, g_V^ℓ, g_A^ℓ are the vector and axial couplings, that can be defined using Eqs. 1.15 :

$$g_V^f = g_L^f + g_R^f = I_3^f - 2q_f \sin^2\theta_W \tag{1.22}$$

$$g_A^f = g_L^f + g_R^f = I_3^f \tag{1.23}$$

The Feynman diagrams of the process in Eq. 1.19 for ν_e are illustrated in Fig. 1.2. For $\overline{\nu}_e$, the process is very similar, but the CC contribution involves a t-channel diagram instead of an s-channel one.

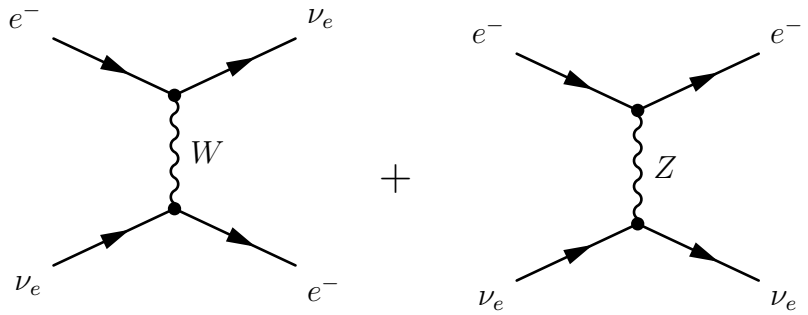

(a) *Charged current* (b) *Neutral current*

Fig. 1.2: *The two tree-level Feynman diagrams for the elastic scattering process* $\nu_e + e^- \to \nu_e + e^-$*: charged current (a) and neutral current (b).*

For ν_μ and ν_τ, the electron elastic scattering process receives a contribution only from NC. In this case, the Lagrangian is given by:

$$\mathscr{L}_{eff}(\nu_\alpha e^- \to \nu_\alpha e^-) = -\frac{G_F}{\sqrt{2}}[\overline{\nu}_\alpha\gamma^\rho(1-\gamma^5)\nu_\alpha][\overline{e}\gamma_\rho(g_V^\ell - g_A^\ell\gamma^5)e], \tag{1.24}$$

where $\alpha = \mu, \tau$ and where only the NC component is present. The Feynmann diagram of this process is shown in Fig. 1.3.

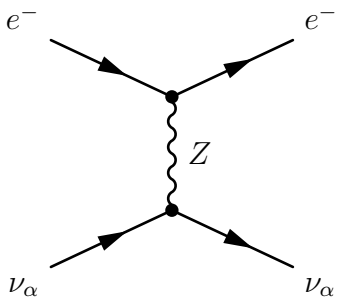

Fig. 1.3: *Tree-level Feynman diagrams for the elastic scattering process* $\nu_\alpha + e^- \to \nu_\alpha + e^-$*, with* $\alpha = \nu, \tau$*.*

From the effective Lagrangians in Eq. 1.21 and Eq. 1.24, the total neutrino-electron cross section can be derived. This cross section is proportional to the square of the

Fermi constant and to the Mandelstam variable $s = (p_\nu + p_e)^2$; $\sigma \propto G_F^2\ s$.
Considering different types of neutrinos, the following relation can be obtained:

$$\sigma_{\nu_e} : \sigma_{\overline{\nu}_e} : \sigma_{\nu_{\mu,\tau}} : \sigma_{\overline{\nu}_{\mu,\tau}} = 1 : 0.42 : 0.16 : 0.14, \tag{1.25}$$

where $\sigma_{\nu_e} \simeq 93$ s/MeV^2, in the limit $\sqrt{s} \gg m_e$. The differences between the cross sections arise from the different values of the coupling coefficients.

Quasi-elastic scattering
Muon and tau neutrinos with energy above the μ and τ production threshold can interact with electrons via quasi-elastic CC process:

$$\nu_\ell + e^- \to \nu_e + \ell^- \tag{1.26}$$

In general, the threshold for a scattering process $\nu\ + A \to \sum_X X$, where the target particle of mass m_A is at rest can be calculated by taking into account that the squared center of mass energy $\sqrt{s} = \sqrt{2E_\nu m_A + m_A^2}$ (neglecting the neutrino mass), must be bigger than $(\sum m_X)^2$. With this consideration, the neutrino energy threshold is:

$$E_\nu^{th} = \frac{(\sum m_X)^2}{2m_A} - \frac{m_A}{2}. \tag{1.27}$$

The effective Lagrangian for the QE process is:

$$\mathscr{L}_{eff}(\nu_\ell\ e^- \to \nu_e \ell^-) = -\frac{G_F}{\sqrt{2}}[\overline{\ell}\gamma^\rho(1-\gamma^5)\nu_\ell][\overline{\nu_e}\gamma_\rho(1-\gamma^5)e], \tag{1.28}$$

and the Feynman diagram is pictured in Fig. 1.4

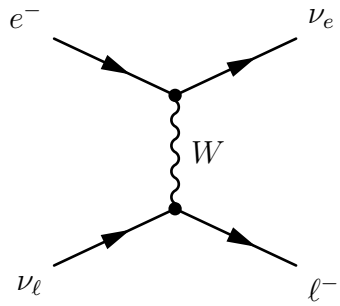

Fig. 1.4: *Tree-level Feynman diagrams for the quasi-elastic scattering process* $\nu_\ell + e^- \to \nu_e + \ell^-$.

The total cross section of this process is given in Eq. 1.29 where with $s = (p_{\nu_\ell} + p_e)^2$.

$$\sigma = \frac{G_F^2\ s}{\pi}\left(1 - \frac{m_\ell^2}{s}\right). \tag{1.29}$$

The QE process is available for both muon and tau neutrinos. However, since the mass of the tau is much larger than that of the muon, the process can occur for tau only at higher energies.

Neutrino nucleon interaction

Neutrino interactions with nucleons are characterized by a much larger cross section, but they are significantly more complex and varied than neutrino-electron interactions. These processes can be divided into three groups: elastic, in which the nucleon recoils intact from the interaction, quasi-elastic, in which the nucleon transforms into the other nucleon, and inelastic. Inelastic processes can themselves be classified into two distinct categories: resonance production and deep inelastic scattering.

Making calculations for neutrino-nucleon interactions presents additional complexity in comparison to electrons, since nucleons are compound particles. Nucleons are essentially composed of three quarks that constantly interact via gluon exchanges. These gluons, in turn, can produce other temporary quark/anti-quark pairs, resulting in a much more complex internal structure. The internal structure of the nucleon that can be resolved depends on the four-momentum of the weak boson; the higher the Q^2, the more the internal structure of the nucleon is revealed by the interaction. For this reason it is not possible, for these interactions, to calculate the exact cross-sections using Feynman diagram rules. Instead, a different approach is required. The general approach consists in representing a nucleon (i.e. hadronic) current $H_\mu^{CC/NC}$ as:

$$H_\mu^{CC} = V_\mu^{\pm} + A_\mu^{\pm} \tag{1.30}$$

$$H_\mu^{NC} = (1 - 2\sin^2\theta_W)V_\mu^0 + A_\mu^0 - 2\sin^2\theta_W V_\mu^S \tag{1.31}$$

where (V_μ) and (A_μ) are the vector and the axial-vector currents, respectively. The $\pm$ and 0 indices denote the three components of the isospin raising(-lowering) currents for the neutrino reaction. The (V_μ^S) is the isoscalar current [19].
These currents are composed of several form-factors $F(Q^2)$, which are functions of the four-momentum transfer. The selection of the necessary form-factors is interaction dependent.

NC Elastic and CC Quasi-Elastic Scattering

NC elastic processes dominate at low four-momentum transfer Q^2. NC interactions are truly elastic scattering process because the initial and final particles are the same:

$$\nu_\ell + N \to \nu_\ell + N \tag{1.32}$$

$$\overline{\nu}_\ell + N \to \overline{\nu}_\ell + N \tag{1.33}$$

where $N = n, p$ and $\ell = e, \mu, \tau$.
If the neutrino has a Q^2 high enough to create the associated charged lepton, CC interactions can take place:

$$\nu_\ell + n \to p + \ell^- \tag{1.34}$$

$$\overline{\nu}_\ell + p \to n + \ell^+ \tag{1.35}$$

These CC processes, since the nucleon changes and the neutrino produces the corresponding lepton, are more properly identified as quasi-elastic.

CC QE interactions are particularly important in neutrino physics for two reasons. First, since the nucleon recoils intact, they are the best interaction for measuring weak nucleon form-factors which are difficult or inaccessible for other scattering probes. Second, their two-body nature leads to a relative simple kinematics, that can be completely reconstructed. If the target nucleon is considered at rest, the neutrino energy E_ν can be fully determined by knowing the exiting lepton momentum p_ℓ and the angle θ_ℓ with respect to the incoming neutrino:

$$E_\nu = \frac{m_p^2 - m_n^2 - m_\ell^2 + 2m_n E_\ell}{2\left(m_n - E_\ell + |\vec{p}_\ell| \cos\theta_\ell\right)}. \tag{1.36}$$

These assumptions, however, are not entirely valid when the nucleon is within a nuclear environment (see Sec. 1.2.2).

Resonance Production (RES)
Resonance production is an inelastic interaction that dominates at low Q^2, more in detail at energies: 0.5 GeV $< E_\nu <$ 10 GeV. An example of RES is given by:

$$\begin{aligned} &\nu_\mu + N \rightarrow \mu^- \; N^* \\ &N^* \rightarrow \pi + N' \end{aligned} \tag{1.37}$$

In these interactions, the target nucleon is excited into a baryonic resonance such as N^*, the available resonance is determined by the neutrino energy. The resonance then decays, typically to a nucleon and a single pion. However, a variety of final-states can occur depending on the resonance and can include multiple pions, kaons or photons. Another example of RES is illustrated in Fig. 1.5.

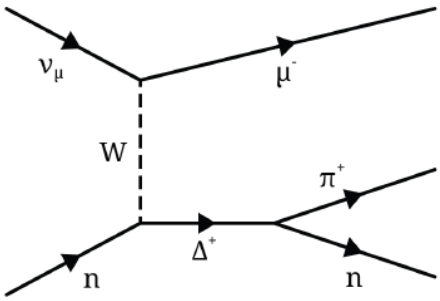

Fig. 1.5: *Feynman diagram for an example of resonance: ν_μ CC resonance single pion interaction [19].*

RES is available for all neutrino and anti-neutrino flavors and can happen via NC and CC channels, off neutrons and protons.

Deep Inelastic Scattering (DIS)
Deep inelastic scattering dominates at higher Q^2, $E_\nu >$ 10 GeV, where neutrinos have

enough energy to be able to resolve individual quarks, and fragment the nucleon. The DIS interactions can occur both via CC and NC:

$$(CC): \qquad \nu_\ell + N \to \ell^- + X\ , \qquad \overline{\nu}_\ell + N \to \ell^+ + X \tag{1.38}$$

$$(NC): \qquad \nu_\ell + N \to \nu_\ell + X\ , \qquad \overline{\nu}_\ell + N \to \overline{\nu}_\ell + X \tag{1.39}$$

where $N = p, n$ and X denotes any set of final hadrons. These scattering processes can be treated as an interaction between the neutrino and a single quark. The types of quarks with which the neutrino can scatter depends on the available Q^2: at lower values neutrino can access mostly up, down, and some strange quarks, while at higher values neutrino can access higher-mass quarks too. As a result of the DIS, the nucleon breaks up into fragments, which hadronise producing jets of strongly interacting particles. DIS processes are important because they allow us to access the inner structure of nucleons and their cross-section can be used to experimentally access the Parton Distribution Functions (PDFs) and Fragmentation Functions (FFs).

Neutrino-nucleon interactions cross sections for neutrino and antineutrino are illustrated in Fig. 1.6.

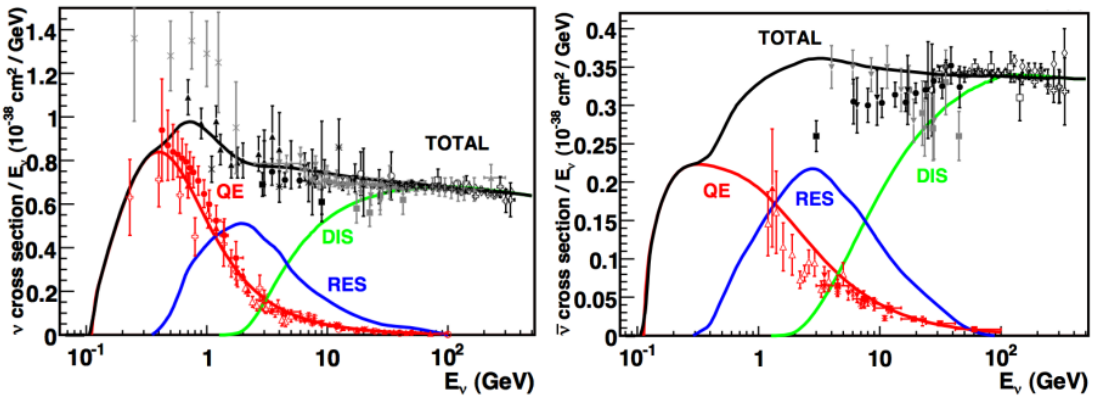

Fig. 1.6: *Muon neutrino (left) and antineutrino (right) charged-current cross-section measurements and predictions as a function of neutrino energy. The contributing processes in this energy region include quasi-elastic (QE) scattering, resonance production (RES), and deep inelastic scattering (DIS)* [21].

Nuclear effects

The description of neutrino-nucleon interactions provided so far applies exactly, only to hydrogen nuclei that consist of a single proton. In heavier nuclei, these interactions become much more complex due to various nuclear effects, which are critical for accurately interpreting modern neutrino experimental results.

The first nuclear effect is the Fermi Motion (FM). Nucleons inside the nucleus are in constant motion, affecting the kinematics and the cross-section of the interaction,

especially at low Q^2. A relativistic Fermi gas model [22] can be used in first approximation, but breaks down at low neutrino energies, therefore more complex models are required.

The second nuclear effect that has to be considered is a second order effect: the Pauli Blocking. Due to the Pauli exclusion principle, final-state nucleons can not occupy already filled states, reducing the available phase-space and so the cross-section.

The third nuclear effect is the fact that nucleons inside the nuclear medium can also behave as correlated nucleon pairs, alpha particles, or any combination of nucleons in a quasi-bound state. When a neutrino interacts with a correlated proton-neutron pair, the momentum exchange is shared by both nucleons, leading to a 2-particle 2-hole (2p2h) process, where two nucleons are ejected.

Finally, the last nuclear effect consists in the Final-State Interactions (FSI). When final-state hadrons propagate through the nuclear medium they can undergo strong interactions with the other nucleons in the medium, changing the observable final state.

All of these effects are present in all neutrino-nucleus interactions but can be ignored at high E_ν where DIS dominates and final-state particles are produced with high momenta. They are however very significant at lower momenta.

Neutrino-nucleus interaction

Another possible interaction, known as coherent scattering, involves neutrinos and a nucleus. This interaction can take place at a very low Q^2 if $QR << 1$, where R is the nuclear radius. In this interaction, the nucleus recoils as a whole, unfragmented, and it does not change its composition.

$$\nu + A_N^Z \rightarrow \nu + A_N^{*Z} \tag{1.40}$$

The coherent scattering cross section is proportional to the square of the atomic mass number A^2. At low E_ν, coherent scattering is only available as NC, while at higher energies both NC and CC processes are possible. In the first case, the only effect of the interaction is a slight recoil of the nucleus, while in the second case additional final-state particles, such as π, ρ, K mesons, can be produced. Because of the low Q^2, coherent scattering processes have a relatively low cross sections.

1.3 Neutrino Beyond the Standard Model

SM predicts neutrinos to be massless, but experimental evidence such as flavor neutrino oscillations and studies on cosmological observables, i.e. anisotropies of the cosmic microwave background or the distribution of large-scale structure [23], show that neutrinos have small mass. Neutrino mass is nowadays the only experimental evidence of physics beyond the standard model.

1.3.1 Neutrino Oscillations

The concept of neutrino oscillations was initially proposed by Pontecorvo in 1957 [24]. He introduced neutrino-antineutrino oscillations imitating those of the kaon-antikaon system. Later, the possibility of a neutrino changing from one flavor to another was also suggested, and the Pontecorvo's hypothesis was improved by Maki, Nakagawa and Sakata [25]. Hints of this phenomenon have existed since the earliest measurements of the solar neutrino flux in the 1970s. In fact, experiments such as Homestake [26], than GALLEX [27] and SAGE [28] measured a neutrino flux coming from the Sun, to be smaller than the one predicted by the Solar Standard Model developed by Bahcall and Davis [29]. This anomaly was called *solar neutrino problem*. The clear experimental evidence of neutrino oscillations was obtained in 1998 by Super Kamiokande [30], which measured ν_e and ν_μ coming from the atmosphere. Neutrino oscillation discovery was later confirmed by other experiments using artificial neutrino beams. Some of them are: KamLAND in 2002 [31], a reactor neutrino experiment that exploited electron antineutrinos coming from a nuclear reactor, K2K [32] and MINOS [33], that used muon neutrino beam produced by accelerated protons.

Flavor neutrino oscillation is a quantum-mechanic phenomenon in which a neutrino produced with a specific initial flavor ν_α may be detected with a different flavor ν_β after traveling a certain distance. This behavior, as explained below, is directly related to the fact that neutrinos are massive particles.

The physical states of particles, known as mass eigenstates, are stationary solutions of the free particle Hamiltonian:

$$\hat{H}\psi = i\frac{\partial\psi}{\partial t} = E\psi. \tag{1.41}$$

The time evolution of the mass eigenstates takes the form:

$$\psi(\mathbf{x}, t) = \phi(\mathbf{x})e^{-iEt}. \tag{1.42}$$

Neutrinos have three mass eigenstates ν_1, ν_2, ν_3, but as said in Sec. 1.2.1, neutrinos are eigenstates of the weak interaction so they also have 3 flavor states: ν_e, ν_μ, ν_τ. The neutrino mass eigenstates do not correspond to the flavor eigenstates. Instead, each neutrino flavor is a coherent linear combination of ν_1, ν_2 and ν_3 [10]. The relationship between the flavor and mass eigenstates can be described using the Pontecorvo-Maki-Nakagawa-Sakata (PMNS) unitary mixing matrix as:

$$\begin{pmatrix}\nu_e\\ \nu_\mu\\ \nu_\tau\end{pmatrix} = U_{\text{PMNS}}\begin{pmatrix}\nu_1\\ \nu_2\\ \nu_3\end{pmatrix} = \begin{pmatrix}U_{e1} & U_{e2} & U_{e3}\\ U_{\mu1} & U_{\mu2} & U_{\mu3}\\ U_{\tau1} & U_{\tau2} & U_{\tau3}\end{pmatrix}\begin{pmatrix}\nu_1\\ \nu_2\\ \nu_3\end{pmatrix}. \tag{1.43}$$

Knowing that the neutrino flavor state is produced as a linear combination of mass eigenstates:

$$|\nu_\alpha\rangle = \sum_i U_{\alpha i}\,|\nu_i\rangle \qquad\qquad \alpha = e, \mu, \tau \qquad i = 1, 2, 3 \tag{1.44}$$

when the neutrino propagates, each mass eigenstate propagates as a free relativistic plane wave, each one with its own phase:

$$|\nu_\alpha(t)\rangle = \sum_i U_{\alpha i} e^{-iE_i t} |\nu_i\rangle \,, \tag{1.45}$$

where $E_i = \sqrt{\vec{p}^2 + m_i^2}$ is the relativistic energy expressed in natural units. Since phases depend on masses m_i, if the three neutrino masses are different, the wave functions can interfere. This means that if a flavor state produced at t_0 is described by a specific linear combination of mass eigenstates, then at a later time t, it will be described by a different new linear combination. This gives rise to the phenomenon of neutrino flavor oscillations.

Oscillations in vacuum

The oscillation probability (i.e. the probability to detect a flavor that is different with respect to the initial one) in vacuum can be calculated as follows.
Considering a flavor state:

$$|\nu_\alpha\rangle = \sum_i U_{\alpha i} |\nu_i\rangle \,, \tag{1.46}$$

it is connected to the massive state via the unitary matrix U_{PMNS}:

$$|\nu_i\rangle = \sum_\alpha U^*_{\alpha i} |\nu_\alpha\rangle \,. \tag{1.47}$$

Substituting the mass state (Eq. 1.47) into the time evolution (Eq. 1.45), we obtain:

$$|\nu_\alpha(t)\rangle = \sum_\beta \left(\sum_i U^*_{\alpha i} e^{-iE_i t} U_{\beta i} \right) |\nu_\beta\rangle \,. \tag{1.48}$$

The amplitude of the $\nu_\alpha \to \nu_\beta$ transitions is:

$$A_{\nu_\alpha \to \nu_\beta}(t) = \langle \nu_\beta | \nu_\alpha(t) \rangle = \sum_i U^*_{\alpha i} U_{\beta i} e^{-iE_i t}, \tag{1.49}$$

so the transition probability is given by:

$$P_{\nu_\alpha \to \nu_\beta}(t) = |A_{\nu_\alpha \to \nu_\beta}(t)|^2 = \sum_{i,j} U^*_{\alpha i} U_{\beta i} U_{\alpha j} U^*_{\beta j} e^{-i(E_i - E_j)t}. \tag{1.50}$$

Due to their tiny masses, neutrinos are always ultra-relativistic, so their energy can be approximated as:

$$E_i \simeq E + \frac{m_i^2}{2E}. \tag{1.51}$$

In this case,

$$E_i - E_j \simeq \frac{\Delta m^2_{ij}}{2E} \qquad \text{with} \qquad \Delta m^2_{ij} \equiv m_i^2 - m_j^2 \qquad \text{and} \qquad E = |\vec{p}|. \tag{1.52}$$

Therefore, the transition probability (Eq. 1.50) takes the form:

$$P_{\nu_\alpha \to \nu_\beta}(t) = \sum_{i,j} U^*_{\alpha i} U_{\beta i} U_{\alpha j} U^*_{\beta j} \exp\left(-i \frac{\Delta m^2_{ij} t}{2E}\right). \tag{1.53}$$

Since neutrinos propagate almost at the speed of light, in natural units it is possible to approximate $t = L$, leading to:

$$P_{\nu_\alpha \to \nu_\beta}(L, E) = \sum_{i,j} U^*_{\alpha i} U_{\beta i} U_{\alpha j} U^*_{\beta j} \exp\left(-i \frac{\Delta m^2_{ij} L}{2E}\right). \tag{1.54}$$

The oscillation probability can also be written as:

$$\begin{aligned} P_{\nu_\alpha \to \nu_\beta}(L, E) = \delta_{\alpha\beta} &- 4 \sum_{i>j} Re(U^*_{\alpha i} U_{\beta i} U_{\alpha j} U^*_{\beta j}) \sin^2\left(\frac{\Delta m^2_{ij} L}{4E}\right) \\ &+ 2 \sum_{i>j} Im(U^*_{\alpha i} U_{\beta i} U_{\alpha j} U^*_{\beta j}) \sin\left(\frac{\Delta m^2_{ij} L}{2E}\right). \end{aligned} \tag{1.55}$$

Analogously, for antineutrinos it can be written:

$$\begin{aligned} P_{\overline{\nu}_\alpha \to \overline{\nu}_\beta}(L, E) = \delta_{\alpha\beta} &- 4 \sum_{i>j} Re(U^*_{\alpha i} U_{\beta i} U_{\alpha j} U^*_{\beta j}) \sin^2\left(\frac{\Delta m^2_{ij} L}{4E}\right) \\ &- 2 \sum_{i>j} Im(U^*_{\alpha i} U_{\beta i} U_{\alpha j} U^*_{\beta j}) \sin\left(\frac{\Delta m^2_{ij} L}{2E}\right). \end{aligned} \tag{1.56}$$

The oscillation probability when $\alpha \neq \beta$ is called *transition probability*, whereas when $\alpha = \beta$ it is called *survival probability*. The last one is defined as:

$$P_{\nu_\alpha \to \nu_\alpha}(t) = 1 - P_{\nu_\alpha \to \nu_\beta}(t), \tag{1.57}$$

and it takes the form:

$$P_{\nu_\alpha \to \nu_\alpha}(L, E) = 1 - 4 \sum_{i>j} |U_{\alpha i}|^2 |U_{\alpha j}|^2 \sin^2\left(\frac{\Delta m^2_{ij} L}{4E}\right). \tag{1.58}$$

Two-flavor scenario

The simplest case of neutrino flavor oscillations is the two-flavor approximation, in which only two flavors are considered, and the mixing matrix U is a 2×2 rotation. This approximation is useful for two reasons: the oscillation formula is much easier and depends on fewer parameters than the three-flavor scenario; moreover, because many experiments lack sensitivity to three-neutrino mixing effects, the data can be interpreted within an effective two-neutrino model. In this scenario, the flavor states can be expressed as functions of the mass states as:

$$|\nu_\alpha\rangle = \cos\theta\, |\nu_i\rangle + \sin\theta\, |\nu_j\rangle\,, \tag{1.59}$$

$$|\nu_\beta\rangle = -\sin\theta\, |\nu_i\rangle + \cos\theta\, |\nu_j\rangle\,. \tag{1.60}$$

In this case, the oscillation probability takes, in natural units, the form:

$$P_{\nu_\alpha \to \nu_\beta}(t) = \sin^2 2\theta \sin^2 \left(\frac{\Delta m^2_{ij} L}{4E} \right), \tag{1.61}$$

writing L in km, Δm^2 in eV^2 and the neutrino energy in GeV, Eq. 1.61 can be written as:

$$P_{\nu_\alpha \to \nu_\beta}(t) = \sin^2 2\theta \sin^2 \left(1.27 \frac{\Delta m^2_{ij} L}{E} \right). \tag{1.62}$$

Moreover, considering the oscillation probability (Eq. 1.62), the oscillation length can be defined as the value of L for which the transition probability is maximal, i.e. $\sin^2 X = 1$:

$$L^{osc} = 2.47 \ \frac{E \ [\text{GeV}]}{\Delta m^2 \ [\text{eV}^2]} \ \text{km} \ . \tag{1.63}$$

The transition probability (Eq. 1.62) for $\sin^2 2\theta = 1$ as a function of $L/E \ \Delta m^2$, is shown by the dashed line in Fig. 1.7. In the same figure, the oscillation length in Eq. 1.63 corresponds to the location of the first dip of the transition probability at $L/E = 2.47$. In real experiments, it is not possible to measure the oscillation probabilities for exact values of the neutrino propagation distance L and the neutrino energy E. This is because both the neutrino source and the detection processes have some spatial and energy uncertainties: the source is not monochromatic, and the detector has a finite energy resolution. Therefore, in practice, the oscillation probability needs to be averaged over an appropriate distribution $\phi(L/E)$ of L/E. A possible distribution can be a Gaussian with average $\langle L/E \rangle$ and standard deviation $\sigma_{L/E}$. The average probability takes the form:

$$\langle P_{\nu_\alpha \to \nu_\beta}(L/E) \rangle = \frac{1}{2} \sin^2 2\theta \left[1 - \left\langle \cos \left(\frac{\Delta m^2 L}{2E} \right) \right\rangle \right], \tag{1.64}$$

with

$$\left\langle \cos \left(\frac{\Delta m^2 L}{2E} \right) \right\rangle = \int \cos \left(\frac{\Delta m^2 L}{2E} \right) \phi \left(\frac{L}{E} \right) d\frac{L}{E}. \tag{1.65}$$

CP violation

Considering $\hat{C}$ the charge operator, that transforms a particle into an antiparticle, and considering $\hat{P}$ the parity operator, that reverses the spatial component of the wave function, the charge-parity operator $\hat{CP}$ can be introduced. $\hat{CP}$ invariance in neutrino physics would imply:

$$P(\nu_\alpha \to \nu_\beta) = P(\overline{\nu}_\alpha \to \overline{\nu}_\beta). \tag{1.66}$$

A possible violation of parity, i.e. a different behavior of ν and $\bar{\nu}$, can be revealed by measuring a non-zero value of the asymmetry:

$$A^{CP}_{\alpha\beta} = P(\nu_\alpha \to \nu_\beta) - P(\overline{\nu}_\alpha \to \overline{\nu}_\beta). \tag{1.67}$$

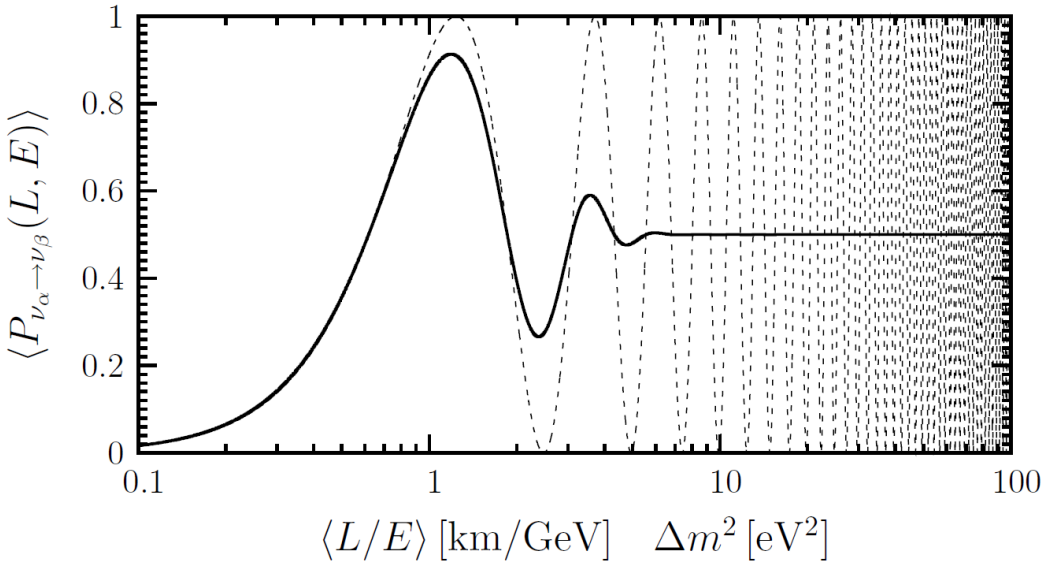

Fig. 1.7: *Probability of* $\nu_\alpha \to \nu_\beta$ *transitions for* $\sin^2 2\theta = 1$ *as a function of* $\langle L/E \rangle$ *[km/GeV]* Δm^2*. Solid line: transition probability averaged over a Gaussian* L/E *distribution. Dashed line: transition probability in Eq. 1.62, with* $L/E = \langle L/E \rangle$ [17].

Taking into account the oscillation probabilities in Eqs. 1.55 and 1.56, the asymmetry can be written as:

$$A^{CP}_{\alpha\beta} = 4 \sum_{i>j} Im(U^*_{\alpha i} U_{\beta i} U_{\alpha j} U^*_{\beta j}) \sin^2 \left(\frac{\Delta m^2_{ij} L}{4E} \right). \tag{1.68}$$

It is important to note that the CP asymmetry can be measured only in the transition between different flavors, since the imaginary part of Eq. 1.68 vanishes for $\alpha = \beta$.

Oscillations in matter

A different description is needed to describe neutrino propagation in matter. When neutrinos travel in matter, they can interact with electrons and nuclei of the medium, and these interactions modify the oscillation probability. This phenomenon is called Mikheyev-Smirnov-Wolfenstein (MSW) effect, also known as matter effect [34]. The MSW effect occurs because all neutrino flavors can participate in NC interactions with electrons, but only electron neutrinos can participate in CC interactions. As a result, the impact of matter on neutrino propagation depends on the neutrino flavor. This effect can be described by adding potentials in the Hamiltonian, that depend on the density of the medium; CC potential and NC potential are respectively:

$$V_{CC} = \pm \sqrt{2} G_F n_e, \qquad V_{NC} = \mp \frac{\sqrt{2}}{2} G_F n_n, \tag{1.69}$$

where G_F is the Fermi constant, n_e is the electron density, and n_n is the neutron density of the medium. Introducing these new potentials, the Hamiltonian in matter, in the

simplest case of two-flavor approximation (e and μ), is [35]:

$$\mathcal{H}_M = \mathcal{H}_{Vac} + V_{CC}\begin{pmatrix}1 & 0\\ 0 & 0\end{pmatrix} + V_{NC}\begin{pmatrix}1 & 0\\ 0 & 1\end{pmatrix}, \tag{1.70}$$

in which $\mathcal{H}_{Vac}$ is the Hamiltonian in vacuum that takes the form:

$$\mathcal{H}_{Vac} = \frac{\Delta m^2}{4E}\begin{pmatrix}-\cos 2\theta & \sin 2\theta\\ \sin 2\theta & \cos 2\theta\end{pmatrix}. \tag{1.71}$$

Since the last term of Eq. 1.70 does not affect the oscillation because it acts equally on both flavors, it can be neglected; so $\mathcal{H}_M$ becomes:

$$= \mathcal{H}_{Vac} + \frac{V_{CC}}{2} + \frac{V_{CC}}{2}\begin{pmatrix}1 & 0\\ 0 & -1\end{pmatrix}. \tag{1.72}$$

Considering Eq. 1.72 and Eq. 1.71, the matter Hamiltonian is:

$$\mathcal{H}_M = \frac{\Delta m^2}{4E}\begin{pmatrix}-(\cos 2\theta - \zeta) & \sin 2\theta\\ \sin 2\theta & (\cos 2\theta - \zeta)\end{pmatrix}, \tag{1.73}$$

where

$$\zeta \equiv \frac{V_{CC}}{\Delta m^2/4E} = \frac{2\sqrt{2G_F}n_e E}{\Delta m^2}. \tag{1.74}$$

In this scenario, the oscillation probability takes the form:

$$P_{\nu_e\to\nu_\mu}(t) = \sin^2 2\theta_M \sin^2\left(\frac{\Delta m^2_M L}{4E}\right), \tag{1.75}$$

where the effective angle θ_M and the effective mass difference Δm^2_M are:

$$\begin{aligned}\Delta m^2_M &= \Delta m^2_V \sqrt{\sin^2(2\theta) + (\cos 2\theta - \zeta)^2}\\ \sin^2 2\theta_M &= \frac{\sin^2 2\theta}{\sin^2 2\theta + (\cos 2\theta - \zeta)^2}\end{aligned} \tag{1.76}$$

in which Δm_V is the mass difference in vacuum. The parameter ζ is particularly relevant because it is sensitive to the sign of the mass square difference, so it can be used to partially resolve the mass hierarchy. In fact, a positive mass difference Δm^2_{21} was measured, which means that m_2 is greater than m_1 [36]. However, the relative ordering between these two states and the third mass state m_3 is still unknown, leading to two different scenarios. In the normal hierarchy (NH) or normal ordering (NO), m_3 is heavier than m_1 and m_2, while in the inverted hierarchy (IH) or inverted ordering (IO), it is the lightest. These two hypotheses are illustrated in Fig. 1.8.

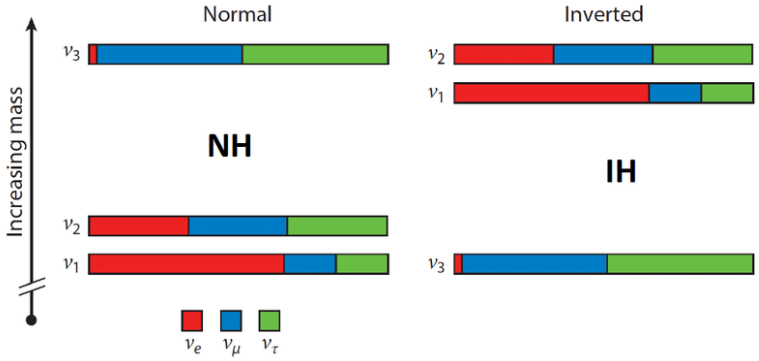

Fig. 1.8: *On the left, Normal Hierarchy (NO) where the heavies mass state is ν_3. On the right, the Inverted Hierarchy (IO) where ν_3 is the lightest mass state* [37].

1.3.2 Oscillation experiment

Neutrino oscillation experiments are divided into many categories according to different features. Firstly, they can be distinguished into appearance and disappearance experiments. Appearance experiments measure transitions between different neutrino flavors, while disappearance experiments measure the survival probability of a neutrino flavor by counting the number of interactions in the detector.
A second distinction can be made by considering the types of neutrino source:

- **Reactor experiments**: employ large isotropic fluxes of electron antineutrinos produced in nuclear reactors.
- **Accelerator experiments**: employ beams of neutrinos or antineutrinos produced by decay of pions, kaons, and muons created by a proton beam hitting a target.
- **Solar neutrino experiments (SOL)**: employ electron neutrinos generated in the core of the Sun by the thermonuclear reactions that power it.
- **Atmospheric neutrino experiments (ATM)**: employ neutrinos coming from primary cosmic rays. Primary cosmic rays interact with the upper layers of the atmosphere producing a large flux of pions and kaons that decay in the atmosphere into muons and neutrinos. Many muons further decay into electrons and neutrinos before hitting the ground.

Neutrino oscillation experiments are also classified according to the average value of the ratio L/E where L is the distance between the detector and the source, and E the neutrino energy. Since the value of Δm^2 is a fixed property of nature, different experiments can be designed with appropriate L/E to be sensitive to different Δm^2. So, the ratio L/E determines the *sensitivity* to Δm^2 which is defined as the value of Δm^2 for which:

$$\frac{\Delta m^2 L}{2E} \sim 1. \tag{1.77}$$

Type of experiment	L	E	Δm^2 sensitivity
Reactor SBL	~ 10 m	~ 1 MeV	~ 0.1 eV^2
Accelerator SBL	~ 1 km	$\gtrsim 1$ GeV	$\gtrsim 1$ eV^2
	~ 10 m	~ 10 MeV	~ 1 eV^2
	~ 1 km	$\sim 10^2$ GeV	$\sim 10^2$ eV^2
Reactor LBL	~ 1 km	~ 1 MeV	$\sim 10^{-3}$ eV^2
Accelerator LBL	$\sim 10^3$ km	$\gtrsim 1$ GeV	$\gtrsim 10^{-3}$ eV^2
ATM	20–10^4 km	0.5–10^2 GeV	$\sim 10^{-4}$ eV^2
Reactor VLB	$\sim 10^2$ km	~ 1 MeV	$\sim 10^{-5}$ eV^2
Accelerator VLB	$\sim 10^4$ km	$\gtrsim 1$ GeV	$\gtrsim 10^{-4}$ eV^2
SOL	$\sim 10^{11}$ km	0.2–15 MeV	$\sim 10^{-12}$ eV^2

Tab. 1.3: *Types of neutrino oscillation experiments with their typical source–detector distance, energy, and sensitivity to* Δm^2.

According to L , also called baseline, it is possible to identify: short baseline experiments (SBL), long baseline experiments (LBL) and very long baseline experiments (VLB).
A summary of neutrino oscillation experiments with their typical source–detector distance, energy, and sensitivity to Δm^2, is illustrated in Tab. 1.3.

1.3.3 Neutrino masses

Although neutrinos are known to have mass, the exact mechanism by which they acquire it remains unknown, and several hypotheses have been proposed.

A possible approach consists in a minimal extension of the Standard Model in which a right-handed neutrino ν_R and left-handed antineutrino $\overline{\nu}_L$ are introduced, and a Lagrangian mass term can be built as:

$$\mathscr{L}_D = -m_D(\overline{\nu}_L\nu_R + \overline{\nu}_R\nu_L). \tag{1.78}$$

In this scenario, the neutrino acquires mass via spontaneous symmetry breaking as all other particles in the SM. Here, neutrinos and antineutrinos are Dirac particles i.e. they are different particles $\nu \neq \bar{\nu}$. Right-handed neutrinos are called sterile neutrinos because they do not interact weakly, and left-handed neutrinos are called active neutrinos, which are the ones experimentally observed.

In another hypothesis, the neutrino is a Majorana particle i.e neutrino ad antineutrino are the same particle $\nu = \bar{\nu}$. Under this assumption, neutrinos are described using only left-handed components. The mass term of the Lagrangian is:

$$\mathscr{L}_{M,L} = -\frac{1}{2}m_L(\overline{\nu}^c_L\nu_L + \overline{\nu}_L\nu^c_L), \tag{1.79}$$

where $\nu_L^c = C\,\overline{\nu}_L^T$ and C is the charge-conjugation operator.

One more hypothesis consists of a unified approach, where the Dirac mass term and two Majorana mass terms for left and right chirality are introduced. In this case, the Lagrangian is:

$$\mathscr{L}_{D+M} = \mathscr{L}_D + \mathscr{L}_{M,L} + \mathscr{L}_{M,R} = -\frac{1}{2}(\overline{\nu}_L \quad \overline{\nu}_R^c) \begin{pmatrix} m_L & m_D \\ m_D & m_R \end{pmatrix} \begin{pmatrix} \nu_L \\ \nu_R^c \end{pmatrix} \; + \; h.c. \tag{1.80}$$

The mass matrix can be diagonalized obtainig on the diagonal the mass terms m_1 and m_2:

$$m_{2,1} = \frac{1}{2}\left[m_L + m_R \pm \sqrt{(m_L - m_R)^2 + 4m_D^2}\right]. \tag{1.81}$$

A particular case of this approach is when $m_L = 0$ e $m_D \ll m_R$, which implies:

$$m1 \simeq \frac{m_D^2}{m_R}\,, \qquad\qquad m_2 \simeq m_R. \tag{1.82}$$

This case is called *Type-I Seesaw*. In this scenario, m_2 is associated to a very massive and sterile (i.e. non-interacting) neutrino, while m_1 is associated to a lighter neutrino which could be the experimentally observed one. Type-I seesaw mechanism is relevant because it provides an explanation for the smallness of neutrino masses. Moreover, it can agree with the SM under the assumption that m_R is at the GUT scale ($\sim 10^{16}$ GeV).

Although a direct measurement of neutrino masses is theoretically possible using kinematical methods, we are currently unable to determine their absolute value. So far, only upper limits have been measured.

For the electron neutrino the best limit is set by KATRIN [38], which measures the neutrino mass by studying the energy and the count rate of electrons emitted in tritium beta decay:

$$m_{\nu_e} < 0.8 \quad \text{eV} \qquad\qquad \text{at} \qquad 90\% \quad \text{C.L.}$$

It is important to note that due to neutrino mixing, the measured quantity is the value $m_\beta^2 = \sum_k |U_{ek}|^2 m_k^2$.

For muon and tau neutrinos, the upper limit is obtained by studying, respectively, the pion and the τ decay kinematics:

$$m_{\nu_\mu} < 0.19 \quad \text{MeV} \qquad\qquad \text{at} \qquad 90\% \quad \text{C.L.}$$

$$m_{\nu_\tau} < 18.2 \quad \text{MeV} \qquad\qquad \text{at} \qquad 95\% \quad \text{C.L.}$$

An other decay from which a limit on neutrino mass can be extracted is the *neutrinoless double beta decay* ($0\nu\beta\beta$) illustrated in Fig. 1.9. Since this decay requires a $\nu \to \bar{\nu}$ transition, which is possible only if neutrinos are Majorana particles, $0\nu\beta\beta$ can be considered a golden channel because it could probe the neutrino nature and

also measure its mass. Nowadays $0\nu\beta\beta$ has not been discovered yet; however its non observation allows to set the following limit:

$$\langle m_{\beta\beta}\rangle = |\sum_i U_{ei}^2 m_i| < 0.036 - 0.156 \qquad \text{eV}$$

This limit is set by measuring the half-life of the decay, which is linked to the neutrino mass by the relation:

$$(T_{\frac{1}{2}}^{0\nu})^{-1} = G^{0\nu}|M^{0\nu}|\left(\frac{m_{\beta\beta}}{m_e}\right)^2, \tag{1.83}$$

where $G^{0\nu}$ is the phase space integral taking into account the final atomic state and $|M^{0\nu}|$ is the nuclear matrix element of the transition [39].

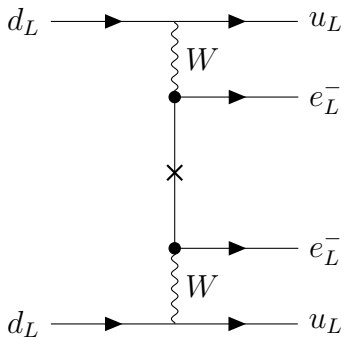

Fig. 1.9: *Feynman diagram for neutrinoless double beta decay* $(A, Z) \to (A, Z+2) + e^- + e^-$*, with a Majorana neutrino.*

Finally, a limit on the sum of all neutrino masses can be obtained from cosmological measurements [40]:

$$\sum_i m_i < 0.07 - 0.12 \quad \text{eV} \qquad \text{at} \qquad 95\% \quad \text{C.L.}$$

Massive neutrinos are difficult to cluster due to their relatively high velocity; as a result, they suppress clustering of matter on scales smaller than the free-streaming scale.[3] This effect can be observed as a suppression of the matter power spectrum $P(k) = \langle|\delta_k|^2\rangle$ i.e. the Fourier transform of the density contrast $\delta(\mathtt{x}) = \frac{\rho(\mathtt{x})-\bar{\rho}}{\bar{\rho}}$ with ρ matter density field.

[3]The free-streaming scale is the co-moving length scale below which neutrinos can move freely without being trapped by gravitational potentials.

1.4 State of art

The U_{PMNS} matrix, in the case of three neutrinos, can be factorized and parameterized as follows:

$$U_{\text{PMNS}} = \begin{pmatrix} U_{e1} & U_{e2} & U_{e3} \\ U_{\mu 1} & U_{\mu 2} & U_{\mu 3} \\ U_{\tau 1} & U_{\tau 2} & U_{\tau 3} \end{pmatrix} = \begin{pmatrix} 1 & 0 & 0 \\ 0 & c_{23} & s_{23} \\ 0 & -s_{23} & c_{23} \end{pmatrix} \begin{pmatrix} c_{13} & 0 & s_{13}e^{-i\delta_{CP}} \\ 0 & 1 & 0 \\ -s_{13}e^{i\delta_{CP}} & 0 & c_{13} \end{pmatrix} \begin{pmatrix} c_{12} & s_{12} & 0 \\ -s_{12} & c_{12} & 0 \\ 0 & 0 & 1 \end{pmatrix}.$$

The submatrices account for the mixing between two different states. In the matrices $c_{ij} = \cos\theta_{ij}$, $s_{ij} = \sin\theta_{ij}$, with θ_{ij} mixing angles and δ_{CP} is the Dirac phase.
This phase is directly related to the violation of CP because: $\not{CP} \implies U^* \neq U$ which means that if CP is violated, then δ_{CP} should be different from 0 and π. Current measurements of this parameter lack the precision necessary to definitively determine whether the neutrino oscillation CP violation exists. The current fit for δ_{CP} is illustrated in Fig. 1.10, where it is possible to note different results for different experiments.

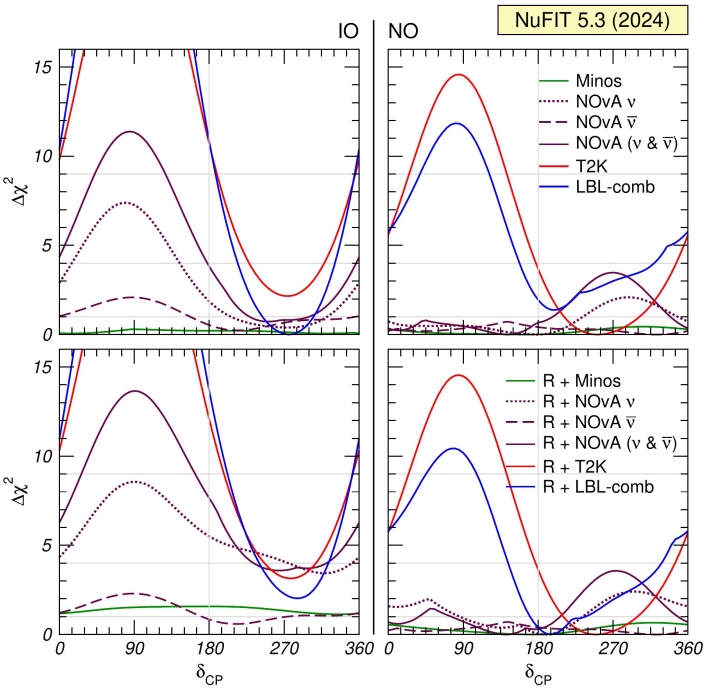

Fig. 1.10: $\Delta\chi^2$ *profiles as a function of* δ_{CP}*. IO on the left and NO on the right. On top/bottom results with/without reactor experiments.* [41].

Thanks to neutrino oscillation experiments, the three mixing angles have been measured with varying degrees of precision, as well as the mass-squared differences. These parameters were first measured using the following experiments[4]:

- $\sin^2\theta_{23}$, in long-baseline accelerator and atmospheric neutrino experiments.

[4]nowadays these measurements can be done all in the same experiment

- $\sin^2\theta_{13}$, in reactor neutrino and in long-baseline accelerator experiments.
- Δm^2_{31}, in long-baseline accelerator and atmospheric neutrino experiments.
- $\sin^2\theta_{12}$ and Δm^2_{21}, in solar neutrino experiments.

The best results currently available for neutrino parameters are summarized in Tab. 1.4.

Parameter	**World Average**	**Mass Ordering**
$\sin^2\theta_{12}$	0.307 ± 0.013	
$\sin^2\theta_{23}$	0.539 ± 0.022	Inverted
$\sin^2\theta_{23}$	0.546 ± 0.021	Normal
$\sin^2\theta_{13}$	$(2.20 \pm 0.07) \times 10^{-2}$	
Δm^2_{21}	$(7.53 \pm 0.18) \times 10^{-5}$ eV^2	
Δm^2_{32}	$(-2.536 \pm 0.034) \times 10^{-3}$ eV^2	Inverted
Δm^2_{32}	$(2.456 \pm 0.033) \times 10^{-3}$ eV^2	Normal
δ_{CP}	$1.36^{+0.20}_{-0.16}\pi$ rad	

Tab. 1.4: Summary of best currently available experimental results for neutrino parameters [9].

Despite these measurements, our understanding of neutrino physics remains incomplete and many questions are still unresolved. As already mentioned in Sec. 1.3.1, the sign of Δm^2_{21} has been measured by exploiting the matter effect of solar neutrino experiment, allowing the mass hierarchy between m_1 and m_2 to be determined. However, the same measurement cannot be made for Δm^2_{31}, since in atmospheric experiments the matter effect is too small to be considered. As a result, the sign of Δm^2_{31} remains unknown, as well as the total mass hierarchy. The current global fit obtained from long-baseline experiments, reactor, and solar neutrino experiments in Fig. 1.11 show a preference towards the normal mass ordering.
In addition, also the octant of θ_{23}, i.e. whether $\sin^2\theta_{23} < 0.5$ or $\sin^2\theta_{23} > 0.5$, remains unknown. For this parameter the current fits are shown in Fig. 1.12.
Moreover, as mentioned earlier, the absolute mass and the real nature of neutrinos are still unknown.
Furthermore, nothing is known about the possible existence of sterile neutrinos. Some experiments such as LNSD, GALLEX and other reactor experiments reported anomalies that could hint at a fourth, sterile neutrino. However, so far no evidence of these neutrinos exists.

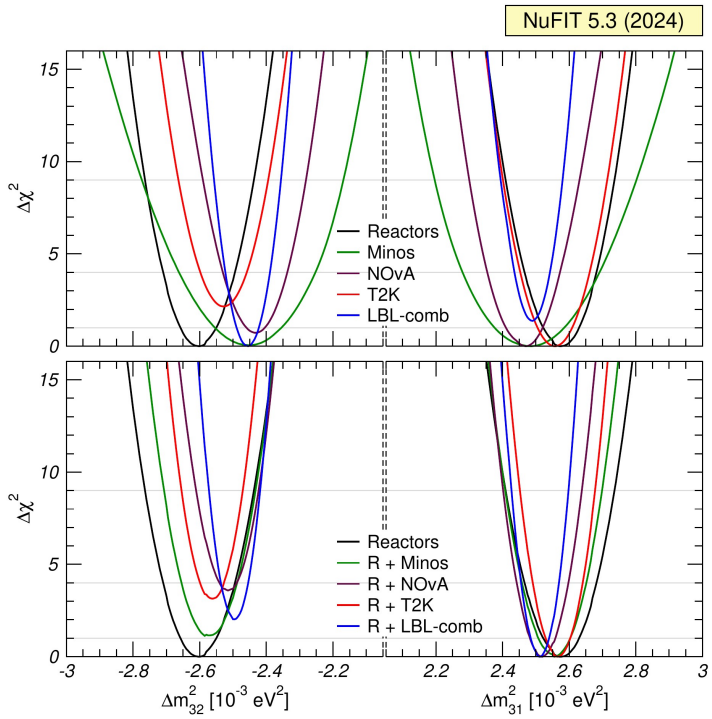

Fig. 1.11: $\Delta\chi^2$ *profiles as a function of* $\Delta m^2_{3\ell}$. *IO on the left and NO on the right. From the minimum of the curves, a preference for the NO can be seen* [41].

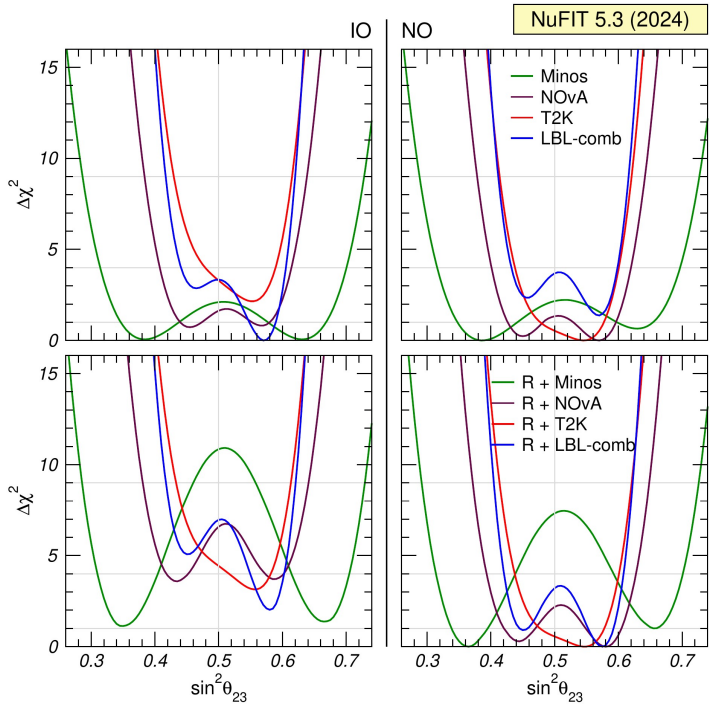

Fig. 1.12: $\Delta\chi^2$ *profiles as a function of* $\Delta m^2_{3\ell}$. *IO on the left and NO on the right. From the minimum of the curves, a preference for the NO can be seen* [41].

Chapter 2

Deep Underground Neutrino Experiment

2.1 Introduction

The Deep Underground Neutrino Experiment (DUNE) is a next-generation long baseline neutrino oscillation experiment, one of its primary objectives is to investigate the matter-antimatter asymmetry in the universe by studying the CP violation phase δ_{CP} in neutrino oscillations. DUNE also aims to determine the neutrino mass ordering and to measure the neutrino mixing parameters with unprecedented precision. Another key goal of the experiment is to detect and analyze neutrinos emitted during core-collapse supernovae in our galaxy, if one were to happen within the lifetime of the experiment, which carry with them the potential for great insight into the evolution of the universe. Additionally, DUNE will search for signs of proton decay, a phenomenon predicted by grand unified theories. To achieve its goals, DUNE, hosted by the U.S. Department of Energy's Fermilab, consists of two neutrino complex detectors: a Far Detector (FD) and a Near Detector (ND). The ND will be located at Fermilab in Illinois, while the FD will be located at the Sanford Underground Research Facility (SURF) in South Dakota, USA, at a distance of 1300 km from Fermilab. The detectors will be exposed to the world's most intense neutrino beam originating at Fermilab [42]. In Fig. 2.1 the experimental setup of DUNE is schematically illustrated.
In this chapter, the design and the main goals of DUNE are presented.

2.2 Design

DUNE comprises three central components: a high-intensity neutrino source generated from a megawatt-class proton accelerator at Fermilab, a massive far detector (FD), and a composite near detector (ND) installed just downstream of the neutrino source. To fully achieve its goals, DUNE will undergo two consecutive phases:

- **Phase-I**: in the first phase a 1.2 MW proton beam will be used, the FD will be

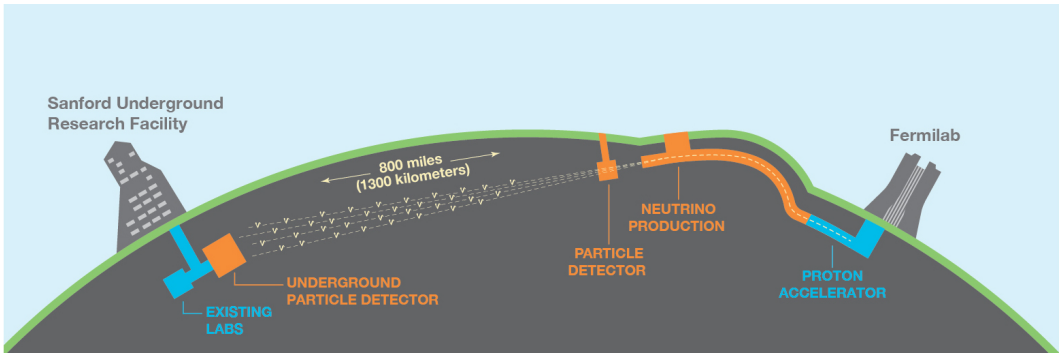

Fig. 2.1: *Schematic DUNE experimental set-up. On the right, the Fermilab with the beamline and the near detector. On the left, the far detector situated in South Dakota* [43].

composed of only two modules with a total fiducial mass of 20 kt, and the ND will include three subdetectors, i.e. ND-Lar, TMS and SAND.

- **Phase-II**: in the second phase the beam will be upgraded to 2.4 MW, the FD will be expanded to four modules with a total fiducial mass of 40 kt, and in the ND, TMS will be replaced by a new subdetector called ND-GAr.

2.2.1 Neutrino beam

DUNE's detectors will be exposed to the the world's most intense neutrino beam provided by the Long-Baseline Neutrino Facility (LBNF) at Fermilab as explained below.

A proton beam in a wide energy range of 60-120 GeV is extracted from Fermilab's Main Injector (MI) synchrotron, and transported to the target area by a series of dipole and quadrupole magnets. In this area, the protons reach the target, which is a long and thin set of graphite segments in which about 85% of the protons interact and produce secondary particles, predominantly pions $\pi^{\pm}$ and kaons $K^{\pm}$. Secondary particles are focused by two magnetic horns before they enter a He-filled 194 m long decay pipe, where a large fraction of the pions will decay via $\mu^{+} + \nu_{\mu}$ or $\mu^{-} + \bar{\nu}_{\mu}$, creating the neutrino beam. The decay pipe is immediately followed by the absorber, an assembly of aluminum, steel, and concrete. The absorber stops the protons that failed to interact in the target and the secondary particles that failed to decay to neutrinos. A longitudinal section of the LBNF beamline is shown in Fig. 2.2.

By adjusting the polarity of the horn's magnetic field, either positive or negative particles can be selected. This capability leads to two operational modes, known as Forward Horn Current (FHC) and Reverse Horn Current (RHC), which produce either a neutrino or antineutrino beam, respectively. This focusing structure is optimized to provide a wide band neutrino beam with an energy range between 0.5 and 5 GeV so as to cover the first and second neutrino oscillation maxima, which for a 1300 km baseline are approximately 2.4 and 0.8 GeV.

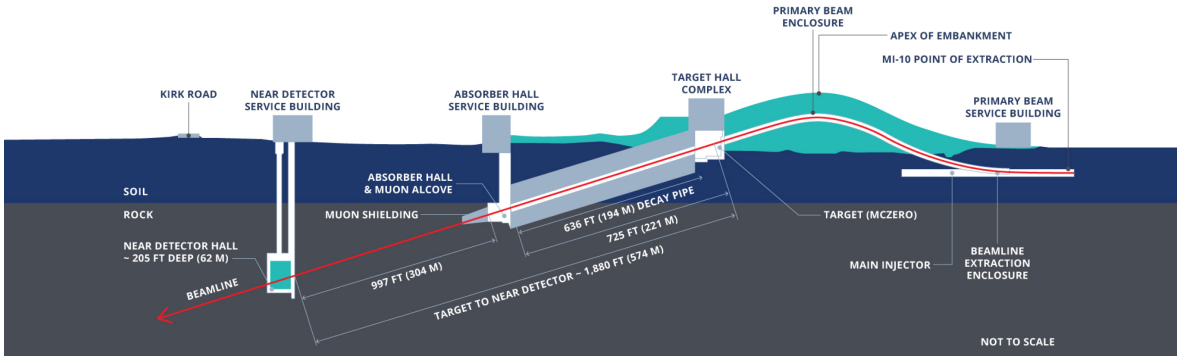

Fig. 2.2: *Longitudinal section of the LBNF beamline facility. The proton beam comes from the right, and the neutrino beam travels to the left* [43].

The DUNE neutrino beam consists of a 10 μs wide spill, with $\mathcal{O}(ns)$ bunch structure, delivered at a $\sim$ 1 Hz rate. The neutrino flux at the far detector site, in absence of oscillations and with all the possible neutrino flavors, is shown in Fig. 2.3 [44].

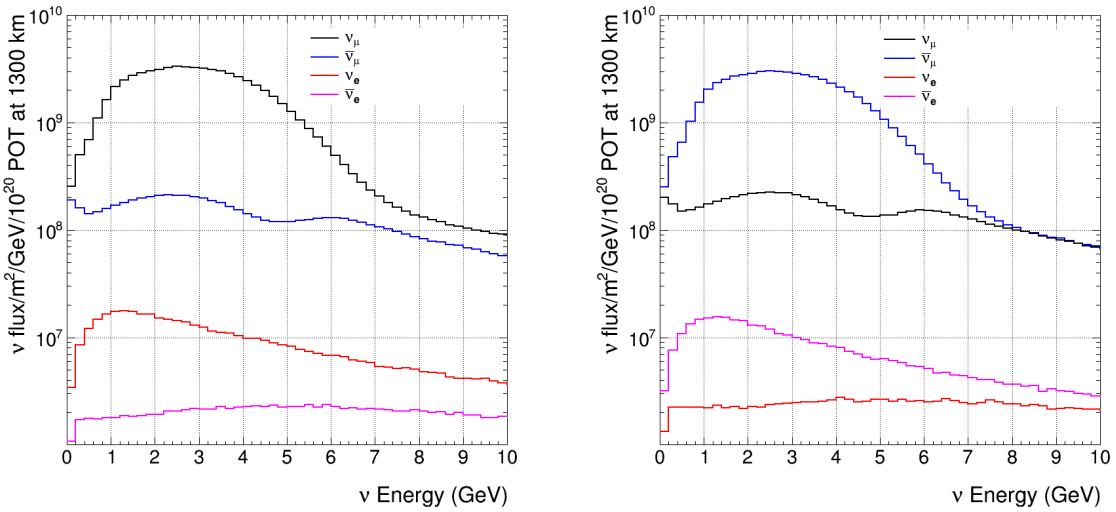

Fig. 2.3: *Neutrino Fluxes at the Far Detector as a function of energy in the absence of oscillations. On the left neutrinos and on the right antineutrinos. In addition to the dominant ν_μ flux, the minor components are also shown* [44].

2.2.2 Far Detector

The Far Detector is a modular liquid argon time-projection chamber (LArTPC). This detector combines a many-kiloton fiducial mass necessary for rare event searches with the ability to image those events with a millimeter-scale spatial resolution. This characteristic allows us to identify the signatures of the physics processes among the numerous backgrounds.

An additional strength of the detector lies in the excellent scintillation properties of liquid argon, which emits fast scintillation light at a wavelength of 126.8 nm (UV). The fast scintillation light, once shifted into the visible spectrum, is collected by photon detectors (PDs). These PDs will provide an initial start time (t_0) for every event recorded by the time projection chamber (TPC), indicating when the ionization electrons begin to drift. By comparing this start time with the time at which the ionization signal reaches the anode, the topology of the event can be reconstructed. In addition, the PDs will provide calorimetric information.

In Phase-I, FD will be composed of two modules (FD1-HD, FD2-VD), with two additional modules (FD3, FD4) to be added in Phase-II. Each detector module of 10 kt fiducial mass (17.5 kt total mass), will be installed about 1.5 km underground inside a cryostat with outer dimensions of 65.8 m (L) × 18.9 m (W) × 17.8 m (H).

The modules FD1-HD and FD2-VD are both single-phase LArTPC, but employ two different technologies: FD1-HD uses a traditional Horizontal Drift [45], while FD2-VD uses an innovative Vertical Drift [46]. The designs of FD3 and FD4 are still under development and will be deployed in Phase-II. A scheme of the FD is illustrated in Fig. 2.4.

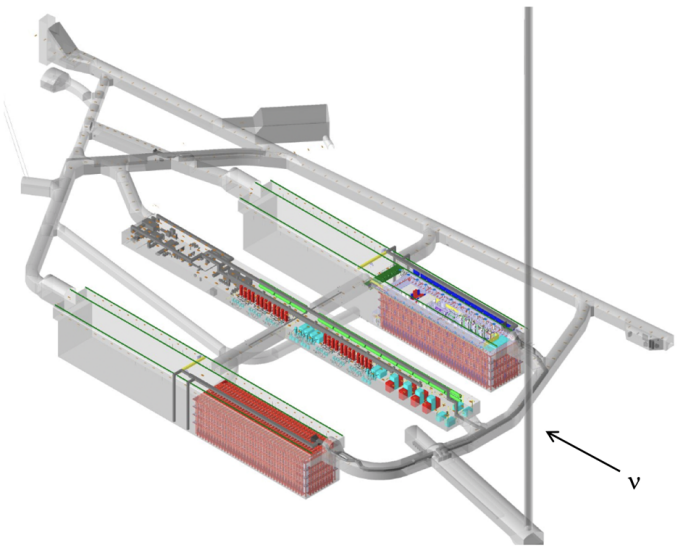

Fig. 2.4: *Underground caverns for the DUNE FD and cryogenics systems. The drawing shows the cryostats (red) for the first two FD modules* [42].

Horizonat Drift

The inner volume of the FD1-HD module, as shown in Fig. 2.5, is divided into four drift regions by alternating three anode walls and two cathode walls. Each drift region measures 58.2 m × 3.5 m × 12.0 m, and it is subjected to a strong E field of 500V/cm, corresponding to a cathode high voltage (HV) of -180kV. In this region, charged particles pass through the argon volume, ionizing its atoms. A typical minimum ionizing

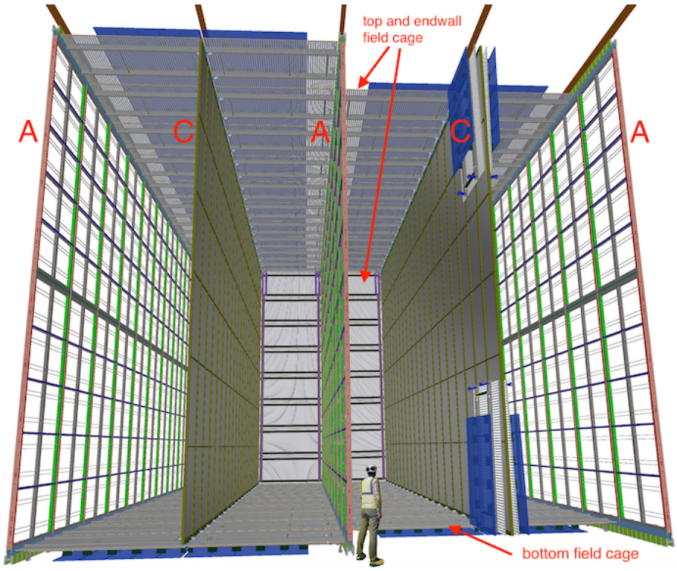

Fig. 2.5: *FD1-HD module, showing the alternating anode (A) and cathode (C) planes, as well as the field cage (FC) that surrounds the drift regions between the anode and cathode planes* [42].

particle produces around 60k ionization electrons per centimeter. The resulting ionization electrons then drift horizontally toward the anode wall at around 1.6 mm/μs, where they are read out. The time taken to drift the full distance from cathode to anode would be around 2.2 ms.

Each anode wall is composed of 50 anode plane assembly (APA) units of dimensions 6 m $\times$ 2.3 m. The APAs are two-sided and contain three active wire layers and an additional shielding layer, also called a grid layer, wrapped around them. The wire spacing on the layers is $\sim$ 5 mm. The relative voltage between the layers is chosen to ensure that all but the final layer are transparent to the drifting electrons. As electrons pass through the transparent layers (called U and V), they produce bipolar induction signals, whereas the final layer (X) collects the electrons, generating unipolar signals. The U and V layers are angled at $\pm 37.5°$ to allow a precise reconstruction. In Fig. 2.6 the general working principle of a single-phase LArTPC is illustrated. The pattern of current collected on the grid of anode wires provides information for reconstruction in the two coordinates perpendicular to the drift direction. The timing information for the events is provided by a photon detection system called X-ARAPUCA [47], placed behind each wire plane. This system employs a dichroic short-pass filter to shift the wavelength of scintillation photons from UV to visible, and trap them within a sealed optical cavity, where Silicon Photomultipliers (SiPMs) collect the light signals. The readout electronics, called cold electronic (CE), are attached to the top of the upper APA and to the bottom of the lower APA.

The cathode walls consist of many cathode plane assemblies (CPAs) arranged in a 2$\times$25 configuration. Each CPA is a 1.2 m $\times$ 4 m panel. The remaining open sides of the active volume are surrounded by a Field Cage, which ensures the electric field

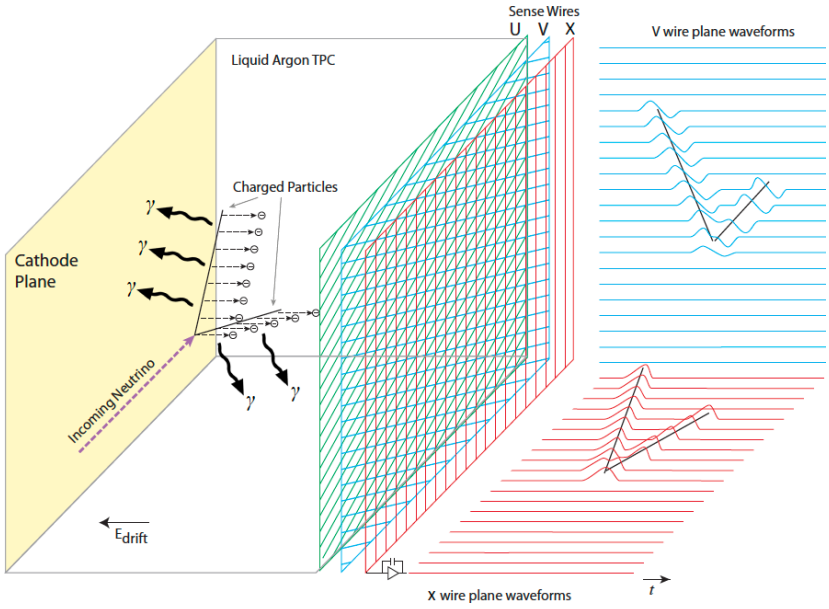

Fig. 2.6: *General working principle of a single-phase LAr TPC* [42].

inside the TPC remains uniform within a 1% tolerance.

Vertical Drift

The FD2-VD module will use a vertical drift. In this configuration the cathode is positioned horizontally at the midheight of the detector creating two drift volumes of equal drift distance 6.5 m and a nominal uniform E field of 450 V/cm. The module is surrounded by a field cage that ensures the uniformity of the electric field. This field causes the ionization electrons to drift vertically toward the anode planes located at the top and bottom of the detector. Each anode plane is composed of two double-sided perforated printed circuit boards (PCBs) of thickness 3.2 mm. These PCBs are mechanically connected, with their perforations aligned, to form charge-readout units (CRUs). CRUs are assembled into charge-readout planes (CRPs). Each anode plane consists of 80 CRPs. A scheme of FD2-VD module is illustrated in Fig. 2.7.

The first PCB, the one closer to the cathode, contains a copper guard plane to absorb any unexpected discharges, and an induction plane. The second PCB, includes a second induction plane and a collection plane. The three planes are set at 60° angles relative to each other to maximize information in the charge readout from different projections. A potential difference of about 1 kV must be applied across each PCB to guarantee full transmission of the electrons through the holes. The electrons pass through holes of the first PCB, then they reach the second one where they are collected.

The top and the bottom anodes will implement different charge readout (CRO) electronics, top drift electronics (TDE) and bottom drift electronics (BDE). The TDE, has both cold and warm components, while the BDE uses cold electronic.

Also in the vertical configuration, the scintillation light generated in liquid argon is detected by a photon detection system (PDS) based on X-ARAPUCA. These photode-

tectors are distributed across the four cryostat walls and on both faces of the central cathode, offering uniform optical coverage. The PDS performance will be enhanced by doping the LAr with a small amount of xenon.

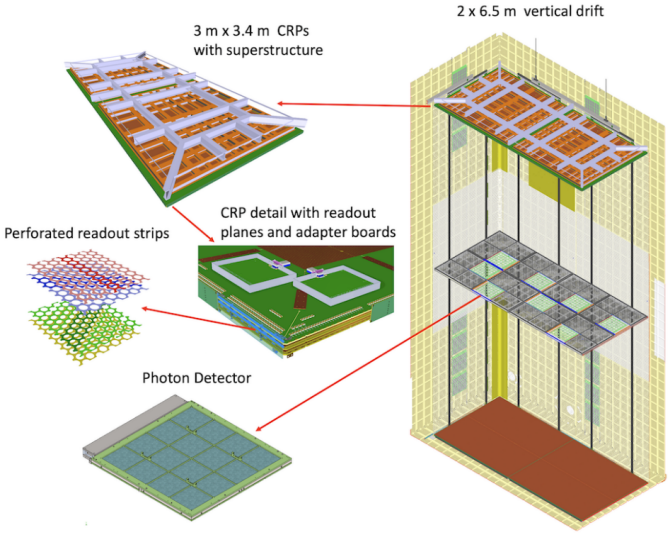

Fig. 2.7: *Scheme of vertical drift concept with PCB-based charge readout. PCB-based CRPs (brown, at top and bottom with superstructure in gray for top CRPs); cathode (violet); field cage modules (white); photon detectors, placed in the openings on the cathode and on the cryostat walls, around the perimeter in the vertical regions near the anode planes* [46].

2.2.3 Near Detector

The Near Detector (ND) will be located approximately 574 meters from the neutrino source at Fermilab and 60 m underground. It will consist of a suite of three sub-detectors, each with specific roles. In Phase-I, it will be composed of: ND-LAr, Temporary Muon Spectrometer (TMS) and the System of on-Axis Neutrino Detection (SAND). In Phase-II, TMS will be replaced by a more capable detector, the leading design for which consists in a high-pressure gaseous Argon TPC (ND-GAr).

ND-LAr and TMS/ND-GAr can move off beam axis, providing access to different neutrino energy spectra. The off-axis configuration yields an almost monochromatic neutrino flux (see Fig. 2.8).

These off-axis measurements will provide data sets with different beam spectra, allowing DUNE to deconvolve the beam and cross section models and constrain each separately. Moreover, these off-axis measurements allow for a data-driven determination of the relationship between true and reconstructed energy, which is less sensitive to neutrino interaction models. This physics program is referred to as DUNE Precision Reaction-Independent Spectrum Measurement (DUNE-PRISM). A scheme of the ND complex both on-axis and off-axis is illustrated in Fig. 2.9.

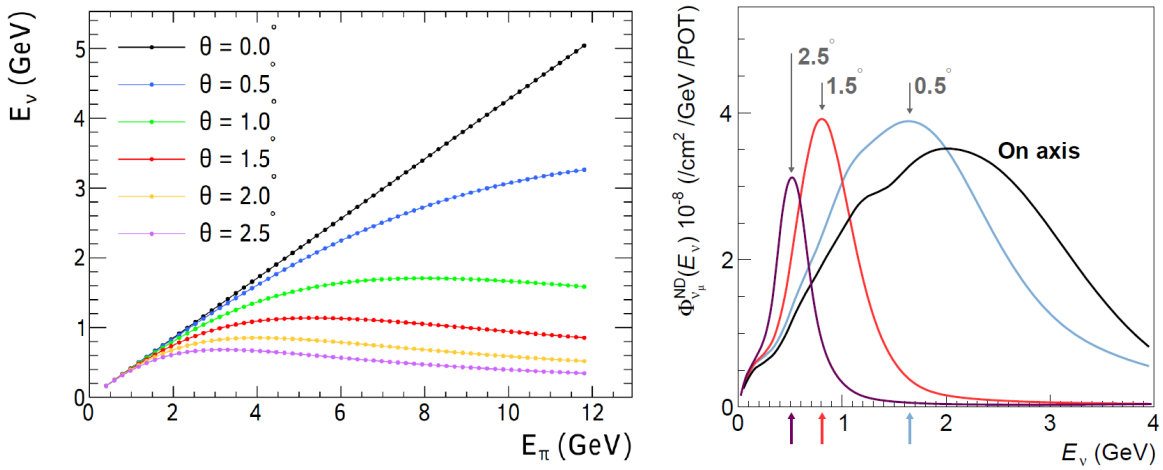

Fig. 2.8: *On the left, the neutrino energy as a function of pion energy for different observation angle. On the right, the predicted DUNE beam muon neutrino flux at the ND site as a function of off-axis angle. The arrows indicate the peak neutrino energy for three different off-axis angles* [48].

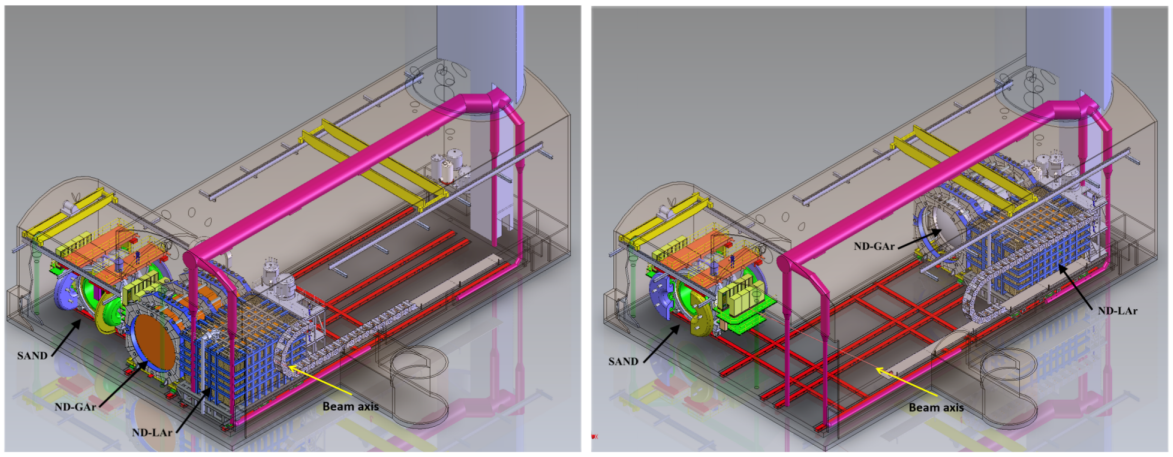

Fig. 2.9: *Scheme of the DUNE ND complex. On the left all detectors in the on-axis configuration. On the right ND-LAr and ND-GAr in an off-axis configuration. The beam axis and direction is indicated* [48].

ND-LAr

The ND-LAr is a liquid argon time projection chamber (LArTPC) designed to handle intense neutrino flux and the high event rate expected in the ND. This design consists of a large TPC made of 35 small, optically isolated TPC modules hosted in a common purified bath of liquid argon held in a cryostat. Each TPC features a high voltage cathode, a field cage that minimizes the amount of inactive material between modules, a light collection system, and a pixel-based charge readout. Each drift region has a maximum drift length of 50 cm.

The subdivision of the volume and optical isolation reduce the event overlap, and the pixelization of the readout allows for full 3D imaging with a spatial accuracy of about 16 mm and a time resolution of about 200 ns.

The scintillation light, which is detected in tandem with the ionization produced by charged particles, provides a complementary measurement of the signal position and energy, albeit at much lower granularity, but with substantially better timing resolution.

ND-LAr will have a total active volume of $5 \times 7 \times 3\ m^3$ and a fiducial mass of 67 tons, with the capability to detect approximately 10^8 ν_μ CC events annually. It will have the same target nucleus and uses the same fundamental detection principles as the FD. This will reduce sensitivity to nuclear effects and detector-driven systematic uncertainties in the extraction of the oscillation signal at the FD. In Fig. 2.10 is shown a scheme of ND-LAr. The large volume contains most of the hadron interactions, but its acceptance decreases for muons with momenta higher than 0.7 GeV/c due to lack of containment. To solve this problem, ND-LAr is complemented by the TMS/ND-GAr detector, to measure muon momentum and charge, critical quantities for accurate neutrino energy determination.

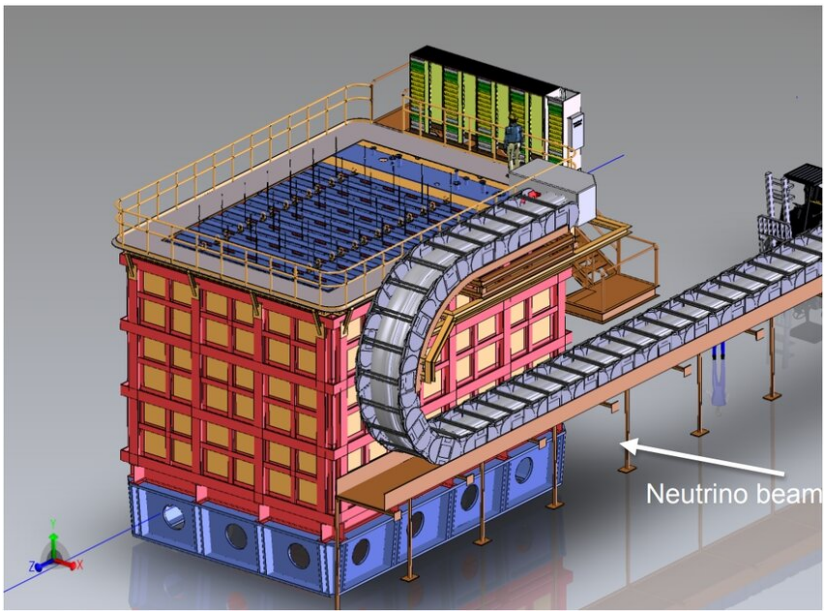

Fig. 2.10: *Schematic view of the external components of ND-LAr* [49].

TMS and ND-GAr

In Phase-I, muons that escape ND-LAr will be measured by the Temporary Muon Spectrometer (TMS) [50] shown in Fig.2.11. TMS is a magnetized range detector composed of 100 layers of dimensions 7.4 m × 5 m × m. Each layer consists of 192 scintillator slats, each 3.5 cm wide, read out using silicon photomultipliers (SiPMs). These scintillator planes are alternated with steel absorber plates 15 mm thick in the first 40 upstream layers and 40 mm thick in the remaining 60 downstream layers. TMS will operate within a 0.5 T magnetic field, and it will enable charge identification and momentum measurement of muons up to ~ 5 GeV, achieving a resolution of approximately 5%.

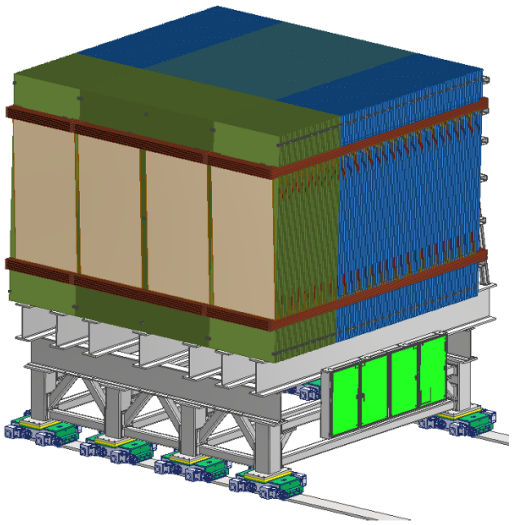

Fig. 2.11: *Schematic view of TMS showing the upstream 15 mm steel plates (green), the downstream 40 mm steel plates (blue), the scintillator modules (brown), and coils (orange)* [20].

In Phase II, TMS is expected to be replaced by ND-GAr (Fig. 2.12). The ND-GAr detector is a high pressure gaseous argon TPC (HPgTPC) surrounded by an electromagnetic calorimeter (ECAL) in a 0.5 T magnetic field. The high pressure gaseous argon TPC runs at 10 atmospheres and provides a lower-density medium with excellent tracking resolution to analyze muons from ND-LAr. This detector offers charge-sign determination, full momentum reconstruction, and particle identification in a single system. Moreover, it offers its own sample of neutrino interactions inside the HPgTPC.

Its 1 ton fiducial volume allows to collect approximately 1.6 $\times 10^6 \nu_\mu$ CC events annually in the on-axis configuration. Thanks to its gaseous argon target ($Ar - CH_4$ mixture), ND-GAr offers a lower energy threshold compared to liquid argon, improving access to low-momentum charged particles. The detector consists of a gaseous cylindrical chamber, a central high-voltage electrode that generates the drift field, and multi-wire proportional chambers (MWPCs) at the end-plates that enable signal amplification and readout. The parallel alignment of electric and magnetic fields minimizes

transverse diffusion, resulting in improved spatial resolution. The ND-GAr outside dimensions are approximately 12.8m wide (transverse to the neutrino beam) × 8.5 m deep (along the neutrino beam) × 10 m high.

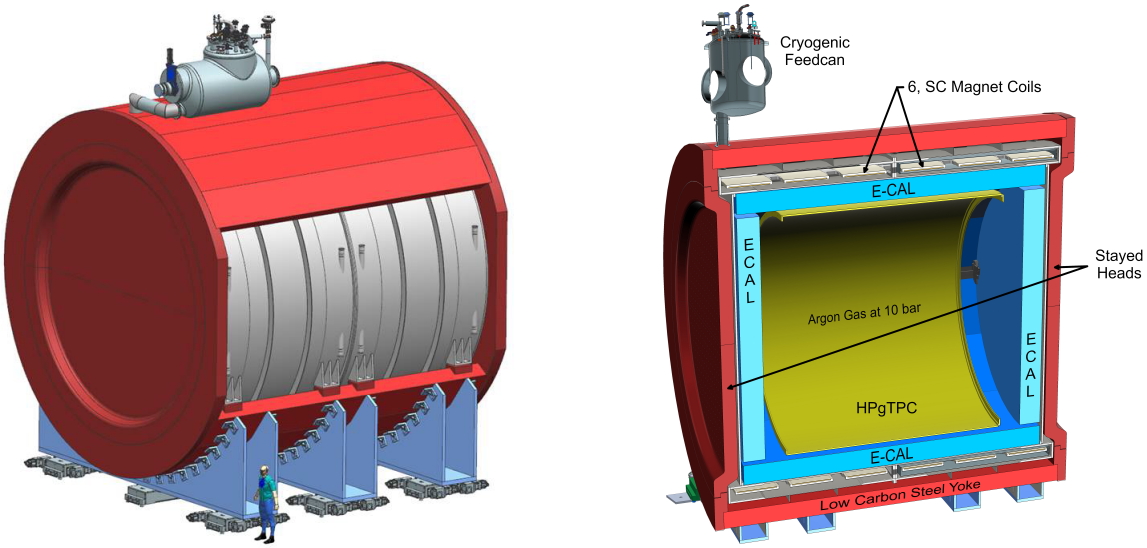

Fig. 2.12: *On the left a schematic representation of the outer layer of ND-GAr. On the right a tut-away view showing the various components* [51].

SAND

The System for on-Axis Neutrino Detection (SAND) is a multipurpose detector permanently positioned on-axis with respect to the neutrino beam to provide continuous monitoring of the neutrino flux directed at the FD. It consists of an inner tracker surrounded by an ECAL inside a large 0.6 T solenoidal magnet. The magnet and ECAL are components from the KLOE detector, previously located at the INFN Laboratory in Frascati. SAND integrates a compact liquid argon target called GRAIN ($\sim$ 1 ton) and a low-density tracker for precision tracking and calorimetry. This configuration enables effective reconstruction of low-energy neutrino interactions, especially those involving neutrons, which are often difficult to detect but critical for flux normalization and energy reconstruction.

The ECAL consists of a cylindrical structure with a central barrel (4 m diameter, 4.3 m active length, 23 cm thickness) and two end caps. The superconducting magnet ensures a uniform magnetic field within the tracking volume, optimized by a robust steel yoke and openable end plates for access. SAND's design, with materials and detection technologies different from ND-LAr and ND-GAr, introduces complementary systematics, improving model validation and our understanding of nuclear effects. The design and physics goals of SAND will be discussed in more detail in Chap. 3.

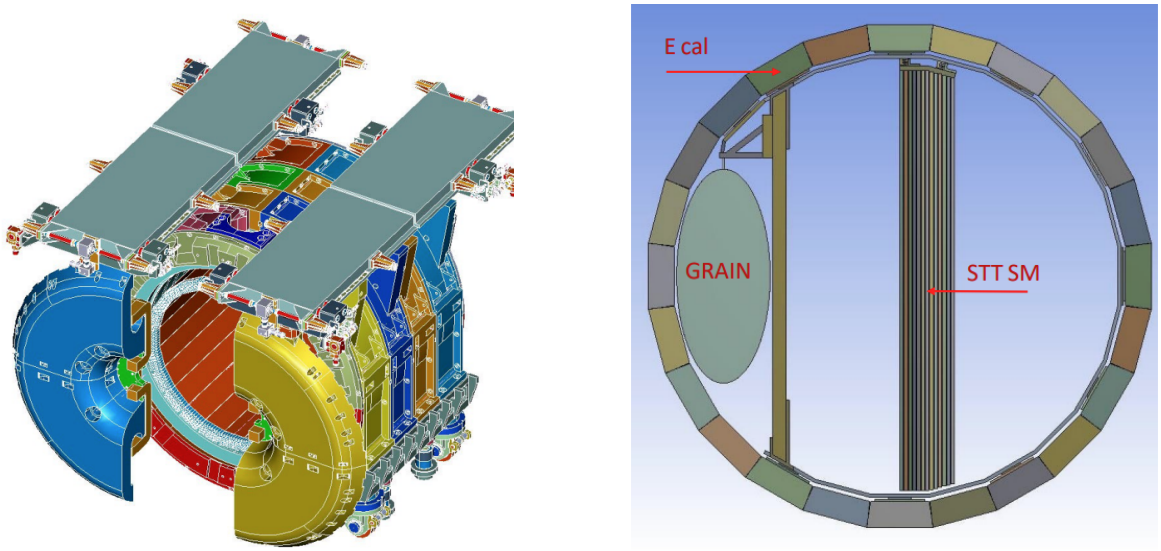

Fig. 2.13: *On the left a schematic representation of the external components of SAND. On the right a cut-away view of the internal components including GRAIN* [49].

2.3 Physics goals

To answer some of the most important neutrino open questions, the DUNE experiment will combine the world's most intense neutrino beam, a high resolution near detector, and a massive LArTPC far detectors. A key aim of the DUNE experiment is to measure neutrino interaction rates from which can be extracted the oscillation probabilities for muon (anti)neutrinos to either remain the same flavor or oscillate to electron (anti)neutrinos. Determining these probabilities as functions of the neutrino energy will allow precision measurements of the free parameters of the Pontecorvo-Maki-Nakagawa-Sakata (PMNS) matrix.

The ND located near the neutrino source will measure the unoscillated neutrino interaction rate, while the FD, located 1300 km away, will measure the neutrino interaction rate after oscillations. This baseline provides the matter effects necessary for DUNE to determine the neutrino mass hierarchy. A comparison of the measurements at the FD and ND allows for the extraction of oscillation probabilities.

DUNE includes a comprehensive program of neutrino oscillation measurements, the search for proton decay, and the detection and measurement of ν_e flux from a core-collapse supernova within the Milky Way. DUNE also includes other accelerator-based neutrino flavor transition measurements with sensitivity to physics beyond the standard model (BSM), measurements of neutrino oscillation phenomena using atmospheric neutrinos, searches for dark matter and a rich neutrino interaction physics program utilizing the ND.

2.3.1 Neutrino oscillation physics

Precision neutrino oscillation measurements lie at the heart of the DUNE scientific program. The strengths of DUNE are (i) its discovery potential for charge-parity symmetry violation (CPV) in the neutrino sector, (ii) its ability to resolve the neutrino mass ordering unambiguously, regardless of values of all other parameters governing neutrino oscillations, and (iii) its unique ability to make high precision measurements of neutrino oscillations all within a single experiment. DUNE will address these issues using ν_μ and $\bar{\nu}_\mu$ beams.

Given that the value of the mixing angle θ_{23} is almost maximal, the oscillations occur primary in the $\nu_\mu \to \nu_\tau$ channel. Since oscillation maxima are at energies below the threshold for τ-lepton production in ν_τ CC interactions in the detector, this channel is studied by measuring the ν_τ disappearance probability as a function of neutrino energy. On the other hand, the sub-dominant $\nu_\mu \to \nu_e$ channel can be used for a detailed study of several parameters of the PMNS matrix, by measuring the ν_e and $\bar{\nu}_e$ appearance probabilities.
The oscillation probability of $\nu_\mu \to \nu_e$, assuming a constant matter density, is:

$$\begin{aligned} P(\nu_\mu \to \nu_e) \simeq\ & \sin^2\theta_{23}\sin^2 2\theta_{13}\frac{\sin^2(\Delta_{31}-aL)}{(\Delta_{31}-aL)^2}\Delta_{31}^2 \\ & + \sin 2\theta_{23}\sin 2\theta_{13}\sin 2\theta_{12}\frac{\sin(\Delta_{31}-aL)}{\Delta_{31}-aL}\Delta_{31}\frac{\sin(aL)}{aL}\Delta_{21}\cos(\Delta_{31}+\delta_{\mathrm{CP}}) \\ & + \cos^2\theta_{23}\sin^2 2\theta_{12}\frac{\sin^2(aL)}{(aL)^2}\Delta_{21}^2, \end{aligned} \tag{2.1}$$

where $\Delta_{ij} = \Delta m^2_{ij} L/4E_\nu$, $a = G_F N_e/\sqrt{2}$, G_F is the Fermi constant, N_e is the number density of electrons in the Earth, L is the baseline in km, and E_ν is the neutrino energy in GeV. In Eq. 2.1, both δ_{CP} and a switch signs in going from the $\nu_\mu \to \nu_e$ to the $\bar{\nu}_\mu \to \bar{\nu}_e$ channel; this introduces a neutrino-antineutrino asymmetry due to both the CP violation (δ_{CP}) and the matter effect (a). From the same equation it is possible to note that this oscillation probability is sensitive to the sign of Δ_{13} , i.e. the mass hierarchy.

The electron neutrino appearance probability, $P(\nu_\mu \to \nu_e)$, is plotted in Fig. 2.14 as a function of neutrino energy for several values of δ_{CP}. As this figure illustrates, the value of δ_{CP} affects both the amplitude and phase of the oscillation. The difference in probability amplitude for different values of δ_{CP} is larger at higher oscillation nodes, which correspond to energies less than 1.5 GeV. Therefore, a broadband experiment capable of measuring both the rate of ν_e appearance and mapping the spectrum of observed oscillations down to energies of at least 500 MeV, is required to maximize the sensitivity of the experiment to CP violation [42]. Fig. 2.16 and Fig. 2.15 shows respectively the sensitivity to neutrino mass ordering and to CP violation. Both as a function of the true value of δ_{CP} and as a function of the exposure (i.e. kt-MW-years).

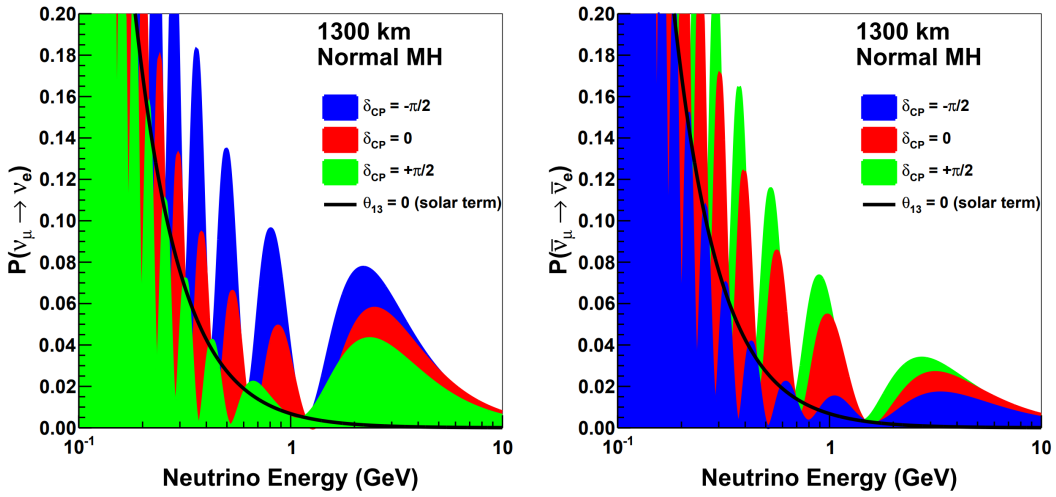

Fig. 2.14: *Appearance probability of ν_e and $\bar{\nu}_e$ at baseline of 1300 km as a function of neutrino energy for different values of δ_{CP} assuming a normal ordering* [42].

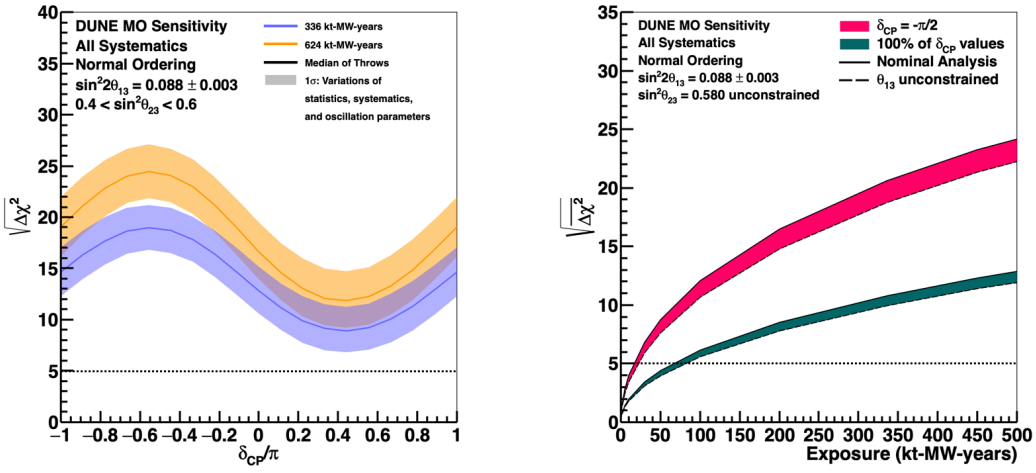

Fig. 2.15: *On the left, the sensitivity of the mass ordering as a function of the true value of δ_{CP} for a given exposure. On the right, the sensitivity as a function of exposure for a given δ_{CP} value or range of values* [52].

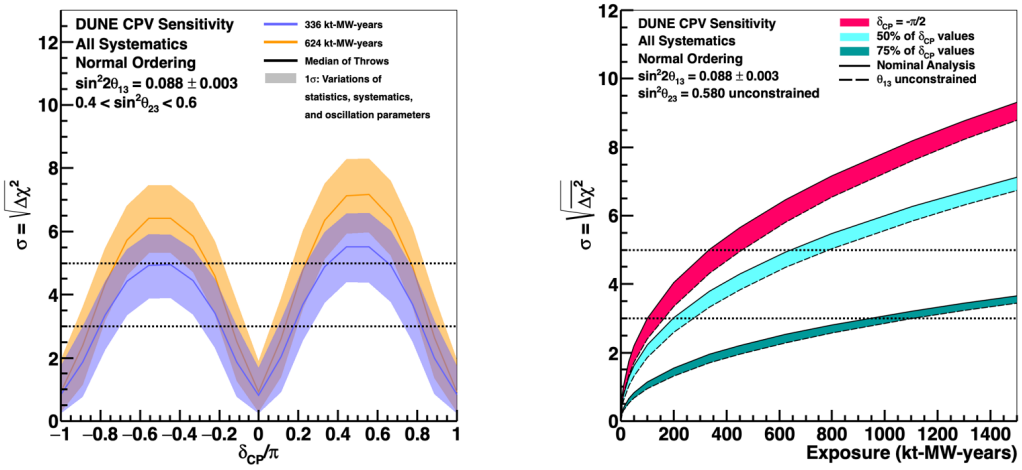

Fig. 2.16: *On the left, the sensitivity of the CP violation as a function of the true value of δ_{CP} for a given exposure. On the right, the sensitivity as a function of exposure for a given δ_{CP} value or range of values* [52].

DUNE will be able to establish the neutrino mass ordering at the 5σ level for 100% of δ_{CP} values with 100 kt-MW-years exposure. DUNE's capability to quickly and unambiguously determine the neutrino mass ordering is unique among existing and planned experiments.

DUNE can also observe CP violation with 3σ significance with 100 kt-MW-years exposure if $\delta_{CP} = -\frac{\pi}{2}$, which corresponds to maximal CP violation. CP violation can be observed with 5σ significance after $\sim$ 350 kt-MW-years if $\delta_{CP} = -\frac{\pi}{2}$ and after $\sim$ 700 kt-MW-years for 50% of the δ_{CP} values. CP violation can be observed with 3σ significance for 75% of the δ_{CP} values after $\sim$ 1000 kt-MW-years of exposure.

In Fig. 2.17, another DUNE's precision measurement capability is shown. At large exposures, DUNE is able to simultaneously determine both δ_{CP} and $\sin^2\theta_{13}$. DUNE will also perform precise measurements of $\sin^2\theta_{23}$ with a significant sensitivity to the θ_{23} octant for values of $\sin^2\theta_{23}$ less than about 0.47 and greater than about 0.55.

In the context of the oscillation program, the ND has many different goals. It will make a high-statistics characterization of the neutrino beam close to the source, to establish the null hypothesis, i.e. no oscillations, in the three-neutrino oscillation paradigm. The ND will precisely measure the energy spectra of unoscillated ν_μ and ν_e, as well as those of the antineutrinos, $\bar{\nu}_\mu$, $\bar{\nu}_e$. Comparing the measured neutrino energy spectra at the ND and FD allows us to disentangle the different energy-dependent effects that modulate the beam spectrum and to reduce the systematic uncertainties. The ND includes a powerful spectral beam monitor that can be used to detect changes in the beam in a timely fashion. The data are also useful for tuning the beam model and identifying the cause of changes in the beam. Thanks to the high statistics collected, the ND will be able to tune the neutrino interaction model used to move between the beam model and the observed data. This tuning is a powerful technique for reducing

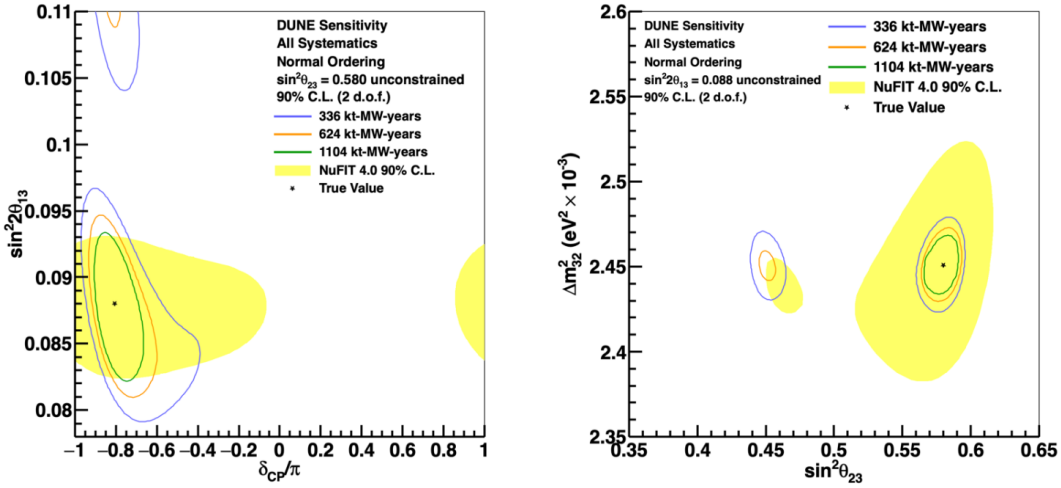

Fig. 2.17: *Two-dimensional 90% C.L. regions in the* $\sin^2\theta_{13}$–δ_{CP} *(left) and* $\sin^2\theta_{13}$–Δm^2_{32} *(right) plane, for three different levels of exposure, with equal running in neutrino and antineutrino mode. The 90% C.L. region for the NuFIT global fit is shown in yellow for comparison* [52].

systematic errors in the extracted oscillation parameters.

2.3.2 Nucleon decay and Baryon number violation

The apparent stability of protons suggests that the baryon number is conserved in nature, although no known symmetry requires it to be so. Indeed, the baryon number conservation is not explicit in the formulation of the SM Lagrangian, and thus observation of baryon-number violating (BNV) processes such as nucleon decay or neutron-antineutron oscillation would be evidence for physics beyond the Standard Model.

DUNE, thanks to its large underground liquid argon time-projection chambers (LArTPC), is uniquely suited to search for BNV processes. In fact, the LArTPC with its excellent imaging, calorimetric and particle identification capabilities should be able to reduce the background below the single-event level in key nucleon decay channels.

A particularly promising discovery channel is the proton decay into a kaon and a neutrino ($p \to K^+\nu$). In this channel, the kaon and its decay products can be reconstructed with high precision. Based on current analysis, DUNE could set a lower limit on the proton lifetime of 1.3×10^{34} years (90% *C.L.*) after a 400 kt · year exposure, doubling the current limit from Super–Kamiokande [53]. If the actual decay rate is near this limit, DUNE could observe up to five candidate events in ten years.

Another potential mode for a baryon number violation search is the decay of the neutron into a charged lepton plus meson, $n \to e^- K^+$. The lifetime sensitivity for a 400 kt-yr exposure is estimated to be 1.1×10^{34} years. Moreover, neutron-antineutron ($n \to \bar{n}$) oscillation is a $|B| = 2$ process. This type of baryon number violation has

never been observed. The expected limit for the oscillation time of free neutrons for a 400 kt-yr DUNE exposure is calculated to be 5.5×10^8 seconds [52].

2.3.3 Supernova neutrinos

A Core-collapse supernova (SN) in the Milky Way is expected during the lifetime of DUNE, so it is important that at least one module of the FD be online at all times to observe this unpredictable event, if and when it occurs. The core-collapse neutrino signal starts with a short, sharp neutronization burst primarily composed of ν_e. These neutrinos are emitted as the shock wave breaks through the neutrino sphere. This quick and intense burst is followed by an "accretion" phase lasting some hundreds of milliseconds, depending on the progenitor star mass, where matter falls onto the collapsed core powering the neutrino luminosity. The later "cooling" phase over ~ 10 seconds represents the main part of the signal, over which the proto-neutron star sheds its trapped thermal energy via neutrino emission.
For these reasons, from the neutrino spectrum as a function of time, information about the progenitor, the collapse, the explosion, and the remnant can be inferred, as well as information about neutrino parameters and potentially exotic new physics.
The DUNE FD will be particularly sensitive to supernova neutrinos with energies from tens of MeVs to 5 MeV. More in detail, to the ν_e flux via CC interaction with argon nuclei: $\nu_e + {}^{40}Ar \rightarrow e^- + {}^{40}K^*$.

2.3.4 Atmospheric neutrinos

Atmospheric neutrinos are another tool for studying neutrino oscillations. Their oscillated flux contains all flavors of neutrinos and antineutrinos, is very sensitive to matter effects and to both Δm^2 parameters, and covers a wide range of L/E. As a result, they can be used to measure oscillation parameters, with high complementarity to neutrino beam measurements. In addition, atmospheric neutrinos are available at all times.

The DUNE FD, with its large mass and the overburden to protect it from atmospheric muon background, is an ideal tool for atmospheric neutrino studies. Since the event topology and energy scale overlap with beam neutrino interactions, the only additional requirements for the FD design include a self-trigger , which is needed due to the fact that, which is needed due to the fact that atmospheric neutrino events are asynchronous with accelerator timing.

Atmospheric neutrinos are particularly suited to determine the neutrino mass ordering. When neutrinos travel through the Earth, the MSW effect enhances electron neutrino oscillations in the few-GeV energy range affecting ν_e in the case of normal mass ordering and $\bar{\nu}_e$ in the inverted ordering. DUNE FD, with its high-resolution imaging, offers the possibility to provide statistical discrimination between neutrinos and antineutrinos, using a proton tag and a decay electron tag.

The atmospheric data can also be used to probe both ν_μ disappearance and ν_e appearance, with the sensitivity strongly depending on the true value of $\sin^2\theta_{23}$. DUNE's

atmospheric measurements can thus help resolve the θ_{23} octant degeneracy.

2.3.5 Beyond standard model physics

The unique combination of the high-intensity neutrino beam with DUNE's ND and massive LArTPC FD modules at a 1300 km baseline enables a variety of probes of BSM physics listed below.

Sterile neutrino mixing

As mentioned in Chap. 1, some theories would require the existence of sterile neutrinos and, at the same time, experimental results in tension with the three-neutrino-flavor paradigm, have generated interest for searches of sterile neutrinos. DUNE will be sensitive over a broad range of potential sterile neutrino mass splittings by looking for disappearance of CC and NC interactions over the long distance separating the ND and FD, as well as over the short baseline of the ND. Moreover, a deviation from the unitarity of the 3×3 PMNS matrix due to extra heavy neutrino states may be observed.

Non-standard interactions (NSIs)

NSIs affecting neutrino propagation through the Earth can significantly modify the data to be collected by DUNE as long as the new physics parameters are large enough. If the DUNE data are consistent with standard oscillations for three massive neutrinos, interaction effects of order 0.1 G_F can be ruled out at DUNE.

Neutrino trident production

Neutrino trident production is a rare weak process in which a neutrino, scattering off the Coulomb field of a heavy nucleus, generates a pair of charged leptons. The typical final state of a neutrino trident interaction contains two leptons of opposite charge. DUNE, with its high statistics provided by the high intensity of ν_μ flux at the ND, will be able to produce this kind of events and to look for an excess of events above the Standard Model prediction, which would indicate new physics.

CPT symmentry

CPT symmetry-the combined invariance under charge conjugation, parity transformation, and time reversal—constitutes a fundamental principle in constructing theoretical models. Consequently, any evidence of its violation would pose a profound challenge to the Standard Model of particle physics. DUNE has the potential to improve the present limits on Lorentz and CPT violation by several orders of magnitude, contributing significantly to the testing of these fundamental conservation rules.

Dark matter

DUNE offers unique capabilities to explore dark matter scenarios, including both light dark matter (LDM) and boosted dark matter (BDM). The lack of evidence of weakly interacting massive particle (WIMP) from direct detection at collider experiments has generated interest in alternative models, such as sub-GeV LDM that interacts with Standard Model particles via a light mediator through the so-called vector portal. DUNE, with its high-flux neutrino beam and precise near detector could enable sensitive searches for LDM through NC interactions with electrons or nucleons. At the same time, the large mass and the deep underground location of the FD, will enable searches for BDM i.e. relativistic dark matter particles generally produced from the annihilation of heavier components anywhere in the cosmos.

Chapter 3

The SAND detector

3.1 Introduction

DUNE's main scientific goal is to infer the neutrino oscillation probability P_{osc}, and to provide an estimate of all its governing parameters in a single accelerator experiment. To achieve this goal it will measure the number of events N_X, as a function of the reconstructed neutrino energy, for a given process X in both the Near and Far detectors. The number of events can be written as:

$$N_X(E_{rec}) = \int_{E_\nu} dE_\nu \; \Phi(E_\nu) \; P_{osc}(E_\nu) \; \sigma_X(E_\nu) R_{phys} \; (E_\nu, E_{vis}) \; R_{det}(E_{vis}, E_{rec}) \quad (3.1)$$

where Φ is the incoming (anti)neutrino flux, σ_X is the cross-section for the process X on a given nuclear target, R_{phys} is the nuclear smearing function that models how primary particles from neutrino interactions interact with nucleons before leaving the nucleus, and R_{det} is the detector acceptance. E_ν is the true neutrino energy, E_{vis} is the total energy of the visible final-state particles emerging from the nuclear smearing and E_{rec} is the final reconstructed energy in the detector. Since the terms in Eq. 3.1 are folded together into the observed event distribution, and since each of them has its own associated systematic uncertainty, the measurement of the number of events is not trivial. The key role of the ND will be to measure and systematics constraint all these terms individually, using different detectors and nuclear targets. DUNE, for its analysis, requires the combined systematic uncertainties to be smaller than the corresponding statistical uncertainties. This is crucial since even a small change in relative uncertainties from 1% to 3% can substantially increase the total exposure needed to achieve a discovery (5σ) [54].

The System for on-Axis Neutrino Detection (SAND) is a multipurpose detector permanently positioned on-axis with respect to the neutrino beam to provide continuous monitoring of the neutrino flux directed at the FD.
In this chapter, SAND's design and its physics goals are presented.

3.2 Design

SAND is composed of an Electromagnetic Calorimeter (ECAL), a low density tracker and a small active liquid argon target called GRAIN. All these components are embedded into a magnetic field (0.6 T) generated by a superconducting solenoid. Both the magnet and the ECAL are reused components of the K-Long Experiment (KLOE), designed primarily for the study of CP violation in neutral kaon decays at the DAΦNE Φ-factory at INFN-LNF [55].

3.2.1 Magnet

SAND's super-conducting magnet, designed in tandem with a 475-ton iron yoke, provides a magnetic field of 0.6 T in a cylindrical volume 4.3 meters long and 4.8 meters in diameter. The coil operates at a nominal current of 2902 A and stores 14.32 MJ of energy. This coil consists of a two-layer conductor layer wound flat with a full vacuum impregnated insulation system. The conductor is a composite made of a (Nb-Ti) Rutherford cable co-extruded with high purity aluminum. The conductor is wrapped with two half-lapped layers of glass tape. The coil is contained in a cryostat with an outer diameter of 5.76 m, an inner diameter of 4.86 m and an overall length of 4.40 m. The cooling of the coil is done via thermo-siphoning cycles: Helium gas at 5.2 K is injected at 3 bar from the cryogenic plant and liquefied through Joule-Thomson valves into a liquid He bath in thermal contact with the coil. Current leads are directly cooled by liquid He, whereas the radiation shields are cooled by gas He at 70 K from the cryogenic plan [56].

3.2.2 Electromagnetic calorimeter

The electromagnetic calorimeter (ECAL), illustrated in Fig. 3.1, is a lead-scintillating fiber sampling calorimeter. Scintillating fibers provide efficient light transmission over several meters, offer sub-nanosecond time resolution, and very good hermeticity.

The calorimeter is composed of: a barrel calorimeter, of a nearly-cylindrical shape, located inside the magnet close to the coil cryostat; and two additional calorimeters, called end-caps, positioned at the ends of the magnet to ensure hermeticity. The barrel is composed of 24 modules, each measuring 4.3 m in length, 23 cm in thickness, and having a trapezoidal cross-section with base widths of 52 and 59 cm. The end-caps are made of 32 vertical rectangular modules that are 23 cm thick and vary in length from 0.7 to 3.9 m long. These modules are bent at the upper and lower ends to allow insertion into the barrel calorimeter and also to place the phototube axes parallel to the magnetic field. Thanks to the large overlap between the barrel and the end-caps, the calorimeter achieves full coverage because it does not have an inactive gap at the interface between those components. Each ECAL module is a layered structure composed of approximately 200 grooved lead foils of 0.5 mm thickness, alternated with 200 layers of 1 mm diameter cladded scintillating fibers glued together with an epoxy.

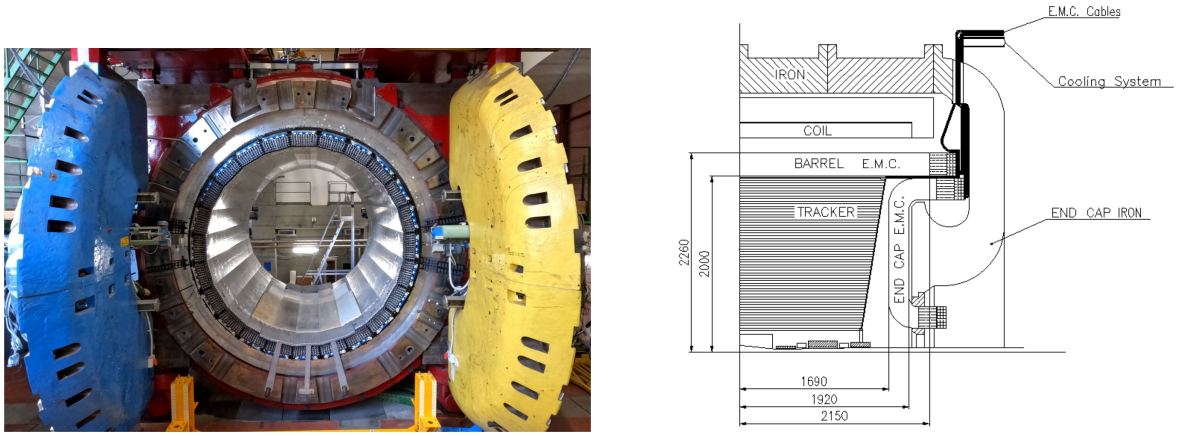

Fig. 3.1: *On the left, a view of the magnet, yoke and barrel ECAL modules of KLOE* [57]. On the right, a scheme of the vertical cross section of the magnet, yoke and barrel ECAL [54].

The ECAL has an average density of 5 g/cm^3, a radiation length of $\sim$ 1.5 cm, an overall thickness of $\sim$ 15 radiation lengths, and a mass of $\sim$ 100 t. The readout system includes 4880 phototubes.

The light of each module is collected from both ends by using light guides. The read-out divides the calorimeter into five layers in depth: the first four layers are 4.4 cm deep, the last one is 5.2 cm deep. These layers are also divided along the transverse direction into elements 4.4 cm wide. This readout segmentation provides a spatial resolution of 1.3 cm in $r - \Phi$ coordinates for the barrel, and in $x - z$ coordinates for the end-caps. The energy and time resolutions were evaluated in the running phases of KLOE [58], they are:

$$\frac{\sigma_E}{E} = \frac{5\%}{\sqrt{E\ (\mathrm{GeV})}}, \qquad \sigma_t = \frac{54\ \mathrm{ps}}{\sqrt{E\ (\mathrm{GeV})}}.$$

3.2.3 Tracker

The tracker, which occupies most of the volume inside the ECAL, has two primary goals: to offer a target for (anti)neutrino interactions and to provide a tracking system able to accurately reconstruct the momenta of all charged particles. To achieve these goals, a series of key physics-driven requirement were identified in the design stage. SAND should have a low density and high track sampling to minimize multiple scattering and so guarantee high resolution in momentum and space. Its total thickness should be comparable with the radiation length to minimize secondary interactions. Moreover, it should be able to accommodate various target materials to compare neutrino interactions on different nuclear targets within the same detector. The tracker should also be capable of performing particle identification for $e^{\pm}$, $\pi^{\pm}$, $K^{\pm}$, p, $\mu^{\pm}$. Finally, it should have a fiducial target mass of $\sim$5 tons to guarantee a sufficient interaction rate. Based on these characteristics, two possible designs are being developed:

a nominal Straw Tube Tracker (STT) and a Drift Chamber Tracker.

Straw Tube Tracker

SAND's STT follows a modular design. One module, shown in Fig. 3.2, is equipped with:

- a passive target layer of carbon or polypropylene with thickness of 4 mm or 5 mm respectively;
- a radiator made of 105 polypropylene foils 18 μm thick, alternating with 117 μm air gaps for e/π separation via transition radiation;
- four straw layers, where each straws has a 3.2 length, 5 mm diameter, 12 μm Mylar walls coated with Al and 20 μm tungsten wire coated with Au; and it operates with a gaseous mixture of Xe and CO_2 (70/30) at 1.9 atm. Two straw layers are placed along the X-axis and the others two along the Y-axis in an XXYY configuration.

The target and radiator layers are the main targets in the detector. Many different materials such as C, Ca, Fe, Pb, can be installed in place of the target slabs.

The average density of the detector can be tuned between a maximum of 0.18 g/cm^3, corresponding to the thickness of the radiator and the target, and a minimum of 0.005 g/cm^3 if only the straw layers are present. This density is kept low enough to obtain a total detector length comparable to one radiation length, for an accurate measurement of the four-momenta of the final-state particles. The passive targets account for up to 97% of the total detector mass, the remaining 3% accounts for the mass of the straws. The STT provides: a single hit space resolution smaller than 200 μm, a momentum resolution $\sim$ 3% and an angular resolution of 2 mrad.

The tracker configuration used in the analysis presented in Chap. 4 consists of 85 modules equipped with about 4.7 tons of C_3H_6 (78 modules) and 504 kg of graphite (7 modules) targets. At the moment, the collaboration is also considering another STT design with a smaller number of modules, which is under study.

Drift Chamber Tracker

The drift chamber design, much like STT, has a modular structure. In this case, each module is equipped with the following components:

- a passive target layer of carbon or polypropylene with thickness of 4 mm or 5 mm respectively;
- three planes of wires, called stations, with a thickness of 1 cm, separated by 20 μm thick Mylar planes. The stations contain alternated signal and field wires

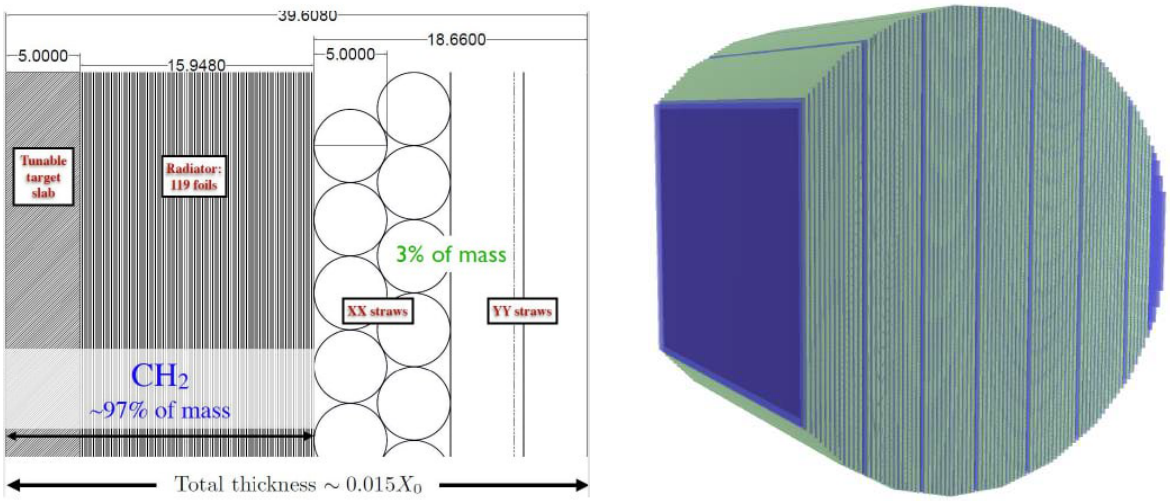

Fig. 3.2: *On the left, a schematic draw of an STT module: from left to right, the target layer, radiator, and four straw layers (XXYY) are shown [48]. On the right, the complete geometry of the STT with its modules: the blue modules are the ones equipped with graphite targets while the gray ones are the modules with polypropylene target [54].*

spaced 1 cm apart and are filled with a gaseous mixture of Ar and CO_2 (85/15) at 1 atm and with a density of 0.002 g/cm^3.

These modules are assembled in larger carbon frames, called supermodules, composed of 1 module with a carbon target and 9 modules with a polypropylene target. The supermodules are 35 cm thick and 3.2 m long and have positions-dependent heights from 1.3 m to 3.8 m. In the current design, the drift chamber tracker is composed of 8 supermodules [59].

3.2.4 GRAIN

The Granular Argon for Interaction of Neutrinos (GRAIN) is an active liquid Argon target with a fiducial mass of $\sim$ 1 ton, that will be placed in the upstream section of the SAND inner volume. The main goal of this detector element is to constrain nuclear effects on argon and to have a complementary argon target always located on-axis, with respect to the neutrino beam, for cross-calibration with other detectors.

GRAIN, as shown in Fig. 3.4, consists of two coaxial cylindrical cryostats: an inner vessel and an outer vessel. The outer vessel is made of different layers of aluminum alloy, honeycomb, and carbon fiber. It is 190 cm high, 200 cm wide and with a maximum thickness of 83 cm. The inner vessel is made of stainless steal and is 147 cm high, 150 cm wide and with a maximum depth of 47 cm. Inside, the liquid argon will be kept at 1.5 bar pressure. A vacuum will be maintained between the two vessels at a pressure of $10^{-4} - 10^{-5}$ bar to thermally insulate the inner vessel. GRAIN relies on the imaging

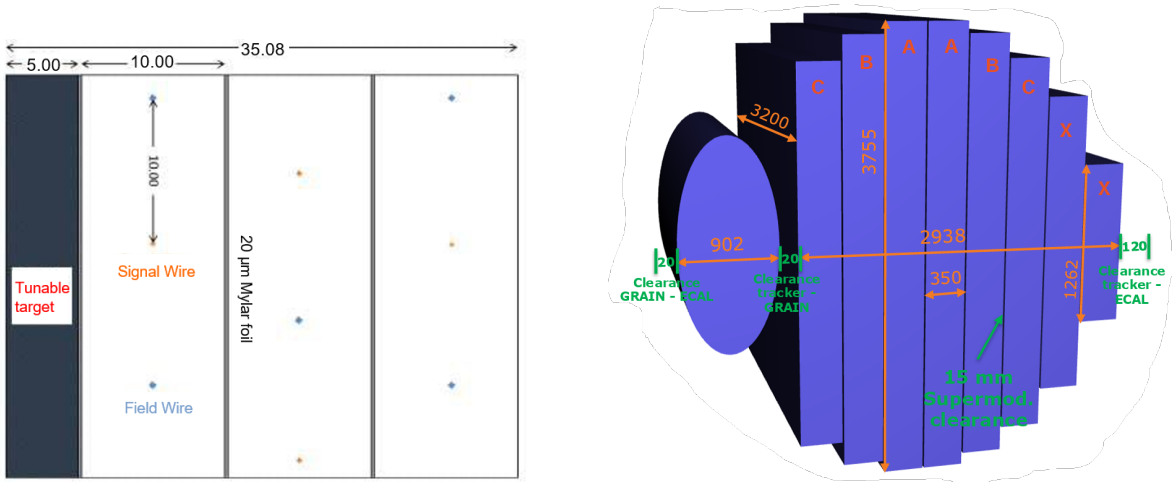

Fig. 3.3: *On the left, a schematic draw of a drift module: from left to right, the target layer, and three drift stations are shown. On the right, the complete geometry of the drift chamber tracker with its supermodules, and GRAIN [59].*

of scintillation light emitted by charged particles, for this reason, the inner vessel will be provided of Vacuum UltraViolet cameras to collect the scintillation light from argon [60].

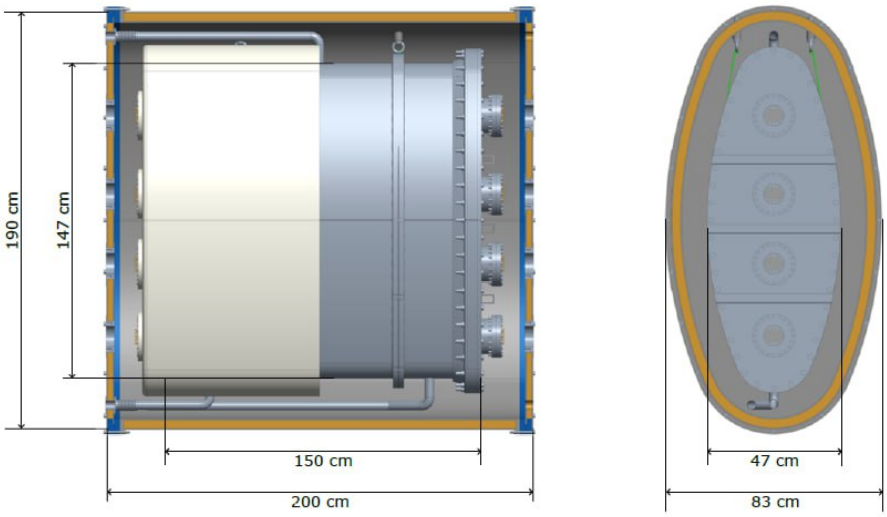

Fig. 3.4: *Scheme of GRAIN inner structure* [61].

3.3 Physics goals

SAND features an oscillation physics program complementary to that of FD, as well as an independent physics program. In the context of neutrino oscillation physics it will monitor the neutrino beam on-axis, its time variations, and it will constrain the nuclear smearing and the systematics on the neutrino flux. SAND's independent physics program involves different goals such as the electroweak precision measurements, studies of (anti)neutrino-nucleus interactions, tests of the isospin and sum rules, measurements of the strangeness content of the nucleon and QCD studies and also measurements of physics beyond the Standard Model [54].

3.3.1 Constraining Systematic Uncertainties

Each term in Eq. 3.1, as already mentioned, has its own statistical uncertainty that must be constrained to perform accurate measurements. Let us consider each factor:

- $\Phi(E_\nu)$: the flux can be accurately measured using a low density tracker, able to achieve high resolution, and a light A target able to minimize the impact of nuclear effects.
- $\sigma_X(E_\nu)$: the cross-section measurements require the same Ar target as the FD. Once all the flux is precisely measured, the cross-section on Ar ca be measured. It is important to note that an accurate measurement of the cross-section is particularly challenging since in the DUNE energy range ($0.5 < E_\nu < 10$ GeV), the neutrino interactions receive a contribution from all the processes: QE ($\sim 25\%$), RES ($\sim 42\%$), DIS ($\sim 33\%$).
- R_{phys} (E_ν, E_{vis}): to disentangle the physics response function from the detector acceptance, both Ar and lighter targets are required in the same detector. SAND will constrain the physics response function using the hydrogen target, for which $R_{phys} \equiv 1$, in combination with Ar and polypropylene.
- $R_{det}(E_{vis}, E_{rec})$: the detector response for the FD can only be provided by detectors with a liquid argon target in the ND complex. Since SAND has different nuclear targets, the determination of $\sigma_X R_{phys}$ would allow an "easy" unfolding of R_{det} in Ar.

Flux Measurements

A precise knowledge of the neutrino flux is crucial for all the DUNE measurements and it is necessary to unfold the terms in Eq. 3.1. SAND will provide an accurate determination of the absolute and relative fluxes using different processes:

- absolute ν_μ flux, from $\nu e \to \nu e$ elastic scattering;
- relative ν_μ flux, from $\nu p \to \mu^- p \pi^+$ on H with energy transfer $\nu < 0.5$ GeV;
- absolute $\bar{\nu}_\mu$ flux, from $\bar{\nu} p \to \mu^+ n$ quasi elastic scattering on H with $Q^2 \leq 0.05$ GeV^2;
- relative $\bar{\nu}_\mu$ flux, from $\bar{\nu} p \to \mu^+ n$ quasi elastic scattering on H with small energy transfer $\nu < 0.25$ GeV;
- ratio of $\bar{\nu}_\mu/\nu_\mu$ fluxes, from coherent interactions π^-/π^+ on C;

- ratio of ν_e/ν_μ and $\bar{\nu}_e/\bar{\nu}_\mu$ fluxes, from ν and $\bar{\nu}$ CC interactions on CH_2 and on H;

- Determination of parent $\mu/\pi/K$ distributions from ν and $\bar{\nu}$ CC interactions on H and CH_2 at low-ν.

Constraints on the Nuclear Smearing

The uncertainties on the nuclear smearing function R_{phys}, are mainly due to the limitation of the models describing the nucleon momentum distribution inside the nucleus and the final state interactions. SAND, will be able to reduce these systematic uncertainties thanks to its tracking system structure. SAND will fix R_{det}, thanks to its target made of different materials, which provides neutrino interactions on hydrogen, carbon and argon with the same detector response, so with the same R_{det}, allowing to unfold the product $\sigma_X R_{phis}$.
Moreover, as described in Sec. 3.2.3, SAND will be equipped with a large amount of hydrogen target for which the neutrino cross-section have small uncertainties and no final state interactions are involved. For these reasons, for interactions on hydrogen, it results $R_{phys} = 1$. This allows a precise measurement of the neutrino cross-section on H and of the neutrino energy E_ν. The latter one, depends only on R_{det} so its resolution depends only on $\delta p/p$.
A comparison between interactions on hydrogen and on argon allows to determine $R_{phys}(\mathrm{Ar})$ and so to determine the modification of the cross-sections in argon due to nuclear effects. These results can be used to tune nuclear models.
Additional constraints on R_{phys} can be obtained by considering a set of kinematic variables sensitive to the effect of the nuclear smearing and comparing the observed distributions of these variables from events in Ar and H targets. This measurement strategy can constrain the nuclear smearing for the ND beam spectrum.

3.3.2 Electroweak Precision measurements

SAND will perform a precise determination of the weak mixing angle $\sin^2\theta_W$, which will provide a direct measurement of neutrino couplings to the Z boson. It will determine the mixing angle from the ratio of NC and CC DIS interactions, $\mathcal{R}^\nu \equiv \sigma^\nu_{NC}/\sigma^\nu_{CC}$, induced by neutrinos. The precision on this measure will depend on theoretical systematic uncertainties on the structure functions of the target nucleons, that must be reduced as much as possible.

A second independent measurement of the weak mixing angle can be obtained from NC $\nu_\mu e$ elastic scattering, considering the ratio $\mathcal{R}_{\nu e}(Q^2) \equiv \sigma(\bar{\nu}_\mu e \to \bar{\nu}_\mu e)/\sigma(\nu_\mu e \to \nu_\mu e)$, in which systematic uncertainties related to the selection and the electron identification cancel out. This channel is free from hadronic uncertainties but it is limited in statistics due to its tiny cross section. The available statistic can be increased by a combined analysis of the events collected by the ND-LAr detector.

Some other channels that SAND will use to measure the weak mixing angle could also be the NC elastic scattering off protons and the coherent ρ production.

3.3.3 Test of the Isospin Physics and Sum Rules

The large sample of neutrino and antineutrino interactions on H, provided by SAND, enables a precision test of the Adler sum rule:

$$S_A = 0.5 \int_0^1 \frac{dx}{x}(F_2^{\bar{\nu}p} - F_2^{\nu p}) = I_p, \tag{3.2}$$

where I_p is the isospin of the target, $F_2 = x(\frac{4}{9}u(x)+\frac{1}{9}d(x))$ is the structure function with $u(x)$ and $d(x)$ parton distribution functions and x is the Bjorken x. This measurement is sensitive to possible violations of the isospin (charge) symmetry, heavy quark (charm) production, and strange sea asymmetries $s-\bar{s}$. Furthermore, the measurement from H can be compared with the values of S_A obtained from the C target, for which $S_A = 0$ since its has the same number of protons and neutrons.

The Gross-Llewellyn-Smith sum rule will also be tested:

$$S_{GLS} = 0.5 \int_0^1 \frac{dx}{x}(F_3^{\bar{\nu}p} - F_3^{\nu p}). \tag{3.3}$$

This sum rules receives both perturbative and non-perturbative QCD corrections and its Q^2 dependence can be used to extract the strong coupling constant $\alpha_s(Q^2)$. The presence of both H and various nuclear targets would allow an investigation of the isovector and nuclear corrections, adding a tool to test isospin (charge) symmetry.

3.3.4 Strange form factor and axial-current charge radius

The contribution of the strange quark to the vector and axial-vector currents of the nucleon, as well as to the nucleon spin, Δs, are important elements that contribute to our understanding of of the nucleon structure. While the strange quark elastic form factors have been measured with good accuracy in parity-violating electron scattering (PVES) experiments [62], the strange axial-vector form factors are still poorly determined.
SAND can accurately determine the latter from a measurement of the NC elastic scattering off protons $\nu_\mu + p \to \nu_\mu + p$ and $\bar{\nu}_\mu + p \to \bar{\nu}_\mu + p$. In the limit $Q^2 \to 0$ the neutral current differential cross-section is proportional to the axial-vector form factor:

$$\frac{d\sigma}{dQ^2} \propto \left(-\frac{G_A}{2} + \frac{G_A^s}{2}\right)^2, \tag{3.4}$$

where G_A and G_A^s are respectively the total and the strange axial form factors. This process provides the most direct measurement of Δs by extrapolating the NC differential cross-section to $Q^2 = 0$ since in this limit $G_A^s \to \Delta s$.
The detector will also measure the following ratios of NC elastic scattering to the corresponding QE process:

$$\mathcal{R}_{\nu p}(Q^2) \equiv \frac{\sigma(\nu_\mu p \to \nu_\mu p)}{\sigma(\nu_\mu n \to \mu^- p)}, \qquad \mathcal{R}_{\bar{\nu}p}(Q^2) \equiv \frac{\sigma(\bar{\nu}_\mu p \to \bar{\nu}_\mu p)}{\sigma(\bar{\nu}_\mu n \to \mu^+ n)}. \tag{3.5}$$

These measurements will be performed over an extended Q^2 range, using the CC-QE process to determine G_A. This will yield the measurement of the axial current charge radius $r_A \equiv \sqrt{(r_a^2)^{u-d}}$. In addition, a combined analysis with PVES data would allow an accurate determination of all three strange form factors G_E^s, G_M^s and G_A^s [48].

3.3.5 Measurements of the strange PDFs

The high resolution of SAND will enable precision measurements of decay modes of charmed hadrons, such as D^+, D_s Λ_c, and measurement of charm fragmentation and production parameters. Thanks to the low density of STT, SAND will give access to both the $\mu\mu$ and μe inclusive semi-leptonic charm decay channels with high statistics.
The DIS *dimuon* ($\mu\mu$) process has a final state characterized by a muon coming from the neutrino, and an antimuon coming from the semi-leptonic decay of the charmed hadron. This decay can directly probe the strange quark content of nucleons providing a clean and direct access to the $s(x)$ and $\bar{s}(x)$ PDFs. In fact, the *dimuon* cross section can be written as:

$$\frac{d\sigma^2_{\mu\mu}}{dxdydz} = \frac{d\sigma_c}{dxdy} \sum_h f_h D^h_c(z) \mathrm{Br}(h \to \mu + X), \tag{3.6}$$

where $D^h_c(z)$ is the fragmentation function of the charm quark into a given charmed hadron h, carrying a fraction z of the charm quark momentum, and $\mathrm{Br}(h \to \mu + X)$ is the corresponding inclusive branching ratio for the muon decays. From the cross section σ_c the following structure function, and so the PDFs, can be obtained:

$$F_{2,c}(x, Q^2) = 2\,\xi \left[|V_{cs}|^2\, s(\xi, \mu) + |V_{cd}|^2\, \frac{u(\xi, \mu) + d(\xi, \mu)}{2} \right] \tag{3.7}$$

where $\xi = x(1 + m_c^2/Q^2)$ and $\mu = \sqrt{Q^2 + m_c^2}$.
The analysis of both neutrino and antineutrino induced charm production provides the most direct determination of the strange quark content of the nucleon.

Measurements of nucleon structure functions

SAND, will enable measurements of structure functions and cross-sections with accuracies comparable to electron scattering experiments. Using both neutrino and antineutrino DIS the different structure functions F_2, xF_3, F_L and $F_T \equiv F_2 - F_L$, can be determined elucidating the flavor structure of the nucleon. Moreover, PDFs as well as perturbative and non-perturbative corrections can be studied in a broad range of Q^2 and Bjorken x. Data from both hydrogen and the various nuclear targets can be used to separate valence and sea quark distributions, d and u quark distributions.Moreover, a study of F_L will provide information on the gluon distribution.
These proposed studies will provide unique and complementary information to the ongoing programs at colliders and fixed-target electron DIS experiments. The availability of large statistics samples of $\nu(\bar{\nu}) - H$ interactions is crucial to study the structure of nucleon disentangling nuclear effects. In particular, using the isospin symmetry it is possible to obtain a direct model-independent measurement of the free neutron structure functions $F^{\nu n}_{2,3} \equiv F^{\bar{\nu} p}_{2,3}$ and $F^{\bar{\nu} n}_{2,3} \equiv F^{\nu p}_{2,3}$. This measurement allows, in turn, a precise determination of the d quark distribution and of the corresponding d/u ratio up to values of Bjorken x close to 1, testing various model predictions for the limit at $x \to 1$.

Search for Physics Beyond the Standard Model

SAND, thanks to its excellent electron identification capability and its high resolution will be capable of analyzing possible anomalies in the ν_μ, $\bar{\nu}_\mu$ (disappearance) and ν_e, $\bar{\nu}_e$ (appearance)

charged-current spectra. Oscillations involving sterile neutrinos can be tested considering the ratios:

$$R_{e\nu}(L/E) = \frac{(\nu_e N \to e^- X)}{(\nu_\mu N \to \mu^- X)}, \qquad \bar{R}_{e\nu}(L/E) = \frac{(\bar{\nu}_e N \to e^+ X)}{(\bar{\nu}_\mu N \to \mu^+ X)}.$$

Moreover, SAND will also enable searches for Dark Sector physics, heavy sterile neutrinos (e.g., Majorana singlet fermions), axion-like particles, dark photons, and light (sub-GeV) dark matter.

Chapter 4

Simulation Framework

4.1 Introduction

The simulation framework used in this thesis features different software designed for event generation, digitization, and reconstruction. The simulation chain starts with the generation of neutrino interactions in matter using the neutrino event generator GENIE [63], presented in Sec. 4.2. It continues with the particle propagation inside the detector performed by Edep-Sim [64], a tool based on Geant4 [65], described in Sec. 4.3. Finally, it concludes with the digitization and reconstruction of the signal performed by Sand-reco, a C++ tool developed by the SAND collaboration [66], in Sec. 4.4. A scheme of the SAND simulation framework is illustrated in Fig. 4.1. For the purpose of the analysis illustrated in Chap. 5, an additional step, developed specifically for this work, is performed to group the necessary variables; a list of these variables can be found in App. 5.8.

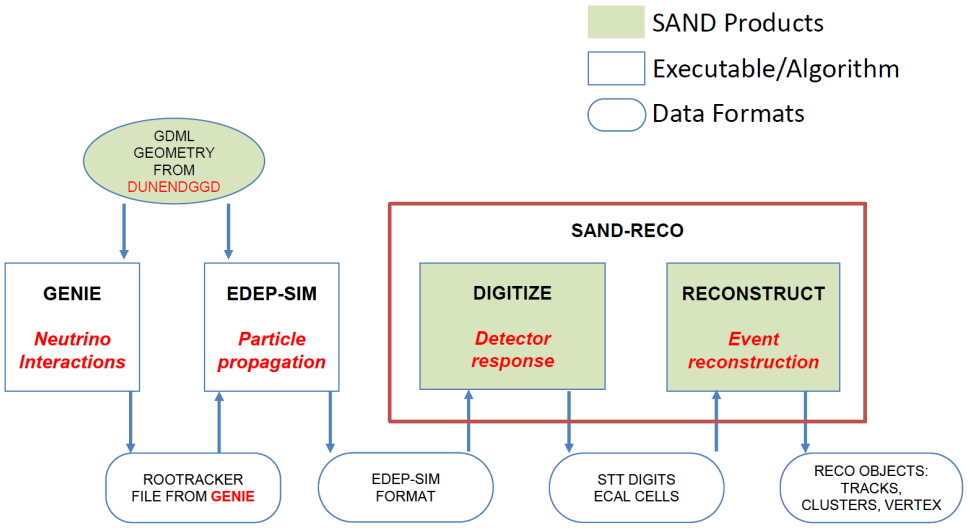

Fig. 4.1: *Chain diagram of the SAND simulation* [67].

4.2 GENIE

GENIE [63] (Generate Events for Neutrino Interaction Experiments) is a widely used Monte Carlo events generator for the experimental neutrino physics community. It is a ROOT-based large-scale software system exploiting an object-oriented methodology. It consists of $\sim$ 120,000 lines developed entirely in C++. The first official physics release of this generator was made in August 2007, in this thesis the version (v3.06.00) is used.

GENIE provides interactions within a wide energy range, from $\sim$ 1 Mev to $\sim$ 1 PeV, for all nuclear target and all neutrino flavors. It includes many physics models that can be categorizes into nuclear physics, cross section, hadronization and final state interactions models. Moreover, it contains several Beyond Standard Model channels, and tuned models from global data analysis.

GENIE allows to customize the neutrino interaction with detailed flux and detector geometry descriptions. The flux descriptions are provided by experiment-specific beam-line simulations, while the detector geometry descriptions derive from engineering drawings.

In the context of the DUNE collaboration, the beam flux simulations are generated by the LBNF (Long Base Line Neutrino Facility) Beam simulation group. Beam flux information can be stored and propagated using different file formats. The `GSimpleNtpFlux` files that contain flux information with minimal formatting, and the `Dk2nu` files that also include information about the hadrons and muons generating the neutrino beam. The first format has been used since it already contains all the information needed for the analysis performed in this thesis.

The geometry of the detector volume in which the interactions are generated is provided to GENIE via GDML [68] (Geometry Description Markup Language) files. The GDML files are generated by the python based software system GGD [69] (General Geometry Description), which provides a description of a constructive solid geometry. The ND collaboration has developed its own geometry generator called `dunendggd` [70], based on GGD.

4.3 Edep-Sim

Edep-Sim (energy deposition simulation) is a wrapper around the GEANT4 toolkit for the simulation of the passage of particles through matter and energy deposition in the detector. It takes as input kinematic files, such as GENIE output files, and geometry files, such as the GDML ones[1]. Knowing the kinematics of the event and the geometry of the detector, Edep-Sim propagates the particles inside the material. In the output, it provides a root standard tree, called `edep`, containing two objects: a TGeoManager containing the detector simulated geometry, and a tree that for each entry has a TG4Event object, a specific Edep-Sim class that stores information on the primaries particles, their tracks, and energy deposits.

4.4 Sand-reco

Sand-reco is a framework for event reconstruction developed in C++ by the SAND Physics and Software working group.

[1] In this thesis only GENIE and GDML are used, but Edep-sim supports also other file formats both for kinematics and geometry.

Sand-reco is currently under an intense period of development, as such, the following description portrays its structure at the time of production of this thesis. Firstly, the generated data from Edep-sim are converted into a digital signal in order to simulate the electronic response of the tracker and the calorimeter (ECAL). In a second step, the ECAL cells are clusterized while the tracks of the tracker are reconstructed to identify the trajectories. Finally, some optional tools can be used to verify the reconstruction and display the events.

In total, Sand-reco provides five executables:

- `Digitize` performs the digitization; it converts the simulated energy deposit into the detector simulated response. It takes as input the output files from Edep-sim (`edep`) and gives a ROOT `digit` file.
- `Reconstruct` performs the reconstruction of the tracks in the tracker and of the clusters in the ECAL. It takes as input the `edep` and `digit` files, then returns a root file called `reco`.
- `Analyze` takes as input the `edep` and `reco` files and returns a new `reco` with particles organized with all their true and reconstructed quantities.
- `FastCheck` produces different plots to check the status of the produced data.
- `Display` displays the events.

In this thesis, only three executables are used: `Digitize`, `Reconstruct`, and `Analyze`. Note that `Analyze` is not the software used to generate the analysis files with the variables described in Appendix 1. That tool was developed specifically for this thesis and operates on the output produced by `Analyze`.

4.4.1 Digitization

The digitization provides a simulated detector response coming from the DAQ system based on the energy deposits of the particles. In Sand-reco, the digitization is implemented for the ECAL and for the tracker in two different ways. In the ECAL, it is performed by dividing the calorimeter modules in cells and simulating the photo-electron production in the photomultiplier tubes. In the STT, it is performed by assigning each hit and energy deposition to the correct straw tube.

ECAL Digitization

The digitization of the ECAL is simulated by following the module segmentation already described in Sec. 3.2.2. Each module is divided into 5 layers, in turns divided into 12 cells. The light produced in each cell is read out by a PMT from both sides of the module, the number of photo-electrons N_{pe} associated to each cell is simulated taking into account the light attenuation length along the fiber and the energy to photo-electron conversion factor. In detail, it is obtained from a Poisson distribution with mean value given by:

$$\begin{aligned} &\mu_{pe} = dE \cdot A \cdot E_{pe} \\ &A = p_1 \cdot \exp\left(-\frac{d}{alt_1}\right) + (1 + p_1) \cdot \exp\left(-\frac{d}{alt_2}\right) \end{aligned} \tag{4.1}$$

where E_{pe} is the conversion factor, A is the attenuation factor with d distance between the hit and the photo-cathode, $p_1 = 0.35$, $alt_1 = 50$ cm and alt_2 changes with the layers. For each photo-electron produced, the arrival time to the PMT must be associated:

$$\begin{aligned} t_{pe} &= t_{cross} + t_{decay} + d/v_{fiber} + \text{Gauss(1ns)} \\ t_{decay} &= t_{scint} \left(\frac{1}{r_{ph} - 1} \right)^{t_{scex}} \end{aligned} \tag{4.2}$$

where t_{cross} is the time associated with the hit from the MC truth, d/v_{fiber} is the propagation time of the photons along the fiber, and Gauss(1ns) is the gaussian smearing that corresponds to the PMT uncertainty. Moreover, t_{decay} is the scintillation decay time obtained by applying the same formula used by the KLOE collaboration, where $t_{scint} = 3.08$ ns, $t_{scex} = 0.588$ and r_{ph} is a random number between 0 and 1.

STT Digitization

The digitization of the STT is simulated in two steps. At first, all the hit produced in the same straw tube are grouped in a cluster. Then, for each cluster, the hits are organized from the first to the last and the coordinates of the digits are obtained as the average between the values of the first and the last point of the cluster. The energy of the digit is obtained by summing all the energies deposited in the cluster.

4.4.2 Reconstruction

The reconstruction, as the digitization, is divided between the ECAL and the tracker. In the first, a cluster reconstruction is performed; in the second, a track reconstruction using a Kalman filter takes place.

ECAL reconstruction

The reconstruction in the ECAL starts from the output of the digitization. From the simulated light of the two PMTs, the position of the cell is obtained using the relation:

$$x_c = \frac{v}{2}(t_A - t_B), \tag{4.3}$$

where t_A and t_B are the times from the PMTs and v is the velocity of the photo-electrons. Starting from the cells, a "pre-clustering" phase takes place, where spatially neighbor cells are added together. Then, a "splitting" phase and a "merging" phase are performed. In the "splitting" phase, the spread in time of pre-clusters is evaluated; if the time criteria are satisfied, the pre-clusters are divided into time quadrants. During the "merging" phase, pre-clusters are checked in time and position, and merged if they have been split incorrectly [71].

Tracker reconstruction

The reconstruction in the tracker is performed using a Kalman filter (KF) which consists in a recursive application of the least-squares regression for track fitting. The KF was first used

in a particle physics application by the DELPHI experiment, to estimate the state of a linear system under random perturbation [72]. Nowadays, the most popular version of the KF is actually an Extended Kalman Filter (EKL) that is able to handle non-linear systems. This is essential for applying a Kalman filter to the reconstruction of helical trajectories produced by charged particles propagating in magnetic fields. In SAND, this last version is used.

The KF is an iterative algorithm that performs many steps to estimate the state of a dynamical system, a track in this case. Each step is based on two phases: prediction and update. In the first phase, it predicts some kinematical parameters such as position and momentum of a particle, while in the second phase it updates the prediction comparing it with the subsequent measurement obtained from the hits in the tracker. At the time of this thesis, the hits for the comparison are taken from the Monte Carlo truth. In detail, the trajectory points that come from the Edep-Sim step are clusterized in *tracklets* according to their position inside the tracker. Then, the *tracklets* are smeared with Gaussian uncertainties. These *tracklets* are the actual hits used for the comparison.

A complete description of SAND's KF can be found in this work [73].

Chapter 5

Analysis of neutrino-hydrogen interactions

5.1 Introduction

The currently available data from $\nu(\bar{\nu}) - H$ interactions were last collected by bubble chamber experiments at ANL [74], BNL [75] and FNAL [76] in the 1980s. Despite the excellent resolution of these measurements, the overall statistics are limited to roughly 16k $\nu - H$ and 9k $\bar{\nu} - H$ CC interactions, due to the relatively small target mass and the low-power beams available at the time. In general, liquid-hydrogen–based experiments are limited in total target mass by safety requirements.

DUNE, thanks to its high intensity flux, will enable studies on $\nu(\bar{\nu}) - H$ interactions with unprecedentedly high statistics. In this context, interactions on hydrogen are obtained using a technique called "Solid Hydrogen" which consists in a statistical subtraction of events on graphite (C) targets from those on polypropylene (C_3H_6) targets. Preliminary studies suggest that this technique could be employed as a valid and realistic alternative to liquid H_2 detectors [77].

A sample of neutrino interactions on H would be extremely valuable for DUNE's oscillation measurement program. As discussed in Sec. 3.3.1, these interactions are completely devoid of nuclear-smearing effects, which are a major source of systematic uncertainty In this chapter, we evaluate SAND's ability to select a sample of antineutrino charge current (CC) interactions on hydrogen. For this study we consider the $\bar{\nu}_\mu + \mathrm{H} \rightarrow \mu^+ + n$ channel and follow an approach similar to that outlined in [59].

5.2 (Anti)neutrino interaction kinematics

(Anti)neutrino interactions on hydrogen are characterized by a distinct kinematic signature. Since hydrogen can be approximated to a free proton, charge current events are expected to be perfectly balanced on the plane transverse to the neutrino direction.

On the other hand, events on different nuclear targets are subject to nuclear effects, which modify the final state leading to a non-zero missing transverse momentum p^T (see Sec. 1.2.2).

The missing transverse momentum is defined as:

$$p^T = \sum_i {p_i}^T \tag{5.1}$$

where $\vec{p_i}$ is the momentum of the final state particles i, and T identify the projection on the plane transverse to neutrino direction.

The interaction considered in this analysis as signal is: $\bar{\nu}_\mu + H \to \mu^+ + n$, that is a CC-QE interaction whose phenomenology is illustrated in Sec. 1.2.2. Since in the final state there are only an antimuon and a neutron, and since H in the initial state is at rest, the kinematics of the interaction is fully determined. Indeed, once the μ^+ four-momentum is reconstructed, the energy of the neutrino can be obtained as:

$$E_{\bar{\nu}}^{reco} = \frac{M_n^2 - m_\mu^2 + M_p^2 + 2M_p E_\mu^{reco}}{2(M_p - E_\mu^{reco} + |p_\mu^{reco}| \cos\theta_\mu^{reco})} \tag{5.2}$$

where M_n, M_p and m_μ are, respectively, the neutron, proton and muon masses, E_μ^{reco} and p_μ^{reco} are the reconstructed muon energy and momentum, and θ_μ^{reco} is the muon emission angle. From this reconstructed neutrino energy, the reconstructed neutrino momentum can be inferred as: $\vec{p}_{\bar{\nu}}^{\,reco} = |p_{\bar{\nu}}^{reco}| \hat{p}_{\bar{\nu}}^{reco}$, with $|p_{\bar{\nu}}^{reco}| = E_{\bar{\nu}}^{reco}/c$ and with $\hat{p}_{\bar{\nu}}^{reco}$ taken from the neutrino beam direction. In the current simulated detector configuration, the beam is along the z-axis and is bent at an angle $\alpha = -5.8°$. From these neutrino reconstructed quantities, the neutron predicted energy and momentum can be obtained as:

$$E_n^{pred} = E_{\bar{\nu}}^{reco} + M_p - E_\mu^{reco} \tag{5.3}$$

$$\vec{p}_n^{\,pred} = \vec{p}_\nu - \vec{p}_\mu \tag{5.4}$$

Assuming that the neutron travels in a straight line with no interactions inside the tracker, the point $\vec{x}_{hit}^{\,pred}$ where the neutron is expected to produce a hit in the calorimeter can be predicted. With the same approach, the time when the hit occurs can be estimated as:

$$t_{hit}^{pred} = \frac{|\vec{x}_{hit} - \vec{x}_{vtx}|}{\beta c} \tag{5.5}$$

where $\vec{x}_{vtx}$ in the interaction vertex and $\beta = E_n^{pred}/|p_n^{pred}|$.

5.3 Event generation

For this analysis, 2 million of $\bar{\nu}_\mu$ CC interactions, corresponding to $\sim 4.6 \cdot 10^{20}$ p.o.t.[1] (~ 5 months of data taking, at 1.2 MW of beam power, RHC mode), were generated within the SAND inner volume containing the STT and GRAIN. Only CC interactions were generated because here it is assumed that muons can be identified with high efficiency and purity. The proper identification will be done by a particle ID algorithm, still under development at the time of this thesis. The distribution of the simulated vertex positions is shown in Fig. 5.1.

For the study of the "Solid Hydrogen" case, only the neutrino interactions occurring in the STT targets are selected. The positions of neutrino vertices on polypropylene (left) and

[1] Protons on Target is a basic unit used to measure the exposure in fixed-target experiments.

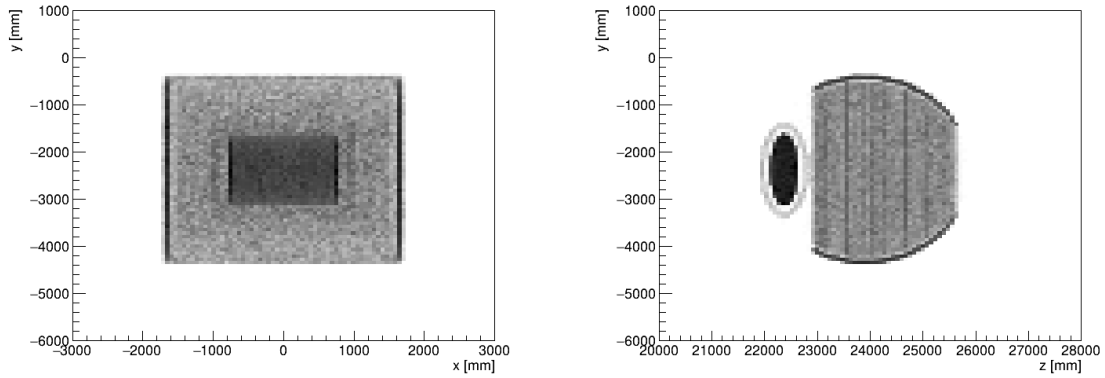

Fig. 5.1: *Interaction vertices of the simulated events in the SAND inner volume. On the left the vertices on the xy plane, on the right the vertices on the zy plane.*

on graphite (right) targets are shown in Fig. 5.2. The events in polypropylene account for about 50% while the events in graphite are 7% of all total generated sample. In the following, "polypropylene" and "plastic" are to be understood as synonymous.

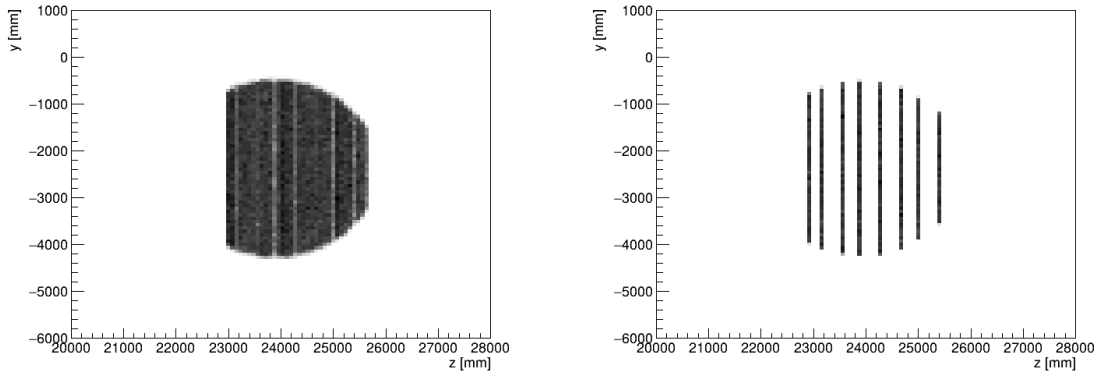

Fig. 5.2: *Interaction vertices on the zy plane inside the tracker targets of the . On the left, events on polypropylene; on the right, events on graphite.*

The true distribution of the missing transverse momentum p^T for interactions with H and C nuclei is shown in Fig. 5.3. As can be seen in the plot, all the charge current interactions on hydrogen have a zero missing transverse momentum, while the charge current interactions on carbon show a continuous distribution.

The interactions of the GENIE simulated sample are classified according to the interaction type (QE, RES, DIS, MEC, COH)[2] and the target nuclei (H in plastic, C in plastic, C in graphite). Their energy distribution is shown in Fig. 5.4. Deep inelastic scattering and resonance production processes are dominant both in graphite and polypropylene. The signal ("CC-QE on H in plastic") is about 10% of the total number of simulated interactions.

The products of neutrino interactions are then propagated through the SAND volume. The detector response is simulated, and the events are reconstructed as explained in Chap. 4.

[2]Quasi-Elastic, Resonance, Deep Inelastic Scattering, Meson Exchange Current, Coherent [63].

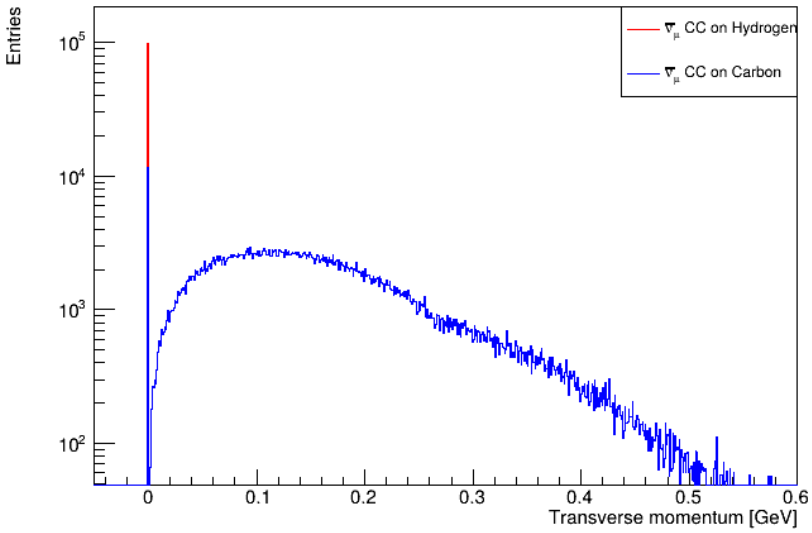

Fig. 5.3: *Missing transverse momentum distribution of CC interactions on hydrogen (red), and the one for CC interactions on carbon (blue).*

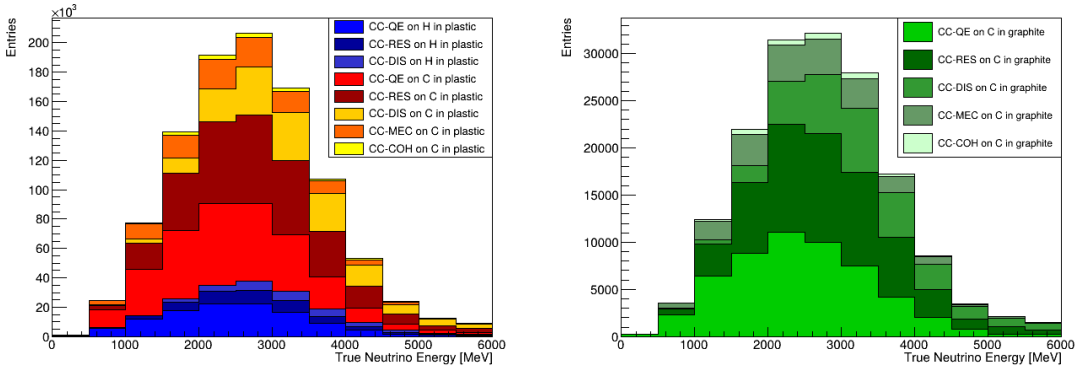

Fig. 5.4: *Energy distribution of all the types of CC interactions in the generated sample. On the top, events on polypropylene; on the bottom, events on graphite.*

Specifically, the muons were reconstructed using the Kalman Filter described in Sec. 4.4.2, while the neutrons were "reconstructed" as clusters in the calorimeter as detailed in Sec. 4.4.2.

5.4 Muon reconstruction performance

The muon reconstructed quantities are taken from the output of the reconstruction. In Fig. 5.5 the residuals of the reconstructed muon momentum components along the x,y and z axis are shown.

The muon momentum resolution is evaluated as function of two key quantities: the number of tracks points and the true muon momentum. In this reconstruction, a point corresponds to one *tracklet* of the Kalman Filter described in Sec. 4.4.2. The resolution is obtained from the width of the distribution of the muon momentum residuals fitted with a Gaussian. In Fig. 5.6, the resolution as function of the number of points and as function

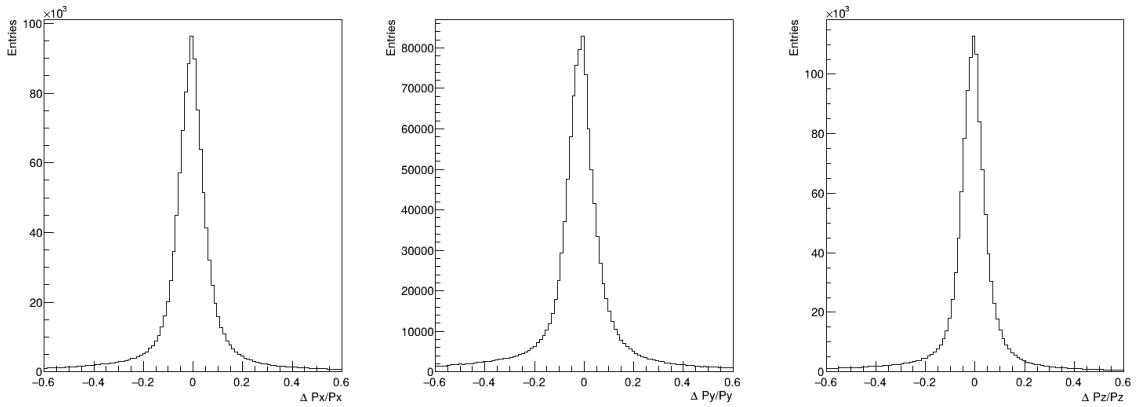

Fig. 5.5: *Residuals of muon momentum components. From the top to the bottom, residuals along the x,y and z axis.*

of the muon momentum is shown. As can be seen from the plots, the minimum achievable resolution is at 5%, which is slightly larger with respect to previous studies [59].

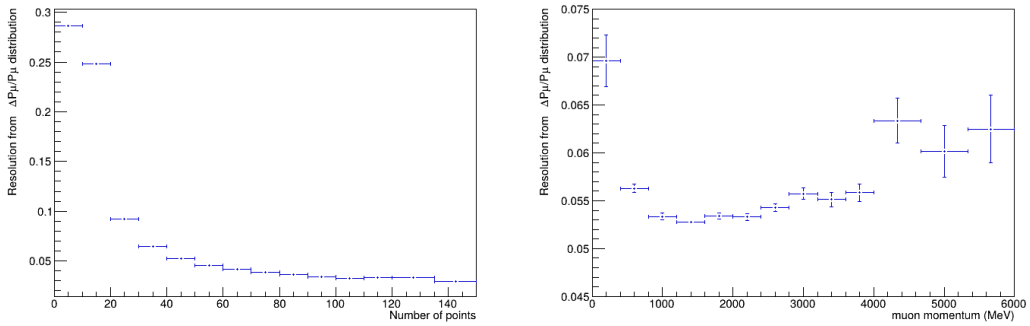

Fig. 5.6: *On the top, the resolution as function of the number of points. On the bottom, the resolution as function of the muon momentum. The resolution is obtained considering the width of the gaussian fit on the muon momentum residuals.*

5.5 Inference on neutrino energy and neutron momentum

For signal events, starting from the reconstructed muon quantities, the neutrino energy as well as the predicted neutron momentum can be inferred using Eqs. 5.2 and 5.3. The residuals between the true and the calculated quantities for generated signal events are shown in Fig. 5.7. The residuals for the neutrino momentum component along the x-axis have the constant value -1, this is due to the fact that the reconstructed neutrino momentum follows the beam direction which has no x-component. In Fig. 5.8, the residuals for the neutrino and neutron energy, respectively, are presented for true signal events

.

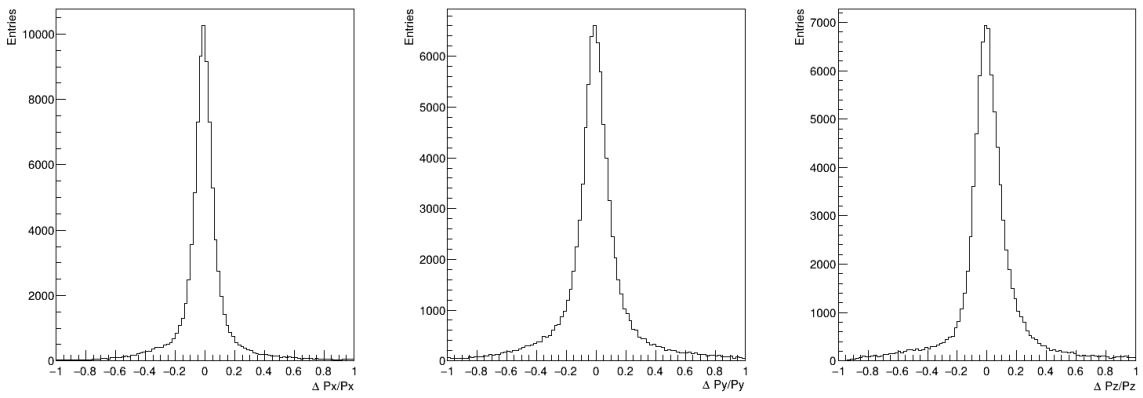

Fig. 5.7: *From left to right the residuals along the x,y and z axes of the neutron momentum for signal events.*

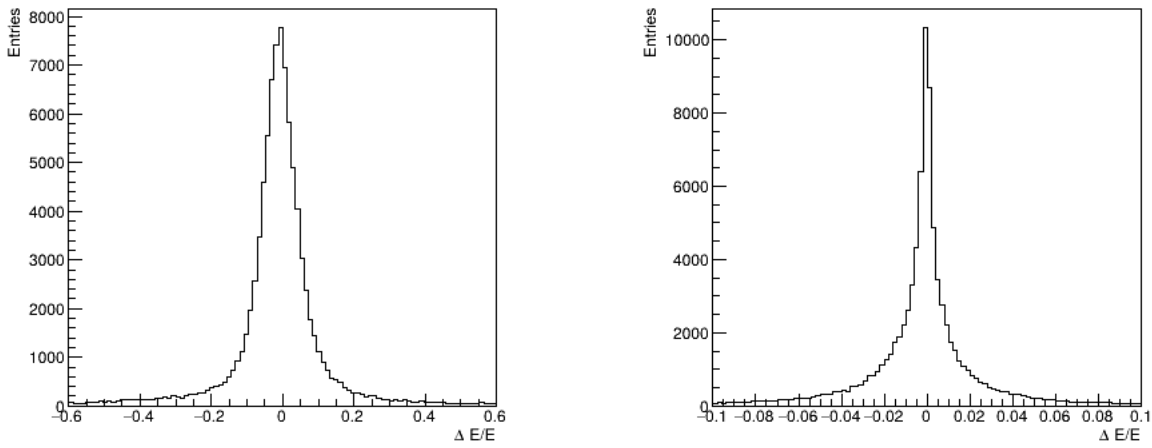

Fig. 5.8: *On the left, neutrino energy residuals for generated signal events. On the right, for neutrons.*

5.6 Event Selection

To select the signal events, several cuts were applied on the reconstructed simulated sample. In addition to the fiducial-volume cut mentioned in Sec. 5.3, which selects only the events with the interaction vertex inside the STT, four additional cuts were applied. The first one is a quality cut based on the performance of the reconstruction algorithm in the Sand-reco framework (see Sec. 4.4). The second cut is a requirement on the charge multiplicity of the events. Finally, the last two cuts are applied to select events with a neutron candidate whose position and time estimates are in good agreement with the ones predicted by the kinematics of CC-QE on H interactions.

5.6.1 Muon reconstruction status and multiplicity

The reconstruction status cut allows to select only events with a successful reconstruction. The Kalman filter computes a chi-square for the track in each iteration step; when this chi-square exceeds a certain threshold, the Kalman Filter stops. In these cases, it returns a failure flag. Thanks to this cut, the events with the failure flag are removed.

The charge multiplicity cut selects the events with only one reconstructed track associated with the interaction vertex.

5.6.2 Neutron position and time

The cut on the neutron position is performed assuming that the neutron has the momentum given in Eq. 5.3, and that it travels in a straight line without any interaction. Under these assumptions, the intersection points $\vec{x}_1^{\,pred}$ and $\vec{x}_2^{\,pred}$ between, respectively, the innermost and outermost layers of the calorimeter and the neutron predicted direction, are computed.

For the barrel calorimeter, the predicted points are computed considering the intersection with two concentric cylinders, while for the endcaps they are computed considering two parallel planes along the x-axis. The two intersection points are used to define a cylinder whose axis is the segment connecting them and whose radius is $r = 100$ mm. All the events with at least one cluster that fall inside the defined cylinder are selected. The radius of the cylinder is chosen considering the distance distributions in Fig. 5.10, where the signal and the background events are shown as a function of the distance between the cylinder axis and the center of the nearest cluster. As can be seen from the plot, after 100 mm the background exceeds the signal.

In Fig. 5.9 event displays for a signal (left) and background (right) events are shown. The inner and outer layers of the calorimeter are drawn as two concentric cylinders containing the tracker (here not shown). Inside the cylinder volume the interaction vertex is printed in red. The true neutron momentum (black) and the predicted neutron momentum (red) start from this vertex. The cluster points reconstructed from the energy deposits in the calorimeter are illustrated in blue, while the predicted intersections $\vec{x}_1^{\,pred}$ and $\vec{x}_2^{\,pred}$ are shown in green. For the signal, the neutron momentum predicted using Eqs. 5.3 almost fully agrees with the true momentum. For the background the prediction on the neutron momentum is not comparable with the true value since Eqs. 5.3 do not hold for the background interactions. Moreover, the cluster points supposed to be associated with the neutron are very close to the predicted

$\vec{x}_1^{\,pred}$ and $\vec{x}_2^{\,pred}$ for signal events, whereas this is not true for background events. This is the important distinction on which the selection is based.

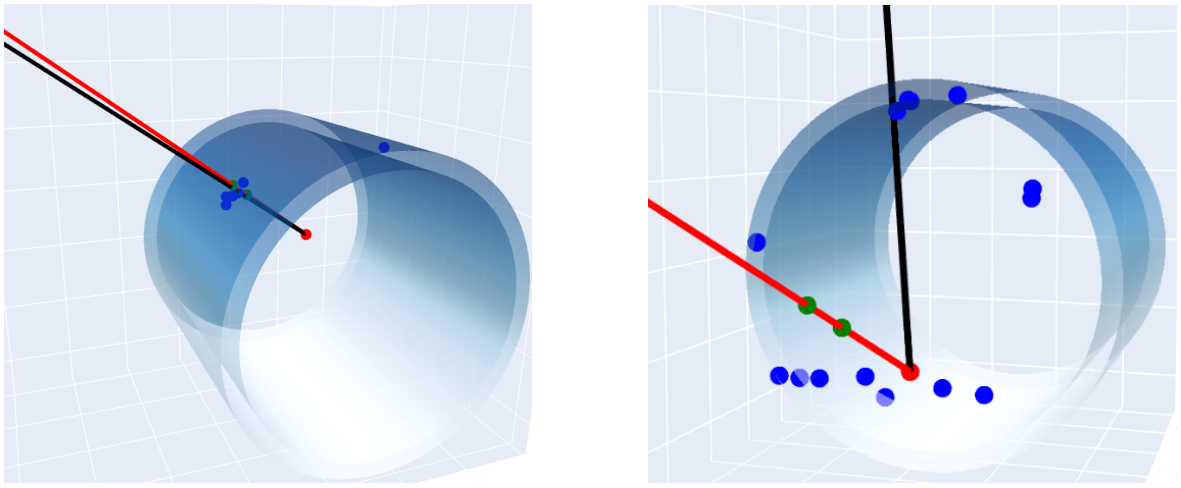

Fig. 5.9: *On the left, event displays for a signal event, on the right and a background event. In the inner volume of the calorimeter the interaction vertex from which the true neutron momentum (black) and the predicted neutron momentum (red) start. In blue all the calorimeter clusters and in green the predicted intersection points* $\vec{x}_1^{\,pred}$ *and* $\vec{x}_2^{\,pred}$*. For the signal can be seen the prediction on the barrel calorimeter, for the background the prediction on the endcaps.*

The cut on the neutron timing was applied considering all the previous assumptions. In this case, all events with a $|\Delta t| < 10$ ns are selected. The Δt is the difference between the time associated with the closest cluster to cylinder axis and the time that the neutron would take to reach that same cluster. The value of $|\Delta t|$ is chosen considering the distributions illustrated in Fig. 5.11, where it can be seen that in the region where $|\Delta t| > 10$ ns the background to signal ratio is the worst in the sample.

5.6.3 Selection summary

In Tab. 5.1, the percentages of events removed for each cut are summarized. For clarity, the events are divided into six categories according to the type of interaction, target, and interaction vertex position. This distinction is done considering true information. The first row represents the signal subsample, while the others represent the background. On the columns we show the effects of the cuts in rejecting events, applied progressively from left to right. In the first column the percentage of events which are removed by the fiducial volume cut is shown. As expected, this selection does not remove the events on the target. In the second column, the cut on the reconstruction status is shown to remove almost the same percentage in each category, with the exception of the events with vertices outside of the target slabs, for which poorer tracker performance is expected. In the third column, the cut on the charge multiplicity, does not affect signal events. This is because the signal is characterized by the presence of an antimuon and a neutron. The fourth column corresponds

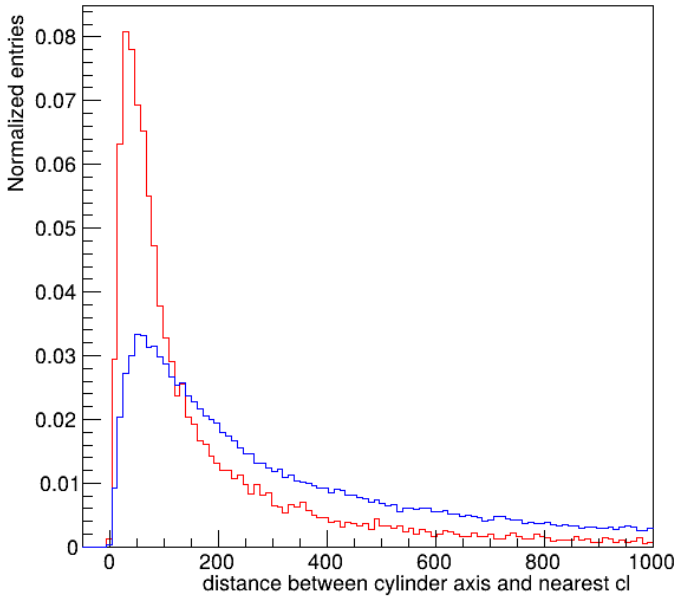

Fig. 5.10: *Normalized number of events as a function of the distance between the segment whose endpoints are the intersection points between the predicted neutron direction and the first and last layer of the calorimeter. In red signal events, in blue background events.*

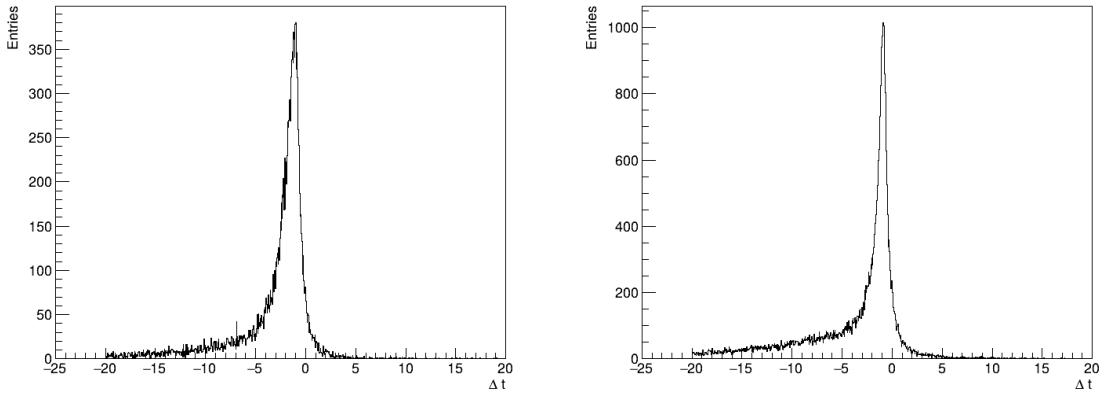

Fig. 5.11: *Number of events as a function of the time difference between the time associated with the cluster and the time that the neutron would take to reach that same cluster. On the left signal events, on the right background events.*

to the cut on the neutron space correspondence. This cut is the most restrictive, as it removes many events in each category. Because of this cut, many signal events are also removed, even if in a smaller amount with respect to the background. This is because, in some cases, the neutron does not leave a cluster in the calorimeter. Finally, in the last column, we show the effects of the cut on the neutron time correspondence. In this case, the signal is only slightly removed while the background is more affected. In Fig. 5.12, the total number of events after each selection step is presented. As can be seen, the most restrictive cut is the one on the neutron space correspondence. The cut on the neutron time correspondence slightly

improves this one.

The composition of the sample as a function of the reconstructed $\bar{\nu}_\mu$ energy is shown in Fig. 5.13 for events in plastic. The selected sample is composed of CCQE events on H (blue), CC events on C (red), and CC events, which are not QE, on H (green). After requiring a successful reconstruction, the sample is dominated by interactions on C. After requiring the existence of only one track, the number of these interactions decreases enhancing the the signal with respect to the background. The composition of the sample becomes signal dominated after requiring the neutron correspondence in space. Finally, the request on time emphasizes this situation. These considerations hold also for events on H that are not QE.

		Target nucleus	**Vertex position**	**Fiducial volume**	**Reco status**	**Charge multiplicity**	**Space match**	**Time match**
S	$\bar{\nu}_\mu$**CCQE**	H	Plastic	0.00	19.18	0.00	77.46	4.90
B	$\bar{\nu}_\mu$**CCQE**	C	Plastic	0.00	17.73	14.13	92.10	18.42
	$\bar{\nu}_\mu$**CC**	H	Plastic	0.00	19.41	67.87	86.62	22.12
	$\bar{\nu}_\mu$**CCQE**	C	Graphite	0.00	17.36	16.19	93.08	16.88
	$\bar{\nu}_\mu$**CC**	H	Everywhere	0.00	62.09	50.50	68.29	60.92
	$\bar{\nu}_\mu$**CC**	all	Everywhere	24.82	37.30	57.21	80.19	17.72

Tab. 5.1: *Removed sample percentage after each cut for signal (S) and background (B). The cuts are applied progressively and the percentages after each cut are calculated with respect to the previous total. Signal events are in the first row.*

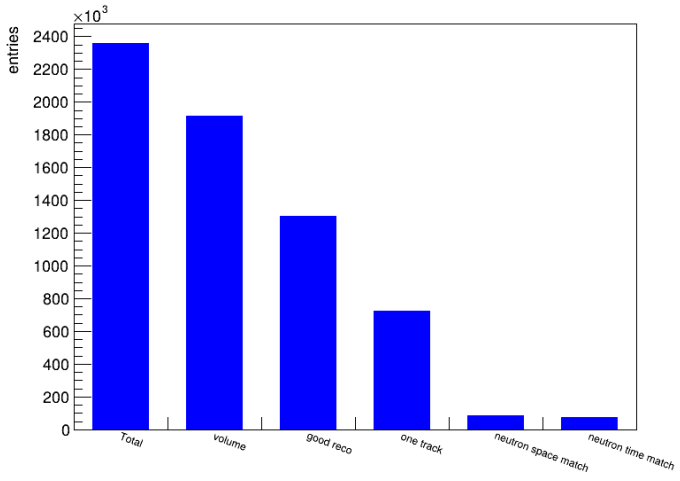

Fig. 5.12: *In each bin, the number of events in each step of the selection. In the first bin there is the total number of events, in the second the number of events inside the fiducial volume, in the third the events with a successful reconstruction, in the fourth the events with one track, in the fifth and in the sixth the number of events with neutron space and time correspondence, respectively.*

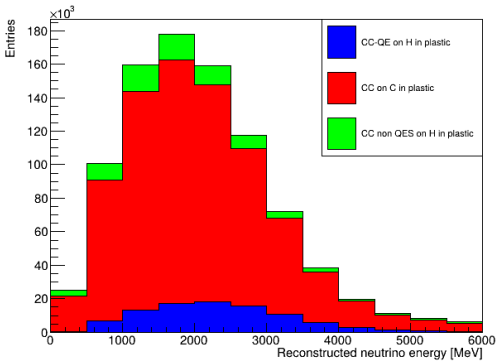

(a) *Sample composition after requiring a successful reconstruction.*

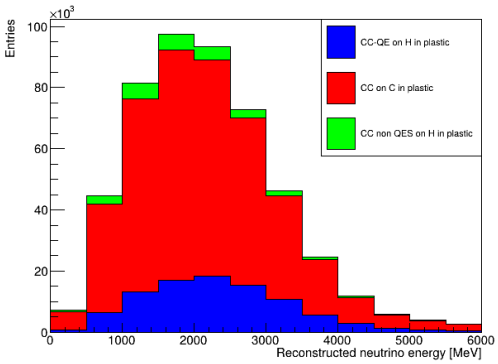

(b) *Sample composition after requiring one track.*

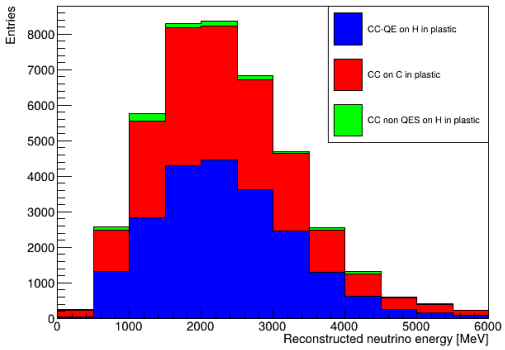

(c) *Sample composition after requiring neutron space correspondence.*

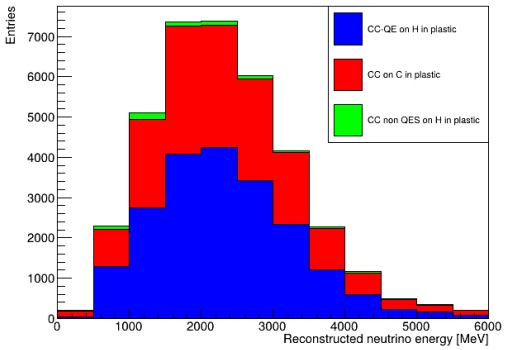

(d) *Sample composition after requiring neutron time correspondence.*

Fig. 5.13: *Sample composition, as function of the reconstructed $\bar{\nu}_\mu$ energy, of events on C_3H_6 after different cuts. In blue the CCQE events on H, in red CC events on C, in green other CC events on H.*

5.6.4 Statistical subtraction

The applied cuts are not sufficient to select interactions on hydrogen with high efficiency and purity. This is because these cuts exploit peculiar characteristics of the signal kinematics, which, as already explained, is well determined and fully constrained by the measurement of the muon momentum. Even a topological cut on the vertex position could remove the background from interactions on graphite. However, the resulting sample would be contaminated by interactions on C in plastic. A multi-variate analysis to identify and remove these interactions would require a precise understanding of the kinematics of neutrino interactions with complex nuclei and of nuclear effects on the final states. At the current stage, such an analysis would suffer from significant systematic uncertainties. Therefore, in this thesis, a statistical subtraction of the background from interactions on the carbon in the plastic ("Solid Hydrogen" technique) was chosen. This technique allows for a compensation of the systematic uncertainties.

The statistical subtraction is applied between events on polypropylene (C_3H_6) targets and those on graphite (C) targets. In detail, the distribution of the events on graphite, multiplied by a weight factor, is subtracted from the distribution of the selected events on C_3H_6 illustrated in Fig. 5.13. This weight factor $w = 5.25$ is introduced to balance the mass quantity of carbon in graphite and polypropylene; w is defined as the ratio between the generated interactions on C in polypropylene and the interactions on C in graphite. The distributions of events on C are shown in Fig. 5.14. The distribution of events on C in graphite (black dots) is still slightly smaller with respect to the same distribution in plastic, even after the correction of the weight factor. However, their ratio is very close to one over the whole energy range.

The distribution of events on H obtained with this technique is shown in Fig. 5.15. This sample is mainly composed of signal events; however, it also contains non-QE CC interactions on H in plastic that are not fully removed with the selection cuts.

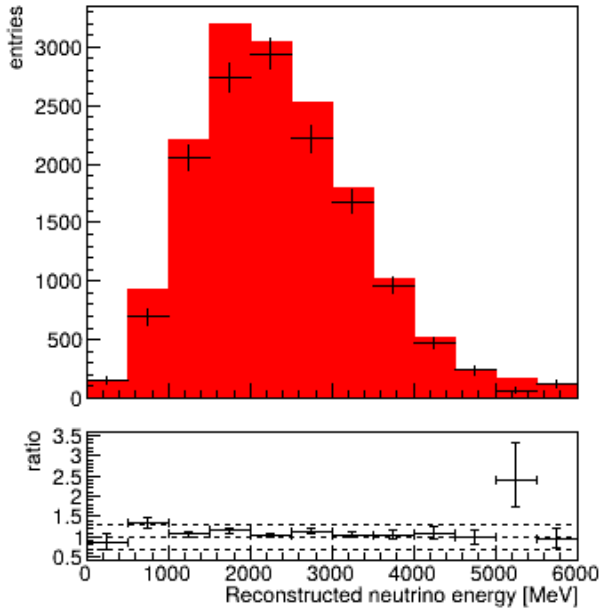

Fig. 5.14: *On the top, the distribution of events on C in plastic (red), the distribution of events on C in graphite multiplied by the weight factor (black dots). On the bottom the ratio between the two distributions, as expected the ratio is almost one.*

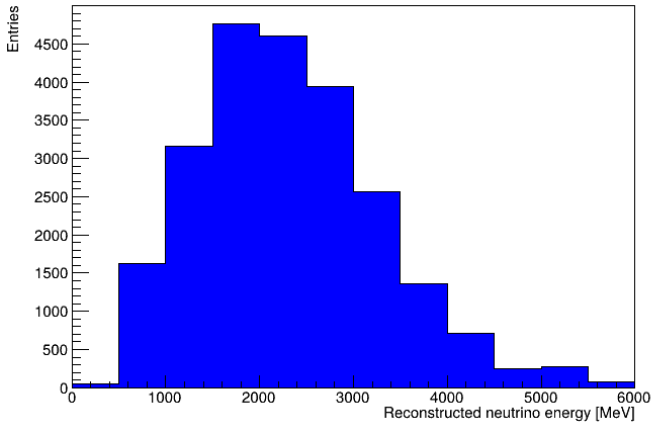

Fig. 5.15: *Distribution of the events on hydrogen obtained via the statistical subtraction on events on C from those on C_3H_6.*

5.7 Unfolding Procedure

The unfolding procedure allows to infer the true distribution of a given quantity, starting from its measured reconstructed distribution, that is modified by detector effects such as resolution, efficiency and acceptance. In this analysis, the unfolding is performed with `RooUnfold` [78] to obtain the "true" rate of events on H in C_3H_6 target.

Fist of all, the selected distribution of events on hydrogen obtained via statistical subtraction, here for simplicity h_i, is multiplied by the acceptance. This multiplication $h_i^{corr} = h_i \times A_i$ corrects the events that are generated outside the fiducial region of the signal space phase, but still pass the detector selection. The acceptance A_i bin-by-bin is calculated as:

$$A_i = \frac{N_i^{Reco\&True}}{N_i^{Reco}}, \tag{5.6}$$

where i is the bin index, N_i^{Reco} are the reconstructed events that pass the selection cuts explained in Sec. 5.6 and $N_i^{Reco\&True}$ are the ones that also pass the true fiducial selection. Acceptance is shown in Fig. 5.16.

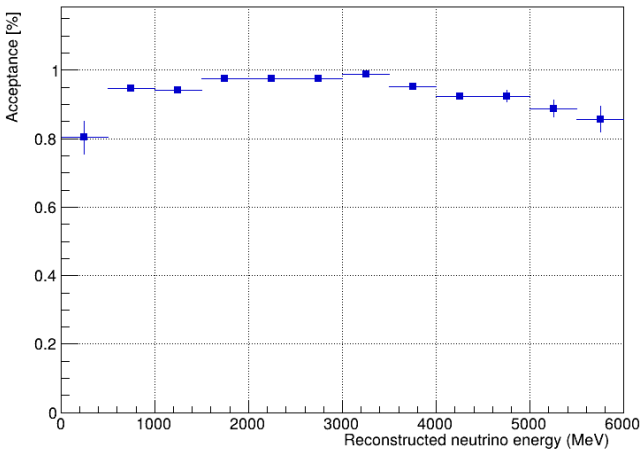

Fig. 5.16: *Acceptance as a function of the reconstructed neutrino energy.*

The corrected distribution h^{corr} is the one to which the Bayesian unfolding method is applied, obtaining: $h^{unfold} = U(h^{corr}, M)$, where U is the unfolding operator and M is the migration matrix shown in Fig. 5.17. The migration matrix is built considering on the x-axis the reconstructed neutrino energy and on the y-axis the true neutrino energy. It is filled with true signal events that pass the selection cuts.

Finally, the unfolded rate h^{unfold} is corrected for the efficiency: $h_i^{final} = h_i^{unfold}/\epsilon_i$. This ratio corrects the inefficiency of the selection and reconstruction of events. The efficiency is defined as:

$$\epsilon_i = \frac{N_i^{True\&Reco}}{N_i^{True}}, \tag{5.7}$$

where i is the bin index, N_i^{True} are the generated true signal events inside the fiducial volume, and $N_i^{True\&Reco}$ are the ones that also pass inclusive detector selection. The efficiency is shown in Fig. 5.18

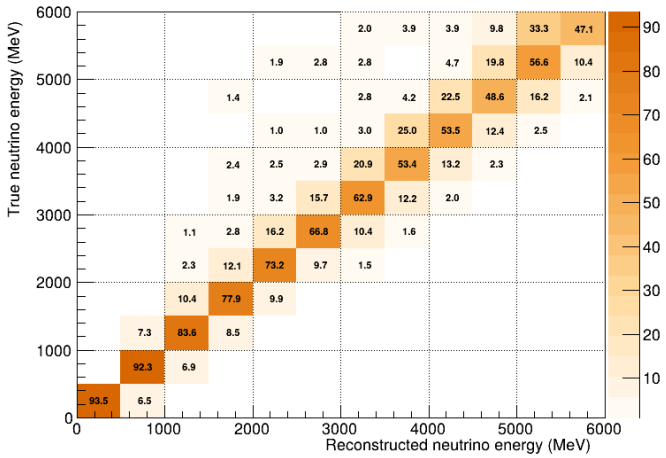

Fig. 5.17: *Normalized migration matrix for true generated CCQE on H selected events.*

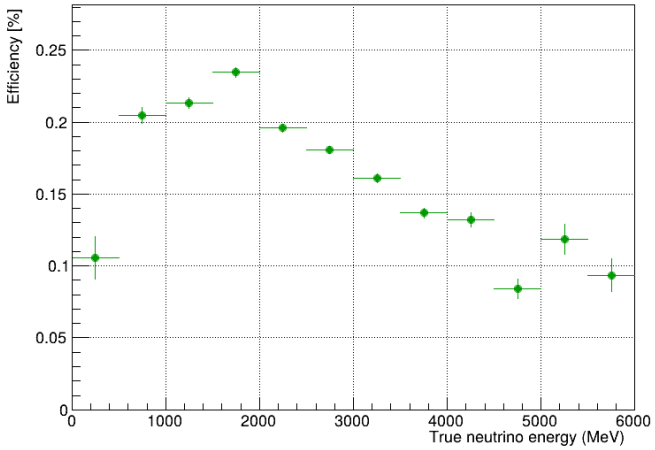

Fig. 5.18: *Efficiency as a function of the reconstructed neutrino energy.*

5.8 Results and outlooks

The final unfolded rate and the true one are shown in Fig. 5.19. The systematic uncertainties due to the event selection and the statistical subtraction technique are obtained from the ratio between these two distributions and the uncertainties associated with the unfolded rate. These uncertainties are illustrated in Fig. 5.20. In the energy region of interest (i.e. 1000-5000 MeV) they strongly oscillate between 5% and 20%. These statistical fluctuations are due to the low number of graphite background-like events used in the statistical subtraction, in these bins.

This work can be further improved in different ways. First of all, the number of generated events can be increased to remove the statistical fluctuations mentioned earlier. Up to now, 5 months of data taking have been simulated but the nominal runtime for achieving SAND's physics goals is approximately five years [42].

Moreover, the selection cut can be redefined and better tuned to minimize the quantity

of removed signal events.

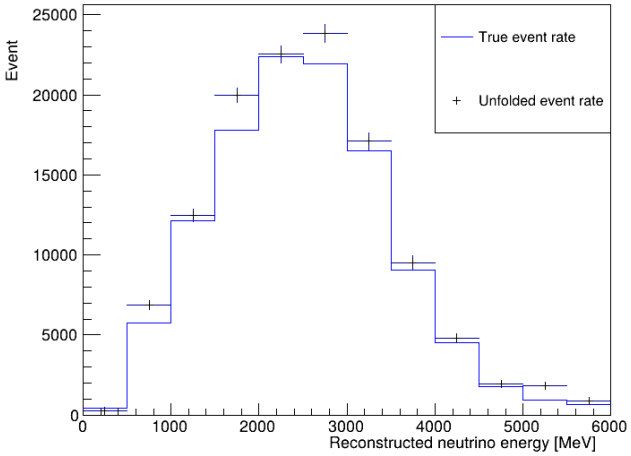

Fig. 5.19: *In blue the true energy distribution of neutrinos interacting on hydrogen, in black the unfolded rate corrected by the selection efficiency.*

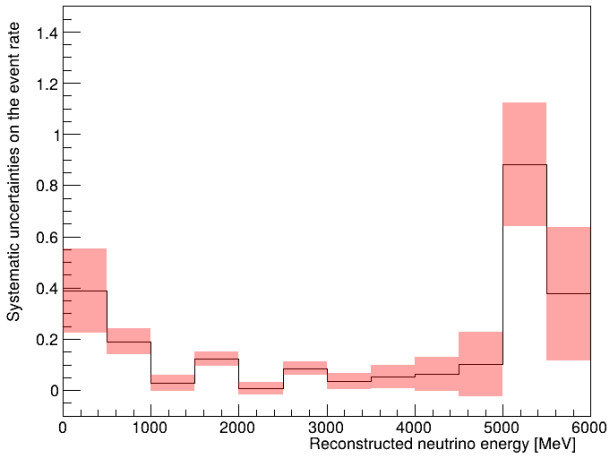

Fig. 5.20: *Systematic uncertainties on the event rate as function of the reconstructed neutrino energy. In black, the ratio between the unfolded rate and the true one. In red, the uncertainties given by the unfolded distribution.*

Conclusions

The SAND detector, a key component of the DUNE Near Detector Complex, is designed to precisely measure the neutrino flux, its composition, and its stability, thereby constraining the systematic uncertainties that limit oscillation measurements. SAND combines a 0.6 T superconducting magnet, an electromagnetic calorimeter, a 1-ton liquid-argon target (GRAIN), and a modular low-density tracker capable of percent-level momentum resolution.

A distinctive strength of SAND is its ability to obtain a large, effectively free-nucleon (hydrogen) interaction sample. This is achieved through the "solid hydrogen" technique: alternating polypropylene (C_3H_6) and graphite (C) targets, followed by a statistical subtraction of carbon-induced events. Because hydrogen interactions are free of nuclear effects, they allow clean kinematic selection and reduce the dominant uncertainties found in interactions on heavy nuclei.

To test this method, a full simulation was performed—including detailed detector geometry, neutrino interaction modeling, particle propagation, realistic detector response, and a Kalman-Filter–based reconstruction algorithm. The analysis focused on selecting the channel $\bar{\nu} + H \rightarrow \mu^+ + n$. The muon track is reconstructed in the tracker, while the neutron is identified in the calorimeter via time-of-flight. After applying cuts on fiducial volume, reconstruction quality, charge multiplicity, and neutron kinematics, the energy distribution of neutrino-hydrogen CC-QE interactions is estimated through statistical subtraction of the interactions on carbon.

The event rate is obtained through a Bayesian unfolding procedure and corrected for efficiency and resolution. Systematic uncertainties introduced by the solid-hydrogen technique are currently estimated at 5–20%, largely driven by limited statistics and expected to decrease with higher data exposure.

Appendix

In this table, all the variables organized and computed for the analysis are listed.

	Variable		Variable		Variable
1	EDepSimEvents_EventId	24	n_E	47	target
2	Enu	25	n_E_pred	48	tracks_ID
3	Evt_cat	26	n_P	49	true_n_startT
4	N_points	27	n_Ppred	50	true_n_startX
5	N_tracks	28	n_px	51	true_n_startY
6	Where_int	29	n_px_pred	52	true_n_startZ
7	cell_ID	30	n_py	53	true_n_stopT
8	cell_energies	31	n_py_pred	54	true_n_stopX
9	cell_y	32	n_pz	55	true_n_stopY
10	cell_z	33	n_pz_pred	56	true_n_stopZ
11	chi2	34	neutron_cluster	57	true_t
12	e_ecal	35	nu_Preco	58	true_x_pos
13	hit_pred	36	nu_type	59	true_y_pos
14	mu_E	37	primaries_PDG	60	true_z_pos
15	mu_Ereco	38	primaries_px	61	vertex_t
16	mu_P	39	primaries_py	62	vertex_x
17	mu_Preco	40	primaries_pz	63	vertex_y
18	mu_px	41	pxnu	64	vertex_z
19	mu_pxreco	42	pynu	65	x_ecal
20	mu_py	43	pznu	66	y_ecal
21	mu_pyreco	44	st_proc_type	67	z_ecal
22	mu_pz	45	t_ecal	68	nu_Ereco
23	mu_pzreco	46	t_pred		

Bibliography

[1] Wolfgang Pauli. "Letter to a physicists' gathering at Tübingen, December 4, 1930". In: *Collected Scientific Papers*. Ed. by R. Kronig and V. Weisskopf. Vol. 2. New York: Interscience, 1964, p. 1313.

[2] Enrico Fermi. "Tentativo di una Teoria dei Raggi *beta*". In: *Il Nuovo Cimento* 11.1 (1934), pp. 1–19. DOI: 10.1007/BF02959820.

[3] James Chadwick. "The Neutron and its Properties". In: *Nobel Lecture*. Dec. 1935. URL: https://www.nobelprize.org/uploads/2018/06/chadwick-lecture.pdf.

[4] F. Reines et al. "Detection of the Free Antineutrino". In: *Phys. Rev.* 117 (1 Jan. 1960), pp. 159–173. DOI: 10.1103/PhysRev.117.159. URL: https://link.aps.org/doi/10.1103/PhysRev.117.159.

[5] R. E. Carter et al. "Free Antineutrino Absorption Cross Section. II. Expected Cross Section from Measurements of Fission Fragment Electron Spectrum". In: *Phys. Rev.* 113 (1 Jan. 1959), pp. 280–286. DOI: 10.1103/PhysRev.113.280. URL: https://link.aps.org/doi/10.1103/PhysRev.113.280.

[6] G. Danby et al. "Observation of High-Energy Neutrino Reactions and the Existence of Two Kinds of Neutrinos". In: *Phys. Rev. Lett.* 9 (1 July 1962), pp. 36–44. DOI: 10.1103/PhysRevLett.9.36. URL: https://link.aps.org/doi/10.1103/PhysRevLett.9.36.

[7] K. et al. Kodama. "Observation of tau neutrino interactions". In: *Physics Letters B* 504.3 (Apr. 2001), pp. 218–224. ISSN: 0370-2693. DOI: 10.1016/s0370-2693(01)00307-0. URL: http://dx.doi.org/10.1016/S0370-2693(01)00307-0.

[8] ALEPH, DELPHI, L3, and OPAL Collaborations. "Determination of the Number of Light Neutrino Species". In: *Physics Letters B* 231.4 (1989), pp. 519–529. URL: https://cds.cern.ch/record/201511/files/198911031.pdf.

[9] Particle Data Group. *Review of Particle Physics*. Online at https://pdg.lbl.gov/index.html. Phys. Rev. D 110, 030001 (2024); accessed July 2025. 2024.

[10] Mark Thomson. *Modern Particle Physics*. Cambridge University Press, 2013.

[11] S. Braibant, G. Giacomelli, and M. Spurio. *Particles and Fundamental Interactions*. Springer, 2011.

[12] C. S. Wu et al. "Experimental Test of Parity Conservation in Beta Decay". In: *Phys. Rev.* 105 (4 Feb. 1957), pp. 1413–1415. DOI: 10.1103/PhysRev.105.1413. URL: https://link.aps.org/doi/10.1103/PhysRev.105.1413.

[13] M. Goldhaber, L. Grodzins, and A. W. Sunyar. "Helicity of Neutrinos". In: *Phys. Rev.* 109 (3 Feb. 1958), pp. 1015–1017. DOI: 10.1103/PhysRev.109.1015. URL: https://link.aps.org/doi/10.1103/PhysRev.109.1015.

[14] Sheldon L. Glashow. "The renormalizability of vector meson interactions". In: *Nuclear Physics* 10 (1959), pp. 107–117. ISSN: 0029-5582. DOI: https://doi.org/10.1016/0029-5582(59)90196-8. URL: https://www.sciencedirect.com/science/article/pii/0029558259901968.

[15] Steven Weinberg. "A Model of Leptons". In: *Phys. Rev. Lett.* 19 (21 Nov. 1967), pp. 1264–1266. DOI: 10.1103/PhysRevLett.19.1264. URL: https://link.aps.org/doi/10.1103/PhysRevLett.19.1264.

[16] A. Salam and J.C. Ward. "Electromagnetic and weak interactions". In: *Physics Letters* 13.2 (1964), pp. 168–171. ISSN: 0031-9163. DOI: https://doi.org/10.1016/0031-9163(64)90711-5. URL: https://www.sciencedirect.com/science/article/pii/0031916364907115.

[17] C. Giunti and C. W. Kim. *Fundamentals of Neutrino Physics and Astrophysics*. Oxford University Press, 2007.

[18] J. A. Formaggio and G. P. Zeller. "From eV to EeV: Neutrino Cross Sections Across Energy Scales". In: *Reviews of Modern Physics* 84.3 (Sept. 2012), pp. 1307–1341. ISSN: 1539-0756. DOI: 10.1103/RevModPhys.84.1307. URL: http://dx.doi.org/10.1103/RevModPhys.84.1307.

[19] Daniel Ivan Scully. "Neutrino Induced Coherent Pion Production". PhD thesis. University of Warwick, 2013.

[20] F. Battisti. "Development of a Novel Kalman Filter and Its Application to Neutrino Interaction Measurements in Next-Generation Time Projection Chambers". Ph.D. thesis. University of Oxford, 2024.

[21] J. L. Hewett et al. *Fundamental Physics at the Intensity Frontier*. 2012. arXiv: 1205.2671 [hep-ex]. URL: https://arxiv.org/abs/1205.2671.

[22] A. Bodek and J. L. Ritchie. "Further studies of Fermi-motion effects in lepton scattering from nuclear targets". In: *Phys. Rev. D* 24 (5 Sept. 1981), pp. 1400–1402. DOI: 10.1103/PhysRevD.24.1400. URL: https://link.aps.org/doi/10.1103/PhysRevD.24.1400.

[23] Julien Lesgourgues and Verde. *Neutrinos in Cosmology*. Online PDF, Particle Data Group Review, August 2023. Phys. Rev. D 110, 030001 (2024); accessed 22 July 2025. 2023. URL: https://pdg.lbl.gov/2024/reviews/rpp2024-rev-neutrinos-in-cosmology.pdf.

[24] B. Pontecorvo. "Inverse beta processes and nonconservation of lepton charge". In: *Zh. Eksp. Teor. Fiz.* 34 (1957), p. 247.

[25] Ziro Maki, Masami Nakagawa, and Shoichi Sakata. "Remarks on the Unified Model of Elementary Particles". In: *Progress of Theoretical Physics* 28.5 (Nov. 1962), pp. 870–880. DOI: 10.1143/PTP.28.870. URL: https://doi.org/10.1143/PTP.28.870.

[26] K. Lande and P. Wildenhain. "The Homestake chlorine solar neutrino experiment: Past, present and future". In: *Nucl. Phys. B Proc. Suppl.* 118 (2003). Ed. by F. von Feilitzsch and N. Schmitz, pp. 49–54. DOI: 10.1016/S0920-5632(03)01303-3.

[27] M. et al. Altmann. "Complete results for five years of GNO solar neutrino observations". In: *Physics Letters B* 616.3–4 (June 2005), pp. 174–190. ISSN: 0370-2693. DOI: 10.1016/j.physletb.2005.04.068. URL: http://dx.doi.org/10.1016/j.physletb.2005.04.068.

[28] J. N. at al. Abdurashitov. "Solar neutrino flux measurements by the Soviet-American gallium experiment (SAGE) for half the 22-year solar cycle". In: *Journal of Experimental and Theoretical Physics* 95.2 (Aug. 2002), pp. 181–193. ISSN: 1090-6509. DOI: 10.1134/1.1506424. URL: http://dx.doi.org/10.1134/1.1506424.

[29] John N. Bahcall and Raymond Jr. Davis. "Solar Neutrinos: A Scientific Puzzle". In: *Science* 191.4224 (Jan. 1976). Seminal paper on solar neutrino problem and early SSM predictions., pp. 264–267. DOI: 10.1126/science.191.4224.264. URL: https://doi.org/10.1126/science.191.4224.264.

[30] Y. Fukuda and T. et al. Hayakawa. "Evidence for Oscillation of Atmospheric Neutrinos". In: *Phys. Rev. Lett.* 81 (8 Aug. 1998), pp. 1562–1567. DOI: 10.1103/PhysRevLett.81.1562. URL: https://link.aps.org/doi/10.1103/PhysRevLett.81.1562.

[31] K. et al. Eguchi. "First Results from KamLAND: Evidence for Reactor Antineutrino Disappearance". In: *Physical Review Letters* 90.2 (Jan. 2003). ISSN: 1079-7114. DOI: 10.1103/physrevlett.90.021802. URL: http://dx.doi.org/10.1103/PhysRevLett.90.021802.

[32] M. H. at al. Ahn. "Indications of Neutrino Oscillation in a 250 km Long-Baseline Experiment". In: *Physical Review Letters* 90.4 (Jan. 2003). ISSN: 1079-7114. DOI: 10.1103/physrevlett.90.041801. URL: http://dx.doi.org/10.1103/PhysRevLett.90.041801.

[33] D. G. et al. Michael. "Observation of Muon Neutrino Disappearance with the MINOS Detectors in the NuMI Neutrino Beam". In: *Physical Review Letters* 97.19 (Nov. 2006). ISSN: 1079-7114. DOI: 10.1103/physrevlett.97.191801. URL: http://dx.doi.org/10.1103/PhysRevLett.97.191801.

[34] L. Wolfenstein. "Neutrino oscillations in matter". In: *Phys. Rev. D* 17 (9 May 1978), pp. 2369–2374. DOI: 10.1103/PhysRevD.17.2369. URL: https://link.aps.org/doi/10.1103/PhysRevD.17.2369.

[35] G. Barenboim. "Neutrinos Matter". In: *Proceedings of the 4th Latin American School of High-Energy Physics*. Ed. by CLAF and CERN. Paper no. 159, presented at the school; 17 pp. València, Spain, 2008. URL: https://cds.cern.ch/record/1114392/files/p159.pdf.

[36] Michael B. Smy. "The solar neutrino day/night effect in Super-Kamiokande". In: *Nuclear Physics B - Proceedings Supplements* 138 (Jan. 2005), pp. 91–93. ISSN: 0920-5632. DOI: 10.1016/j.nuclphysbps.2004.11.022. URL: http://dx.doi.org/10.1016/j.nuclphysbps.2004.11.022.

[37] Luca Stanco. "The next challenge for neutrinos: the mass ordering". In: *EPJ Web of Conferences* 164 (Oct. 2016). DOI: 10.1051/epjconf/201716401031.

[38] M. Aker et al. *Direct neutrino-mass measurement based on 259 days of KATRIN data*. 2024. arXiv: 2406.13516 [nucl-ex]. URL: https://arxiv.org/abs/2406.13516.

[39] M. C. Gonzalez-Garcia and M. Yokoyama. *Neutrino Masses, Mixing, and Oscillations*. https://pdg.lbl.gov/2023/reviews/rpp2023-rev-neutrino-mixing.pdf. Revised September 2023, in *Review of Particle Physics*. 2023.

[40] Helen Shao et al. *Cosmological limits on the neutrino mass sum for beyond-ΛCDM models*. 2024. arXiv: 2409.02295 [astro-ph.CO]. URL: https://arxiv.org/abs/2409.02295.

[41] NuFIT Collaboration. *NuFIT v5.3: Three-flavor oscillation parameters from our fit to global data as of March 2024*. NuFIT Collaboration. URL: https://www.nu-fit.org/?q=node/278.

[42] DUNE Collaboration. *Deep Underground Neutrino Experiment (DUNE), Far Detector Technical Design Report, Volume I: Introduction to DUNE*. 2020. arXiv: 2002.02967 [physics.ins-det]. URL: https://arxiv.org/abs/2002.02967.

[43] Deep Underground Neutrino Experiment (DUNE). *Deep Underground Neutrino Experiment*. https://www.dunescience.org/. July 2025.

[44] James Strait et Al. *Long-Baseline Neutrino Facility (LBNF) and Deep Underground Neutrino Experiment (DUNE) Conceptual Design Report Volume 3: Long-Baseline Neutrino Facility for DUNE June 24, 2015*. 2016. arXiv: 1601.05823 [physics.ins-det]. URL: https://arxiv.org/abs/1601.05823.

[45] B. Abi et al. *Deep Underground Neutrino Experiment (DUNE), Far Detector Technical Design Report, Volume IV: Far Detector Single-phase Technology*. 2020. arXiv: 2002.03010 [physics.ins-det]. URL: https://arxiv.org/abs/2002.03010.

[46] DUNE Collaboration et al. *The DUNE Far Detector Vertical Drift Technology, Technical Design Report*. 2023. arXiv: 2312.03130 [hep-ex]. URL: https://arxiv.org/abs/2312.03130.

[47] C. Brizzolari et al. "Enhancement of the X-Arapuca photon detection device for the DUNE experiment". In: *Journal of Instrumentation* 16.09 (Sept. 2021), P09027. ISSN: 1748-0221. DOI: 10.1088/1748-0221/16/09/p09027. URL: http://dx.doi.org/10.1088/1748-0221/16/09/P09027.

[48] A. Abed Abud et al. *Deep Underground Neutrino Experiment (DUNE) Near Detector Conceptual Design Report*. 2021. arXiv: 2103.13910 [physics.ins-det]. URL: https://arxiv.org/abs/2103.13910.

[49] Federico Battisti. "The DUNE Near Detector". In: Dec. 2022, p. 615. DOI: 10.22323/1.414.0615.

[50] Tom LeCompte. *Temporary Muon Spectrometer (TMS): LBNF*. Presentation (PDF) at TMS Meeting, Fermilab Indico, February 16, 2021. 2021. URL: https://indico.fnal.gov/event/47782/contributions/208331/attachments/139839/175631/LeCompte-TMS-LBNF-16Feb2021.pdf (visited on 08/2025).

[51] Andrea Bersani et al. *SPY: A Magnet System for a High-pressure Gaseous TPC Neutrino Detector*. 2024. arXiv: 2311.16063 [hep-ex]. URL: https://arxiv.org/abs/2311.16063.

[52] DUNE Collaboration et al. *Snowmass Neutrino Frontier: DUNE Physics Summary*. 2022. arXiv: 2203.06100 [hep-ex]. URL: https://arxiv.org/abs/2203.06100.

[53] K. et al. Abe. "Search for proton decay, data of Super-Kamiokande". In: *Physical Review D* 90.7 (Oct. 2014). ISSN: 1550-2368. DOI: 10.1103/physrevd.90.072005. URL: http://dx.doi.org/10.1103/PhysRevD.90.072005.

[54] Bernardini at al. *A Proposal to enhance the DUNE Near-Detector Complex v6.6*. Tech. rep. v6.6. https://indico.cern.ch/event/806612/attachments/1813045/2962023/A_Near_Detector_for_DUNE.pdf. Mar. 2019.

[55] Giulio Saracino. "The KLOE experiment at DANE". In: *Nuclear Physics A* 663-664 (2000), pp. 1103c–1106c. ISSN: 0375-9474. DOI: https://doi.org/10.1016/S0375-

9474(99)00787-3. URL: https://www.sciencedirect.com/science/article/pii/S0375947499007873.

[56] D.E. Andrews et al. "Progress in the design, manufacture and testing of the KLOE solenoid for the DANE ring at Frascati". In: 3 (June 1997), 3413–3415 vol.3. DOI: 10.1109/PAC.1997.753226.

[57] Nicolò Tosi. "The SAND detector of the DUNE experiment". In: *Nuclear Instruments and Methods in Physics Research Section A: Accelerators, Spectrometers, Detectors and Associated Equipment* 1080 (2025), p. 170727. ISSN: 0168-9002. DOI: https://doi.org/10.1016/j.nima.2025.170727. URL: https://www.sciencedirect.com/science/article/pii/S0168900225005285.

[58] M Adinolfi et al. "The KLOE electromagnetic calorimeter". In: *Nuclear Instruments and Methods in Physics Research Section A: Accelerators, Spectrometers, Detectors and Associated Equipment* 482.1 (2002), pp. 364–386. ISSN: 0168-9002. DOI: https://doi.org/10.1016/S0168-9002(01)01502-9. URL: https://www.sciencedirect.com/science/article/pii/S0168900201015029.

[59] Gianfranco Ingratta. "Study of Neutrino interactions on Hydrogen in the SAND detector of DUNE". PhD thesis. alma, Mar. 2025. URL: https://amsdottorato.unibo.it/id/eprint/11966/.

[60] V. Pia and on behalf of the DUNE collaboration. "Reconstruction of neutrino interactions in SAND with an innovative liquid Argon imaging detector". In: *Journal of Instrumentation* 19.02 (Feb. 2024), p. C02073. DOI: 10.1088/1748-0221/19/02/C02073. URL: https://dx.doi.org/10.1088/1748-0221/19/02/C02073.

[61] Valentina Cicero. "Study of the tracking performance of a liquid Argon detector based on a novel optical imaging concept". PhD thesis. alma, Giugno 2023. URL: https://amsdottorato.unibo.it/id/eprint/10871/.

[62] D.S. Armstrong and R.D. McKeown. "Parity-Violating Electron Scattering and the Electric and Magnetic Strange Form Factors of the Nucleon". In: *Annual Review of Nuclear and Particle Science* 62.1 (Nov. 2012), pp. 337–359. ISSN: 1545-4134. DOI: 10.1146/annurev-nucl-102010-130419. URL: http://dx.doi.org/10.1146/annurev-nucl-102010-130419.

[63] C. Andreopoulos et al. "The GENIE Neutrino Monte Carlo Generator". In: *Nucl. Instrum. Meth. A* 614 (2010), pp. 87–104. DOI: 10.1016/j.nima.2009.12.009. arXiv: 0905.2517 [hep-ph].

[64] Clark McGrew. *edep-sim: Energy Deposition Simulation*. URL: https://github.com/ClarkMcGrew/edep-sim.

[65] S. Agostinelli et al. "GEANT4—a simulation toolkit". In: *Nuclear Instruments and Methods in Physics Research Section A* 506.3 (2003), pp. 250–303.

[66] DUNE Collaboration. *sandreco: Simulation and Reconstruction Tools for SAND*. URL: https://github.com/DUNE/sandreco.

[67] Francesco Barilari. "Neutrino beam monitoring with the SAND detector at the DUNE near site". PhD thesis. URL: https://amslaurea.unibo.it/id/eprint/35319/.

[68] W. Pokorski R. Chytracek J. McCormick and R. Sehgal. "GDML: A Geometry Description Markup Language". In: *Proceedings of Computing in High Energy and Nu-*

clear Physics (CHEP 2006). 2006. URL: https://indico.cern.ch/event/408139/contributions/979922/attachments/815913/1118019/GDML_CHEP06.pdf.

[69] Brett Viren. *GeGeDe: General Geometry Description*. URL: https://github.com/brettviren/gegede.

[70] Yang G. *DunEndGGD*. URL: https://github.com/gyang9/dunendggd.

[71] Denise Casazza and Riccardo D'Amico (for the SAND software group). *SAND ECAL clustering and PID*. Tech. rep. DUNE Italia Collaboration Meeting, Ferrara. URL: https://agenda.infn.it/event/42478/contributions/247234/attachments/127552/188723/29Ott2024-DUNEItalia_Ferrara_Casazza.pdf.

[72] P. Abreu et al. "Performance of the DELPHI detector". In: *Nuclear Instruments and Methods in Physics Research Section A: Accelerators, Spectrometers, Detectors and Associated Equipment* 378.1 (1996), pp. 57–100. ISSN: 0168-9002. DOI: https://doi.org/10.1016/0168-9002(96)00463-9. URL: https://www.sciencedirect.com/science/article/pii/0168900296004639.

[73] Giulia Lupi. "Particle tracking in the DUNE-SAND detector: an extended Kalman filter approach". PhD thesis. URL: https://amslaurea.unibo.it/id/eprint/32197/.

[74] S. J. et al. Barish. "Study of neutrino interactions in hydrogen and deuterium: Description of the experiment and study of the reaction $\nu + d \to \mu^- + p + p_s$". In: *Phys. Rev. D* 16 (11 Dec. 1977), pp. 3103–3121. DOI: 10.1103/PhysRevD.16.3103. URL: https://link.aps.org/doi/10.1103/PhysRevD.16.3103.

[75] G. et al. Fanourakis. "Study of low-energy antineutrino interactions on protons". In: *Phys. Rev. D* 21 (3 Feb. 1980), pp. 562–568. DOI: 10.1103/PhysRevD.21.562. URL: https://link.aps.org/doi/10.1103/PhysRevD.21.562.

[76] M. et al. Derrick. "Multiplicity distributions in $\overline{\nu}_\mu p$ interactions". In: *Phys. Rev. D* 25 (3 Feb. 1982), pp. 624–633. DOI: 10.1103/PhysRevD.25.624. URL: https://link.aps.org/doi/10.1103/PhysRevD.25.624.

[77] H. Duyang et al. "A novel approach to neutrino–hydrogen measurements". In: *The European Physical Journal Plus* 139.11 (Nov. 2024). ISSN: 2190-5444. DOI: 10.1140/epjp/s13360-024-05783-y. URL: http://dx.doi.org/10.1140/epjp/s13360-024-05783-y.

[78] Tim Adye et al. *RooUnfold – ROOT Unfolding Framework*. https://gitlab.cern.ch/RooUnfold/RooUnfold.